

AD-A118 185 FOREIGN TECHNOLOGY DIV WRIGHT-PATTERSON AFB OH
JOURNAL OF AERONAUTICS. (U)

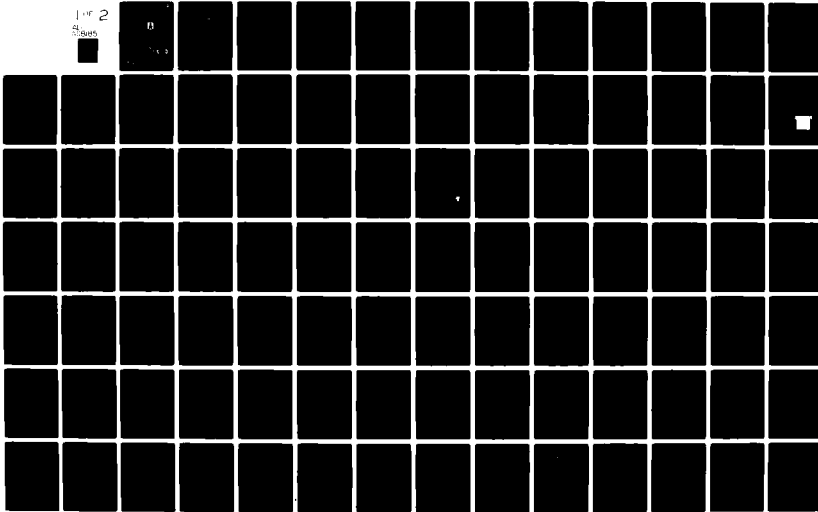
F/6 20/4

JUL 82
UNCLASSIFIED FTD-ID(RS)T-0621-82

NL

1 of 2
8 pages

B



@

AD A118185

FTD-ID(RS)T-0621-82

FOREIGN TECHNOLOGY DIVISION



JOURNAL OF AERONAUTICS



DTIC
ELECTED
AUG 16 1982
S D

D

Approved for public release;
distribution unlimited.

DTIC FILE COPY



82 08 16 015

Accession For	
NTIS GRA&I	<input checked="" type="checkbox"/>
DTIC TAB	<input type="checkbox"/>
Unannounced	<input type="checkbox"/>
Justification	
By _____	
Distribution/ _____	
Availability Codes	
Dist	Avail and/or Special
A	



FTD -ID(RS)T-0621-82

EDITED TRANSLATION

FTD-ID(RS)T-0621-82

21 July 1982

MICROFICHE NR: FTD-82-C-000989

JOURNAL OF AERONAUTICS

English pages: 163

Source: Acta Aeronautica et Astronautica Sinica,
Vol. 3, Nr. 1, March 1982, pp. 1-98

Country of origin: China

Translated by: LEO KANNER ASSOCIATES
F33657-81-D-0264

Requester: FTD/TQTA

Approved for public release; distribution unlimited.

THIS TRANSLATION IS A RENDITION OF THE ORIGINAL FOREIGN TEXT WITHOUT ANY ANALYTICAL OR EDITORIAL COMMENT. STATEMENTS OR THEORIES ADVOCATED OR IMPLIED ARE THOSE OF THE SOURCE AND DO NOT NECESSARILY REFLECT THE POSITION OR OPINION OF THE FOREIGN TECHNOLOGY DIVISION.

PREPARED BY:

TRANSLATION DIVISION
FOREIGN TECHNOLOGY DIVISION
WP.AFB, OHIO.

FTD -ID(RS)T-0621-82

Date 21 Jul 19 82

TABLE OF CONTENTS

Calculation of the Lift Distribution and Aerodynamic Derivatives of Quasi-Static Elastic Aircraft, by Liu Qianggang, Wu Changlin, Jian Zheng.....	1
Preliminary Study on Variable Porosity Walls for a Transsonic Wind Tunnel, by Variable Porosity Wall Research Group (Penned by Zhang Qiwei).....	20
A New Simultaneous Iteration Algorithm for Evaluation of Eigen-Problems in Large Structures, by Liu Guanggang and Li Junjie.....	33
Some Problems of Plate Bending Hybrid Model With Shear Effect, by Wu Changchun.....	46
A Local Strain Fatigue Analysis Method and Computer Program, by Wu Yisheng.....	61
Shock Wave Boundary Layer Interaction in Compressor Cascades, by Yu Shen.....	75
Experimental Study on Discharge and Loss Coefficients of Combustor Swirlers, by Zhang Chunxia and Wang Yulian.....	85
Asymptotic Stability of Partially Damped Mechanical Systems, by Gao Weibin.....	96
Aerodynamic Coefficient Identification of Time-Varying Aircraft System and Its Application, by Wang Tong.....	109
An Adjustment Method and Engineering Realization for Control Curves of the Two-Variable Function, by Shao Rongshi.....	124
BRIEF REPORTS ON RESEARCH	
Strain Fatigue Properties and Fatigue Dislocation Structures of 2024 Aluminum Alloy, by Li Qingsheng, Tsai Chikung, Chen Xianxi, Pan Tianxi.....	140
Study on Microstructure of Carbon-Aluminum Composites, by Zheng Lide, Zhang Guoding, Wang Wenrong, Shi Peiyuan.....	150
NEWS IN BRIEF- ACADEMIC ACTIVITIES	
Flourishing Developments in Academic Activities at China Aeronautic Institute.....	158

GRAPHICS DISCLAIMER

All figures, graphics, tables, equations, etc. merged
into this translation were extracted from the best
quality copy available.

CALCULATION OF THE LIFT DISTRIBUTION AND AERODYNAMIC DERIVATIVES OF QUASI-STATIC ELASTIC AIRCRAFT

Liu Qiangang, Wu Changlin, Jian Zheng
Northwestern Polytechnical University

Abstract:

A numerical method is presented for predicting the aerodynamic characteristics of elastic aircraft under quasi-static approximation. This method can be used to evaluate the lift distribution and 11 main longitudinal aerodynamic derivatives of elastic aircraft at subsonic speeds. The aerodynamic calculations are based on the Green's function method. The structure deformation is evaluated by the free structure influence coefficient method. The combination of these methods can provide an efficient, general and flexible aerodynamic tool for design of elastic aircraft.

Several numerical examples are given and some dynamical problems of elastic aircraft are also discussed in this paper. The derivatives evaluated in this paper can be directly adopted in analysis of stability and control of elastic aircraft.

I. FOREWORD

Numerical value calculation method is one important means of the present research on elastic aircraft pneumatic characteristics. Because this calculation involves problems in the areas of pneumatics, structure, and flight mechanics, the amount of work is comparatively large, and we must choose the appropriate method.

In the area of pneumatic force calculations, this text uses the speed force integral equation method that Greene's theorem gives guidance to. Its major merits are that it can be applied to pneumatic force computations of various complex aircraft contours, and excess machine time is comparatively less, and the results are relatively accurate. Thus it is comparatively appropriate for pneumatic force computations of elastic flight instruments. In the area of structural deformation computations, we used the free structure influence coefficient method. This method not only correctly explains the computation problems of aircraft structure deformations, but also because of the complete alikeness of the elastic aircraft pneumatic derivative that is gained

and other applicable dynamic equations on the form it analyzes and researches the dynamic state characteristics of elastic aircraft to bring many conveniences.

In this text we will carry out research and discussion on the strong question of when to use the influence coefficient method to calculate aircraft structure deformation, the problem of the coordinate axis system, and existing problems in some related documents of foreign research of elastic aircraft dynamic state characteristics.

II. TURBULENCE SPEED FORCE EQUATIONS AND OTHER NUMERIC VALUE EVALUATIONS

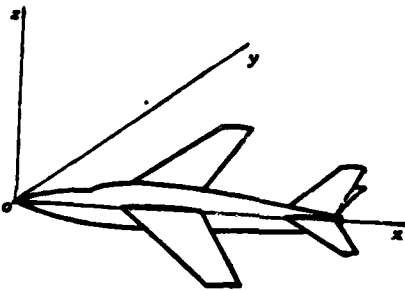


FIG. 1: COORDINATE SYSTEM

In pneumatic calculations, assume the coordinate system in Fig. 1 (in which ox axis and undisturbed airflow velocity directions are the same).

By the literature [1,2, and 3] when airflow flows through the aircraft, on the basis of Green's theorem, on the aircraft surface disturbance speed force Φ satisfies the following integral equation:

$$\begin{aligned} \Phi(X, Y, Z) = & -\frac{1}{2\pi} \iint_{S_b} \Phi^\infty \frac{1}{R} dS_b + \frac{1}{2\pi} \iint_{S_b} \Phi \frac{\partial}{\partial n} \left(\frac{1}{R} \right) dS_b \\ & + \frac{1}{2\pi} \iint_{S_w} \Delta \Phi \frac{\partial}{\partial n} \left(\frac{1}{R} \right) dS_w \end{aligned} \quad (1)$$

Where

$$X = x/\beta\delta, \quad Y = y/\delta, \quad Z = z/\delta, \quad \beta = \sqrt{1 - M_\infty^2}$$

$$R = \sqrt{(X - \xi)^2 + (Y - \eta)^2 + (Z - \zeta)^2}$$

Φ is the disturbance speed force Φ'' is the disturbance speed force method toward the derivative; c is the average pneumatic chord length; S_B expresses the aircraft surface; S_W is the turbulence area that is eased out by the wing or tail's rear edge; ξ , η , and ζ are the integral variable elements of the directions X, Y, and Z edges.

To design the aircraft surface equations we can use:

$$S(X, Y, Z) = 0 \quad (2)$$

to express, thus on S we have the following boundary conditions:

$$\Phi'' = -\frac{1}{|\nabla S|} \frac{\partial S}{\partial X} \frac{1}{c} \quad (3)$$

When using the numeric value solution to explain equation (1), with the aircraft surface divides into N small 4 side form elements, consider the speed force Φ value on every element as equal to constant, and also equal to the above-mentioned Φ value of the element's center. On every element, the value of Φ'' is also equal to constant, and also equal to the value of the above-mentioned center of the element Φ'' . The vortex area divides into some parallel vortex strips with the OX axis. Because the vortex surface cannot bear pressure, each vortex strip has:

$$\Delta\Phi = \Delta\Phi_{rs} = \text{constant} \quad (4)$$

Where $\Delta\Phi$ expresses the difference of the vortex strips top and bottom surface speed force; $\Delta\Phi_{rs}$ expresses the difference of wing surface rear edge top and bottom surface speed force. At the same time, on the basis of storage tower conditions, we can similarly consider that $\Delta\Phi_{rs}$ is equal to the difference of the element centroid top and bottom surface speed force that are linked together with the above-mentioned rear edge, to ensure that the rear edge pressure difference is zero.

Through the preceding treatment equation (1) can turn into an N exponential linear algebra equation that possesses N unknown mass Φ_i :

$$(a_i - b_i - w_i) \{\Phi_i\} = (b_i) \{\Phi''_i\} \quad (5)$$

Where δ_{ij} is an enumerable function. When $i=j$, $\delta_{ii}=1$. When $i \neq j$, $\delta_{ij}=0$.

$$b_{ij} = - \iint_{S_{Bj}} \frac{1}{2\pi R_i} dS_{Bj} \quad (6)$$

$$c_{ij} = \iint_{S_{Bj}} \frac{\partial}{\partial N} \left(\frac{1}{2\pi R_i} \right) dS_{Bj} \quad (7)$$

$$W_{ij} = \iint_{S_{Wj}} \frac{\partial}{\partial N} \left(\frac{1}{2\pi R_i} \right) dS_{Wj} \quad (8)$$

$$R_i = \sqrt{(X_i - \xi)^2 + (Y_i - \eta)^2 + (Z_i - \zeta)^2} \quad (9)$$

Where R is the distance of the required integral point (ξ, η, ζ) by the centroid of element i ; S_{Bj} expresses the surface of element j ; S_{Wj} expresses the vortex strip surface of the rear of element j .

After given matter surface geometric parameters, we can obtain the value of coefficients b_{ij} , c_{ij} , W_{ij} , and $\Phi_j^{(n)}$ by the literature [1]. By substituting them in equation (5) and evaluating this equation, we thus obtain the value Φ_j ($j=1, 2, \dots, N$) of each element's speed force. Later according to the following formula we can obtain the pressure coefficient of each element:

$$C_r = -\frac{2}{\rho} \left(\frac{\partial \Phi}{\partial X} \right), \quad (10)$$

Where $\left(\frac{\partial \Phi}{\partial X} \right)$ is obtained by use of the limited deviation method.

After obtaining the pressure coefficient, the lift and pitching movement coefficient are obtained by using the numeric value integral method. The deduction resistance coefficient uses the attainment of the "joint flow field" method. These coefficient derivatives can be obtained by using the method of calculating the increments of these coefficients and the ratio of corresponding conditional derivative increments.

As to the $\dot{\theta}$ derivative, it also can be obtained under the condition of determined common assumptions. To design the center of mass of the aircraft coil, we use the $\dot{\theta}$ angle velocity to make the pitching rotations, thus the attached angle of attack of the centroid of element j that has emerged is:

$$\Delta\alpha_i = (x_{i0} - x_{is}) \frac{\theta}{v_\infty} \quad (11)$$

This condition is equivalent to the aircraft not rotating and the dispersed variable curves of its geometric contour according to $\Delta\alpha_i$. To the corresponding curved aircraft, the boundary conditions change to:

$$\Phi_j^m = -(N_j \cos \Delta\alpha_i + T_j \sin \Delta\alpha_i) / \beta \quad (12)$$

Where N_{xj} and T_{xj} separately express the normal line of element j and the cosine of the tangent's same airflow direction and the included angle of the OX axis.

With formula (12) substituting equation (5), later according to the preceding same kind of measure to seek explanation we can obtain the pneumatic coefficient when the pitching angle velocity increments are θ , and with the mutual elimination of this pneumatic coefficient increment separation and the dimensionless angle velocity increments, we then can obtain the corresponding pneumatic derivatives.

III. SOME RELATED PROBLEMS OF COMPUTING FREE IN FLIGHT AIRCRAFT STRUCTURE ELASTIC DEFORMATION

1. Quasi-Static Assumptions and Other Conditions

When researching elastic aircraft dynamic state characteristics, in order to simplify computations we can adopt quasi-static assumptions. So called quasi-static assumptions refer to when researching elastic aircraft dynamic state characteristics, we omit a degree of free aircraft elastic movement, and consider each instantaneous elastic deformation of aircraft only related to the preceding instantaneous effect on the exterior of the aircraft. Also, consider that there is no mutual position difference between force and deformation. Except for wanting to consider the special characteristics of free flight, the relationship between them can be completely in accordance with the treatment of the relation between general static elastic mechanics center force and deformation.

Adopting quasi-static assumptions can greatly simplify computation. But only if the free oscillating frequency of the aircraft structure is comparatively higher than the rigid body motion frequency of the aircraft (for example the frequency of the aircraft vertical short cycle motion), then can they be applied. Because at this moment the coupling between the elastic motion of the aircraft structure and the rigid body motion of the aircraft is very weak. When the preceding two kinds of motion frequency are comparatively close, if we adopt quasi-static assumptions then we possibly will have fairly large error. At this time to research the dynamic state characteristics of aircraft we should compute the degree of free aircraft elastic motion.

2. The Average Axis System

When computing free flight aircraft structure elastic deformation, this text uses the average axis system, now introduced below. When the balanced state particle system of the free motion center receives the attached exterior effect, its disturbance motion can be broken down into three sections: a) Each section of the particle system with its center of mass together make attached translational motion. b) Each section of the particle system wind its center of mass to make rotating motion. c) the deformation motion of the particle system. The first two kinds of motion are jointly called rigid body motion. In these two kinds of motion, the relative position between each particle of the particle system doesn't change. The third kind of motion is elastic motion. In this kind of motion, the relative position of each particle changes. Designing δ_0 , δ_x , δ_z , to separately express the displacement of certain particles in the particle system in translational, rotational, and deformation motion. Thus the total displacement of certain particles in the particle system is equal to:

$$\delta_i = \delta_0 + \delta_x + \delta_z \quad (13)$$

Although the relative position of each particle within the particle system in deformation motion do change, this kind of change should not lead to the displacement of the position of the center of

mass of the particle system, and also should not lead to the whole particle system winding its center of mass to produce rotational motion. Because these two kinds of motion already break down among the former two kinds of rigid body motion. Because rigid body motion model state and elastic motion model state are mutually perpendicular, the elastic displacement of each particle in the particle system $\vec{\delta}_{ei}$ should satisfy the following two conditions:

$$\sum_{i=1}^N m_i \vec{\delta}_{ei} = 0 \quad (14)$$

$$\sum_{i=1}^N m_i \vec{r}_i \times \vec{\delta}_{ei} = 0 \quad (15)$$

Where m_i is the mass of the i particle; \vec{r}_i is the direct loss of the i particle to the center mass of the particle system; N is the total of the particles in the particle system.

Now we assume on the particle system selecting this kind of coordinate system oxyz with one right angle, when the particle system does not receive disturbance, its primary position is on the center mass of the particle system, and the direction of its three coordinate axis is determined by the conditions of (15). In the process of disturbance motion, it together with the particle system makes rigid body motion. This is also to say, its primary point throughout mutually coincides with the particle system's instantaneous center of mass. Moreover, it rotates together with the particle system. Clearly, this coordinate system is a non-inertia coordinate system. At the same time we say to this coordinate system, the rigid body displacement of each particle in the particle system of course can only be zero. Therefore the displacement of each particle in the particle system facing this coordinate system then is the elastic displacement $\vec{\delta}_{ei}$ that we require.

This kind of coordinate system is called the average body axis system. Its position can be determined according to conditions (14) and (15).

It is worthy to point out that when computing structure displace-

ment the structure influence coefficient that is used refers to its axis system as the structure axis system (its coordinate primary point and certain structure points of the aircraft are consolidated). It is different from the average body axis system.

IV. COMPUTATION OF FREE FLIGHT AIRCRAFT STRUCTURE ELASTIC DEFORMATION, FREE STRUCTURE INFLUENCE COEFFICIENT

The attached exterior of the aircraft rear disturbance of balanced state designed for free flight that emerges on element j is f_{zj} ; at this moment each element on the aircraft corresponding inertia force is equal to:

$$f_{Ik} = -m_k \left(\frac{f_{zj}}{m} + \frac{f_{zj} X_j X_k}{I_{yy}} \right) \quad (16)$$

$K = 1, 2, \dots N$

Where m is aircraft mass; I_{yy} is the pitching rotation inertia of the aircraft; X_j is the distance from the centroid of element j to the aircraft center mass edge OX direction; m_k is the mass of the K element.

Exterior force f_{zj} and the corresponding inertia force system f_{Ik} ($K=1, 2, \dots N$) constitute a balanced force system. Under the effect of these balanced force systems, displacement of the i element of the aircraft to the structure axis system is:

$$\delta Z_i = c_{ij} f_{zj} + \sum_{K=1}^N c_{ik} f_{ik} \quad (17)$$

Where c_{ij} is the structure influence coefficient of the corresponding structure axis system. With (16) substituting (17) it makes:

$$c_{ii} = c_{ij} - \frac{1}{m} \sum_{K=1}^N c_{ik} m_k - \frac{X_j}{I_{yy}} \sum_{K=1}^N c_{ik} m_k X_k \quad (18)$$

to obtain:

$$\delta Z_i = c_{ij} f_{zj} \quad (19)$$

Because in turbulent motion the structure axis system is not like the average body axis system that kind of completely with the aircraft together making rigid body transitional and rotational motion, the displacement of each element in the aircraft, except for elastic displacement, by structure axis system computations then cannot avoid including the composition of rigid body displacement, must deduct this kind of rigid body displacement, and then can obtain the elastic displacement of each element of the aircraft. Thus

$$\delta Z_{s_i} = \delta Z_i - \delta Z_r - \delta Z_{s_r}, \quad (20)$$

Where δZ_r is the displacement of the aircraft related structure axis system to make rigid body translational motion. Also it is simply the displacement of the primary point of the average body axis system toward the structure axis system; δZ_{s_r} is the displacement of the aircraft (also is simply the average body axis system) each element when making rigid body rotational motion toward the structure axis system.

Consider the condition of the deformation of the rear disturbance edges OX and OY axis can be omitted and not calculate the aircraft symmetry of the left and right sides. Formulas (14) and (15) can be simplified as:

$$\sum_{K=1}^N m_k \delta Z_{s_k} = 0 \quad (21)$$

$$\sum_{K=1}^N m_k X_k \delta Z_{s_k} = 0 \quad (22)$$

Where (20) substitutes (21) and (22) to obtain:

$$\delta Z_r = \frac{1}{M} \sum_{K=1}^N m_k \delta Z_k, \quad \delta Z_{s_r} = \frac{X_i}{I''} \sum_{K=1}^N m_k X_k \delta Z_k \quad (23)$$

With (23) substituting (20) to obtain:

$$\delta Z_{s_i} = \delta Z_i - \frac{1}{m} \sum_{K=1}^N m_k \delta Z_k - \frac{X_i}{I''} \sum_{K=1}^N m_k X_k \delta Z_k \quad (24)$$

$i = 1, 2, \dots N$

This is simply the correct computation formula for elastic displacement of each element of the aircraft rear disturbance. The preceding computation process clearly shows, by the displacement of the related structure axis system it deducts the corresponding rigid body displacement δZ_{x_0} , δZ_{x_1} . Also then corresponding to the displacement conversion of the related structure axis system is the displacement of the average body axis system. This is simply to say, when computing aircraft elastic displacement, we must use the average body axis system.

Where formula (19) substitutes formula (24), it makes:

$$c_{ij,ss} = c_{ij} - \frac{1}{m} \sum_{K=1}^N m_K c_{Kj} - \frac{X_i}{I_{ss}} \sum_{K=1}^N m_K X_K c_{Kj}$$

free

(25)

and we obtain:

$$\delta Z_{x_i} = c_{ij,ss} f_{x_i},$$
(26)

Where c_{ij} free represents the free structure influence coefficient, it expresses the effect of a unit of exterior force that the element j of the free flight aircraft receives, and the elastic displacement in element i is produced.

Consequently, the elastic displacement of each element in the aircraft becomes:

$$\{\delta Z_{x_i}\} = [c_{ij,ss}] \{f_{x_i}\}$$
(27)

V. COMPUTATIONS OF FREE FLIGHT ELASTIC AIRCRAFT BALANCED STATE LIFT DISTRIBUTION AND REAR DISTURBANCE PNEUMATIC DERIVATIVES

Elastic aircraft, when a specified altitude and specified number M make a level speed rectilinear flight, the following equation is established:

$$\left. \begin{array}{l} L_E - mg = 0 \\ M_E = 0 \\ \{\delta Z_{ij}\} = [c_{ij}] \{F_{Zj} - m_j g\} \end{array} \right\} \quad (28)$$

Where L_E is elastic aircraft lift; M_E is elastic aircraft pitching motion; F_{Zj} is the lift of the effect on elastic aircraft small elements.

By equation (28) we can determine the angle of attack α_1 , the rudder incline angle δ_1 , and the lift distribution of the aircraft this moment and lift coefficient C_{L1E} to deduce resistance coefficient C_{D11E} when specified number M and specified altitude make level speed rectilinear flight.

Equation (28) can be evaluated by use of the alternate method.

As to the calculation of elastic aircraft rear disturbance pneumatic derivatives, we can use the similar method of computing rigid aircraft pneumatic derivatives. What is different is that is the computation process we must according to formula (27) seek out the attached elastic displacement of each element of the aircraft rear disturbance, and later again seek the attached lift of the aircraft rear deformation and pitching motion to deduce the resistance coefficient.

When calculating the elastic displacement of each element of the aircraft rear disturbance we must also use the alternate method.

In accordance with the preceding method, when computing the quasi-static elastic aircraft pneumatic derivatives, because of applied free structure influence coefficients, we have already considered the use of exterior force of disturbance lift and other corresponding inertia force systems. Therefore in the pneumatic equation for aircraft disturbance, we need not again have other considerations due to the attached pneumatic force of inertia force toward the deformation influence that is rising. (Some literature says that this section derivative is inertial derivative. See the literature (7) and (10)).

Therefore the corresponding equation for quasi-static elastic aircraft motion of these pneumatic derivatives, and the second formula that is similar to the equation for rigid aircraft pneumatic derivative motion are computed. We only must use the quasi-static elastic aircraft pneumatic derivatives C_{LaE} and C_{maE} with each rigid body aircraft pneumatic derivatives C_{La} and C_{ma} then can be replaced.

VI. ANALYSIS OF COMPUTED EXAMPLES AND COMPUTED RESULTS

Using the preceding methods, we computed the pneumatic derivatives of lift distribution of balanced state and rear disturbance of certain large scale aircraft on a TQ-6 computer (The above-mentioned aircraft contours are shown in the simplified diagram in Fig. 2).

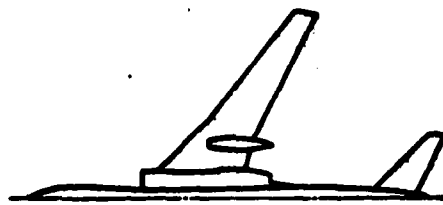


FIG. 2: AIRPLANE CONFIGURATION

Fig. 3 gives the rigid aircraft and elastic aircraft when $H=6000$ meters and $M_\infty = 0.6$ under alike lift coefficient ($C_{L1} = 0.26$) when making level speed rectilinear flight the wings open toward the load distribution and the chord toward the lift distribution. The balance state angle of attack and the rudder incline angle, elastic aircraft is $\alpha_{1E} = 3.5^\circ$, and $\delta_{1E} = 2.85^\circ$; rigid aircraft is $\alpha_1 = 2.76^\circ$, and $\delta_1 = 2.2^\circ$. By this we can see, under the same kind of conditions of Number M and altitude and flight weight, making level speed rectilinear flight, the angle of attack and rudder incline angle of elastic aircraft all are larger than those of rigid aircraft.

Fig. 4 gives the calculated results of rigid aircraft and elastic aircraft when the preceding altitude and Number M under the conditions of alike angle of attack ($\alpha = 3.5^\circ$). We can see by the figure, after computing the elastic deformation influence, the aircraft lift coeffic-

ient descends very much. In this calculation C_{L1E} descends more than C_{L1} by 13.9% ($C_{L1E}=0.26$, $C_{L1}=0.302$).

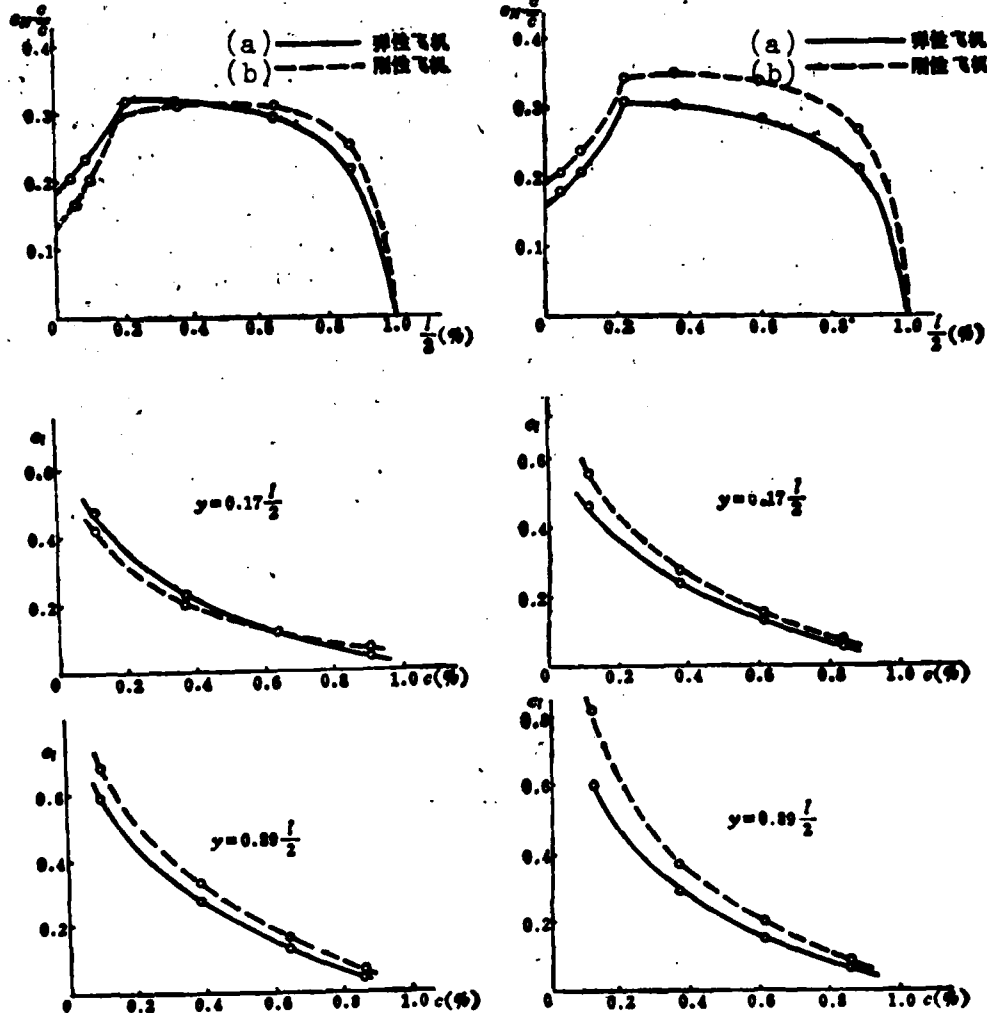


FIG. 3: COMPARISON OF LOAD DISTRIBUTION AND LIFT DISTRIBUTION ON RIGID AND ELASTIC AIRCRAFT AT $M_\infty = 0.6$, $C_y = 0.26$
KEY: (a) Elastic Aircraft
(b) Rigid Aircraft

FIG. 4: COMPARISON OF LOAD DISTRIBUTION AND LIFT DISTRIBUTION ON RIGID AND ELASTIC AIRCRAFT AT $M_\infty = 0.6$, $\alpha = 3.5^\circ$
KEY: (a) Elastic Aircraft
(b) Rigid Aircraft

Fig. 5 and Fig. 6 separate under the preceding conditions the elastic displacement of the wings and fuselage.

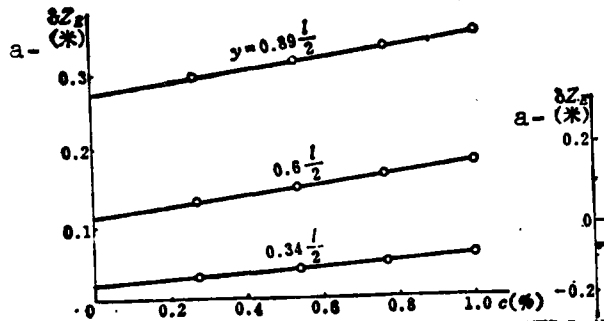


FIG. 5: ELASTIC DISPLACEMENT
OF WING. $M_\infty = 0.6$, $C_{yE} = 0.26$
KEY: (a) meter.

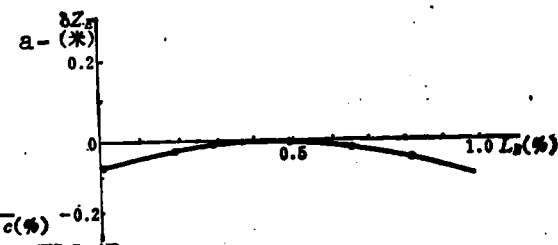


FIG. 6: ELASTIC DISPLACEMENT
OF FUSELAGE. $M_\infty = 0.6$, $C_{yE} = 0.26$
KEY: (a) meter.

Table 1 gives the computed value of the rear disturbance pneumatic derivatives of the preceding aircraft in the preceding flight conditions ($H=6000$ meters, $M_\infty = 0.6$, $C_{L1} = 0.26$). Computed value (1) is the computed result of rigid aircraft. Computed value (2) is the computed result of elastic aircraft. By the table we can see, after computing the structure elastic deformation influence, the above-mentioned aircraft's pneumatic derivatives have comparatively great change.

	Test Value	Computed Value		
		(1)	(2)	(3)
C_{L_a}	4.773	4.65	4.109	4.033
C_{m_a}	-0.8589	-0.880	-0.7278	-0.5471
$C_{D_{f_a}}$	0.1145	0.117	0.184	0.102
C_{L_b}		0.367	0.335	0.241
C_{m_b}	-0.8423	-1.05	-0.793	-0.728
C_{L_d}		1.849	0.7193	0.4475
C_{m_d}	-0.529	-0.118	-7.491	-7.106
$C_{D_{f_d}}$		0.084	0.0547	0.0312
C_{L_M}		0.128	-0.00274	-0.00058
C_{m_M}		-0.0323	-0.0163	-0.01066
$C_{D_{f_M}}$		0.00314	-0.00058	-0.00032

TABLE 1: $M=0.6$, $H=6000$ meters, $C_{L1}=0.26$, $\bar{q}=1212 \text{ kg/m}^2$

For easy comparison, Table 1 lists directly the elastic aircraft pneumatic derivatives that use the structure influence coefficient c_{ij} to calculate deformation. At this moment the aircraft consolidates the center of mass when there is no deformation. "Elastic" displacement is the structure axis system of the aircraft center of mass that is relative to the primary point position when there is no deformation. This kind of method of computing elastic aircraft pneumatic derivatives in the past had been some means that were adopted, but from the basic principle we came to see, clearly it is not correct. By Table 1 we can see that the elastic aircraft pneumatic derivatives that use this method of computation is much more serious than the derivative that uses c_{ij} free to calculate its elastic deformation. But this in reality is only a false appearance, because this method of treatment does not correctly reflect the realistic condition of free flight quasi-static elastic aircraft rear disturbance.

VII. SOME PROBLEMS OF QUASI-STATIC ELASTIC AIRCRAFT STABILITY AND CONTROL

With the quasi-static elastic aircraft pneumatic derivatives that the preceding section obtained, substitute the related formula of rigid aircraft stability and control. We then obtain the corresponding formula for quasi-static elastic aircraft. For example, as to quasi-static elastic aircraft specified speed focus, we have:

$$\bar{X}_{\alpha_s} - \bar{X}_{\alpha_{sp}} = \frac{C_{m_{sp}}}{C_{L_{sp}}} \quad (29)$$

As to specified load focus, we have:

$$\bar{X}_{\alpha_s} - \bar{X}_{\alpha_{sp}} = \frac{C_{m_{sp}}}{C_{L_{sp}}} \left(1 + \frac{C_{L_{sp}} M}{2 C_{L_1}} \right) - \frac{C_{m_{sp}} M}{2 C_{L_1}} \quad (30)$$

As to specified normal level rectilinear flight, the rudder incline angle with the variable frequency of the the velocity, we have:

$$\left(\frac{\Delta \delta}{\Delta \theta} \right)_s = -2 C_m \frac{\frac{C_{m_{sp}}}{C_{L_{sp}}} \left(1 + \frac{C_{L_{sp}} M}{2 C_{L_1}} \right) - \frac{C_{m_{sp}} M}{2 C_{L_1}}}{C_{m_{sp}} - C_{L_{sp}} \frac{C_{m_{sp}}}{C_{L_{sp}}}} \quad (31)$$

Where \bar{X}_{ss} , \bar{X}_{so} , and $\bar{X}_{sol_{n-1}}$ the X coordinates of the aircraft centroid, the specified speed focus, and the specified load focus, and their ratio to the average pneumatic chord. $(\Delta\delta/\Delta\bar{\theta})_s$ is the ratio of the increments of the rudder incline angle in level speed rectilinear flight and the increments of flight velocity, in which $\Delta\bar{\theta} = v/v_\infty$.

In Table 1, the value of the quasi-static elastic aircraft corresponding pneumatic derivatives substitute formulas (29), (30), and (31) to obtain:

$$\bar{X}_{ss} - \bar{X}_{so,s} = -0.177, \bar{X}_{ss} - \bar{X}_{sol_{n-1}} = -0.1416, (\Delta\delta/\Delta\bar{\theta})_s = 0.1$$

As to rigid aircraft, the preceding coefficient values are:

$$\bar{X}_{ss} - \bar{X}_{so} = -0.1892, \bar{X}_{ss} - \bar{X}_{sol_{n-1}} = -0.18, \Delta\delta/\Delta\bar{\theta} = 0.095.$$

Thus we can see, after computing the elastic deformation influence, the specified speed focus and the specified load focus both move forward, and the value of $\Delta\delta/\Delta\bar{\theta}$ yet has increases.

In order to understand the pneumatic characteristics of quasi-static aircraft high subsonic speed pressure time, we still computed the focal position of elastic aircraft and rigid aircraft when $M_\infty = 0.8$; its value is as Table 2 expresses:

	Rigid Aircraft	Elastic Aircraft	
\bar{q} (公斤/米 ²)	2468	2155	2468
$\bar{X}_{ss} - \bar{X}_{so}$	-0.233	-0.202	-0.199
$\bar{X}_{ss} - \bar{X}_{sol_{n-1}}$	-0.22	-0.1987	-0.186

TABLE 2

The preceding computations explain that when M increases from 0.6 to 0.8, and speed pressure \bar{q} increases from 121.2 kg/m^2 to 2155 kg/m^2 then elastic aircraft specified speed focus moves back in volume less than rigid aircraft does. This is because the influence of the speed force rising elastic deformation lowers the influence of a section of

Number M. By Table 2 we can yet see that when Number M is fixed, with the speed pressure increase, the specified speed focus and the specified load focus both move forward, and specified speed and specified load degree of stability both descend.

Because the factors that effect elastic aircraft pneumatic characteristics are comparatively complex, by certain opinions or conclusions of aircraft computed results that have been gained, no certainties can be extended to other aircraft. For example, in literature (6) the value of the specified load focus of a certain aircraft when $M_{\infty}=0.8$ is calculated. The above text considers that when $M_{\infty}=0.8$, with speed pressure increases, specified load focus position continually moves back, when speed pressure is very large, the specified load focus is far behind the aircraft centroid. Moreover, the variations are not sensitive to the centroid. But in this text, the conditions of the preceding computations are not like this. When $M_{\infty}=0.8$, with speed pressure increase, specified load focus on the contrary moves forward. Therefore we consider that if the literature (6)* computed results are believable, they only represent particular conditions of certain types of aircraft. Moreover, we cannot obtain from this a general conclusion.

Lastly we want to briefly discuss some problems that merit attention when using some other methods to treat quasi-static elastic aircraft dynamic state characteristics. In recent years, foreign documents have brought out some methods to use the so-called "zero quality pneumatic derivatives" and "inertia derivatives" to compute elastic aircraft pneumatic characteristics. The so-called "zero quality pneumatic derivative" is simply on the aircraft rear disturbance, and only computes the elastic aircraft pneumatic derivatives of the exterior force rising "structure deformation" gains. The so-called "inertia derivative" is simply on the aircraft rear disturbance, and only considers the effect of the derivative of the aircraft inertia force rising "structure deformation" gains. When taking the exterior force system and its corresponding inertial force system to separately

* Computed formulas in literature 6 of specified load focus are not correct. See the following discussion in this text or literature 4 .

compute the structure deformation that has arised, because they both are not balanced force systems, when computing deformation, the sustaining reaction force that is used is not equal to zero. Therefore, in "zero quality pneumatic derivatives" and "inertia derivatives" computations, the sustaining effect exists. When the sustaining conditions change, the numeric value of the derivative also changes. Therefore, by themselves "zero quality pneumatic derivatives" and "inertia derivatives" are not of realistic significance. But after substituting elastic aircraft pneumatic equations with these derivatives (This kind of quasi-static elastic aircraft pneumatic equations and rigid aircraft pneumatic equations are not the same), because all the exterior force systems of disturbance rising and their corresponding inertia force still constitute balanced force systems, the sustaining effect of these derivatives mutually reduce. Using this kind of equation and derivative to compute the dynamic state characteristics of quasi-static elastic aircraft, its conclusion is still correct. But the "zero quality pneumatic derivative" alone, due to the sustaining influence included among it, cannot be used to compute and analyze the control and stability characteristics of the aircraft. Therefore, any other derivative formula using "zero quality pneumatic derivatives" or uses when computing aircraft elastic deformation not balanced force system gains to research the fixed speed focus of elastic aircraft and the fixed load focus and its control and stability performance generally speaking is not correct. Literature (6)when computing the fixed load point of elastic aircraft, the pneumatic derivative that is used clearly brings on the sustaining influence, because what it uses when computing aircraft structure deformation is not balanced force system. Therefore the sustained reaction force is not equal to zero. At the same time, the coordinate system that the above text uses when computing the aircraft structure deformation is not a balanced axis system. This kind of computed results are not accurate.

In some other literature (for example 7 and 10) some similar problems also exist. Because literature 4 has already made detailed discussion of these problems, we won't repeat it here.

This text has already been checked and approved by Prof. Zhang Guilian, who also pointed out valuable opinions. We hereby express our thanks.

Reference Literature:

- (1) Xi Bei Gong Ye Da Xue Deng Dan Wei Tan Xing Ke Ti Ban Zuo Zu, Ya Yin Su Ji Yi, Ji Shen, Wei Yi Zu He Ti Ya Li Fen Bu Ji Qi Dong Xi Shu De Ji Suan, Qi Dong Yan Jiu Yu Fa Zhan, 1978 Nian Di 5 Qi, 91 Ye Zhi 102 Ye. "Northwestern Polytechnic University, Elastic Problem Action Group; Computations of Subsonic Speed Wings, Fuselage, and Tail Constituted Body Pressure Dispersement and Pneumatic Derivatives; Pneumatic Research and Development, No. 5, 1978, pages 91-102."
- (2) L. Morino and C. C. Kao. Subsonic Potential Aerodynamics for Complex Configurations. A General Theory. AIAA Journal Vol. 12, №. 2 Feb. 1974.
- (3) L. Morino, L. T. Chen, E. O. Sack. Steady and Oscillatory Subsonic and Supersonic Aerodynamics Around Complex Configurations. AIAA Journal Vol. 15 №. 3 Mar. 1978.
- (4) Zhang Guilian, Guan Yu Yong Ying Xiang Xi Shu Fa Chu Li Zhun Jing Tan Xing Fei Ji Dong Tai Te Xing Wen Ti De Yi Xie Yi Jian. Hang Kong Xue Bao, 1978 Nian De 2 Qi; "Zhang Guilian, Some Opinions Regarding Problems of Using the Influence Coefficient Method to Treat Quasi-Static Elastic Aircraft Dynamic State Characteristics; Journal of Aeronautics, No. 2, 1978."
- (5) A. S. Taylor and D. L. Woodcock. Mathematical Approaches to the Dynamics of Deformable Aircraft. R&M №. 3776; 1976.
- (6) William B. Kemp, Jr. Definition and Application of Longitudinal Stability Derivatives for Elastic Airplanes. NASA TN D-6629.
- (7) J. Roskam, A. Dusto. A method for Predicting Longitudinal Stability Derivatives of Rigid and Elastic Airplanes. Journal of Aircraft. Vol. 6 №. 6 1969.
- (8) NASA CR 73276, 11, 1968.
- (9) Howard L. Chevalier, Gerald M. Dornfeld, Robert C. Schwanz. An Analytical Method for Predicting the Stability and Control Characteristics of Large Elastic Airplane at Subsonic and Supersonic Speeds. AGARD Conference Proceedings №. 46.
- (10) J. Roskam, Comments, Interpretation and Application of A Method for Predicting Aerodynamic Characteristics of Large Flexible Airplanes. AGARD Conference Proceedings №. 46.

PRELIMINARY STUDY ON VARIABLE POROSITY WALLS FOR A TRANSONIC WIND TUNNEL

Variable Porosity Wall Research Group, Nanjing Aeronautical Institute
Penned by Zhang Qiwei

Abstract:

In order to reduce the wall interference and improve quality of the flow field in a transonic wind tunnel, a set of variable porosity walls with 60° inclined holes have been designed and manufactured. The open-area ratio of the walls can vary continually from zero to 9.2 percent. The walls have been used in a 600mm×600mm transonic and supersonic wind tunnel with solid side walls. This paper describes the general characteristics of the variable porosity walls and the preliminary results of calibration at Mach numbers ranging from 0.6 to 1.2.

SYMBOLS:

M	Airflow Mach number
M _t	Test section nucleus uniform internal area average Mach number
M _o	Computed airflow Mach number of static pressure from station reference point
M _w	Computed airflow Mach number of static pressure from test section side wall
ΔM _s	$\Delta M_s = M_s - M_o$
ΔM _r	$\Delta M_r = (M_r - M_o)$ with model $-(M_r - M_o)$ without model
Re	Unit length Reynold's number (1/m)
P	Static pressure
P _o	Front chamber total pressure
θ	Wall plate expansive angle (expansive is straight)
K	Open area ratio of porosity wall
d	Diameter of porosity wall
A	Dynamic plate shift distance of variable porosity wall plate
D	Diameter of 20° cone-cylinder model cylinder section
H	Wind tunnel test section altitude
L _a	Airflow acceleration section length
x	Distance from test section entrance cross section
x ₁	Distance from top point of 20° cone-cylinder model

- σ_m Mean root error of the test section nucleus flow uniform internal area Mach number
 c_y^a Derivative ($1/\alpha$) of the zero facing angle time lift coefficient to the facing angle
 \bar{x}_F Ratio of the distance of the zero facing angle time focus from the top point of the model and the largest diameter of the model fuselage
 Cx_0 Resistive coefficient of the zero facing angle time
 ΔCx_0 Resistive coefficient increments, $\Delta Cx_0 = Cx_0 - Cx_0(M=0.8)$

I. PREFACE

In order to fully weaken the interference of the tunnel walls of the transonic wind tunnel, outside the country many wind tunnels use variable porosity walls^(1,2). In order to improve the flow field characteristics of the transonic wind tunnel and understand some particular problems of using variable porosity walls, we have designed and manufactured on our own a set of continuable variable porosity walls. In 1980 this set of porosity walls was used in a tunnel with a high speed of 600mmx600mm to conduct preliminary flow field calibration: researched in the scope of $M=0.6\sim 1.2$ porosity and the influence of wall plate expanse angle to the flow field, and calibrated the interrelation between the station reference point Mach number and the nucleus flow uniform internal area average Mach number, using the 20° porosity cone-cylinder model to conduct calibration pressure tests. It was preliminarily determined to use from now on the scope of δ and K , and also conducted AGARD-B standard model calibration pressure tests. This text explains the general situation of this kind of variable porosity wall and preliminary calibration results.

II. SIMPLIFIED CONDITIONS OF A WIND TUNNEL

This wind tunnel is a direct flow down temporary formula wind tunnel. Its minute details are seen in material (3). The test section model cross section is a square of 600mmx600mm. The test section length is 1580mm. The test section Mach number range is 0.5~3.5. When $M=0.5\sim 1.2$ a solid speed of sound nozzle is used, depending on changing the front chamber total pressure to change the Mach number. The left and

right side walls of the test section are fixed parallel solid walls, which are porous from top to bottom, and the expanse angles can be adjusted. The station depth is comparatively small. The most shallow place is only 170mm. Moreover, there is no auxiliary air exhaust system. As our first step we only take the straight porosity walls that were formerly used and switch over to variable porosity walls to conduct tests. When $M=1.5\sim 3.5$ this wind tunnel uses replaceable two dimensional nozzles to change the Mach number, and the test section walls are all solid walls.

III. GENERAL CONDITIONS OF VARIABLE POROSITY WALLS

Variable porosity walls are composed of steel plates that have two layers open with holes. Detailed structure can be seen in material (4), and a simplified diagram is shown in Fig. 1. The layer of porosity plate near the airflow is fixed and doesn't move. The other layer of porosity plate can shift back and forth. When the holes of the two plates are completely aligned, the wall plate porosity gets the largest. According to the computations in Fig. 1, $K_{\text{largest}} = (\pi \times 4.5^2) / (65 \times 10) = 9.8\%$, but because the fixed position screw occupies a separate hole position, the realistic largest porosity is 9.2%.

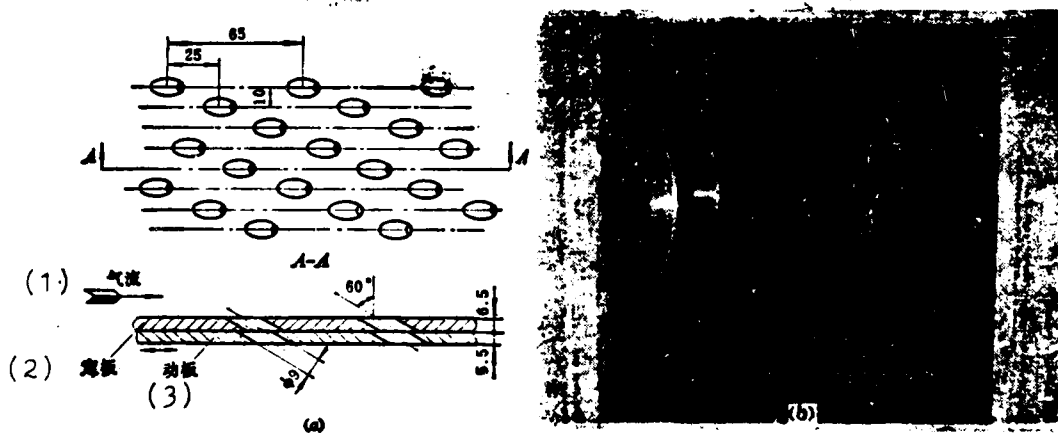


FIG. 1 DETAILS OF VARIABLE POROSITY WALLS
 (a) Simplified diagram of variable porosity wall
 (b) Variable porosity test section
 KEY: (1) Airflow; (2) Fixed plate; (3) mobile plate

When the holes of the two plates are completely spread apart, the porosity tends toward zero. The holes are evenly distributed, the back of the moving plate of the front wall can plug into the blocking plate of various models, to change the airflow acceleration characteristics. Experiments demonstrate that when not adding any block plate the airflow acceleration section is shortest (when $K=6\%$, La/H can shorten to 0.4), and at this moment in the uniform area the airflow fluctuation also is not great. Therefore, now we do not add a blocking plate.

The model support of this wind tunnel is located in the inside of the test section. When wall plate porosity varies very little, the transonic support plug up effect will be extremely severe. Therefore on the support area wall plate is added ten cracks that are 5mm wide and 200mm long (see the photograph in Fig. 1).

The moving plate of this wall plate is run by a model DG-6 electronic motor. When reducing porosity, the moving plate contrary air flow direction shifts. Its shift distance is measured by model LVDT displacement sensor. Measurement precision is $\pm 0.1\text{mm}$. The relationship between the moving plate shift distance A and porosity K is according to the following computations (when we make $K=K_{\text{largest}}, A=0$):

$$K = K_{\text{max}} \times \frac{2}{\pi} \left[\arccos\left(\frac{A}{2d}\right) - \left(\frac{A}{2d}\right) \sqrt{1 - \left(\frac{A}{2d}\right)^2} \right]$$

IV. CONTENTS OF EXPERIMENTS

Emperiment Mach number scope is 0.6~1.2, $Re=(1.3~2.3)\times 10^7/\text{m}$; Porosity variation scope is 0~7%; Wall plate expanse angle variation scope is 0~0.6°. Front chamber total pressure, station pressure, and test section sideplate static pressure is calibrated. We use fixed in the test section on the center line axial static pressure sounding tube to calibrate test section nucleus flow Mach number distribution. The axial static pressure sounding tube external diameter is 28mm; on the tube each interval of 40mm has a calibration pressure hole, and top to bottom staggered arrangement. We also calibrated the sur-

face distributed pressure of a 20° cone-cylinder model. The length of the cone-cylinder model is 720mm; the diameter of the cylinder section is 68mm; the plug proportion weight is 1%. The position of the axial sounding tube and the 20° cone-cylinder model in the test section is shown in Fig. 2. Aside from this, we still conducted AGARD-B standard tests to measure pressure under different porosity variation regulations.

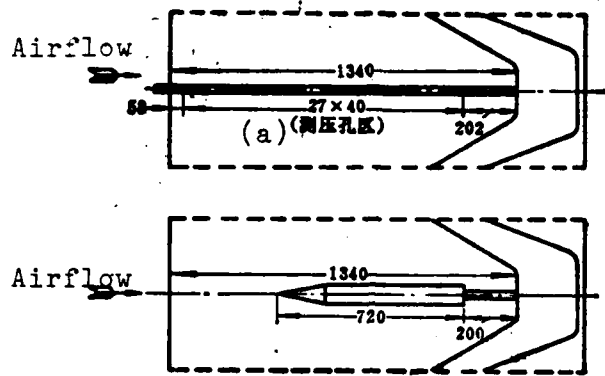


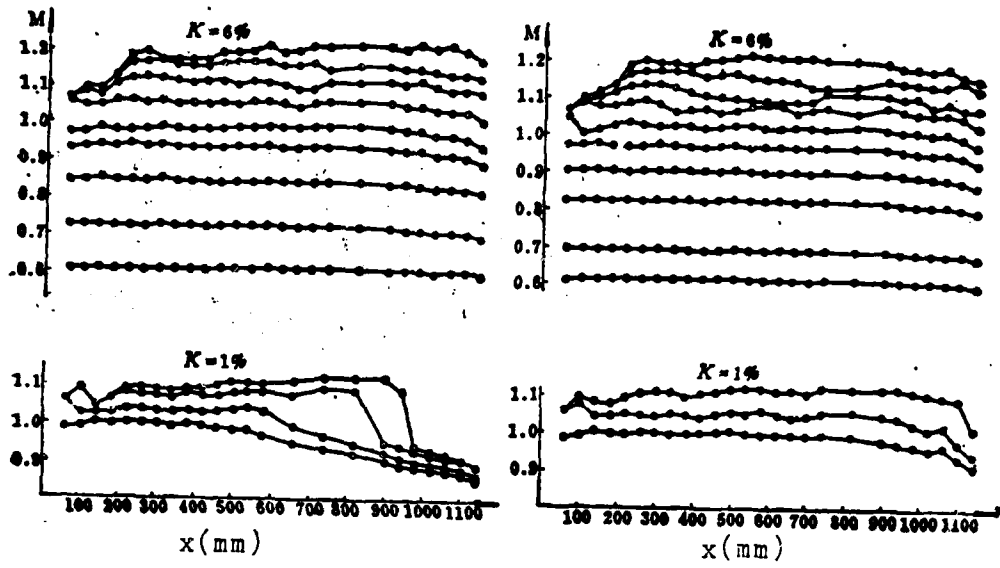
FIG. 2 LOCATION OF CENTERLINE STATIC PRESSURE AXIAL SOUNDING TUBE AND 20° CONE-CYLINDER MODEL IN THE TEST SECTION
KEY: (a) Calibration hole area

V. PRINCIPAL TEST RESULTS

1. The Flow Field of Nucleus Flow

Figures 3 and 4 separately give the Mach number distribution of the nucleus flow under typical conditions and the σ_M value of this wall plate under general conditions.

(1) The influence of δ to the nucleus flow field: when δ value increases, subsonic speed airflow uniform degree gets better, supersonic speed airflow acceleration gets faster. If δ enlarges, then excessive acceleration emerges on the supersonic speed area, and causes the flow field uniform degree to get worse. δ decreases then it causes the Mach number to be unable to reach 1.2. δ can be chosen and used in the range of 0.2°~0.5°.



(a) Supporting area without crack
 (b) Supporting area with crack $\delta = 0.5^\circ$

FIG. 3 TYPICAL CENTERLINE MACH NUMBER DISTRIBUTION

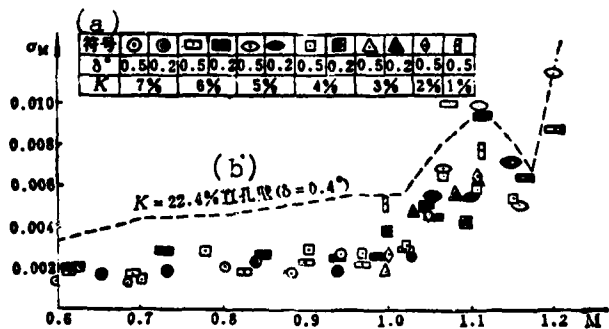


FIG. 4 CENTERLINE LOCAL MACH NUMBER

DEVIATION (RMS)

KEY: (a) Symbol; (b) Straight hole wall

(2) The influence of K to the nucleus flow field: When the value of K increases, subsonic speed airflow uniform degree gets better, and supersonic speed airflow acceleration gets faster. If K enlarges, then excessive acceleration emerges in the supersonic speed area, and causes airflow uniform degree to get worse. From the flow field uniform degree we come to see that when subsonic speed takes $K=6\sim 7\%$ it is better, at supersonic speed the K value is best to change with the Mach number, its numeric value is related to δ , when δ is larger

we should apply a smaller K value. For example, when $M_t=1.20$, we take $\delta=0.5^\circ$, and $K=6\%$ is better; when $M_t<1.15$, if $\delta=0.5^\circ$, then to take $K<4\sim5\%$ is better; if $\delta=0.2$, then to take $K<5\sim6\%$ is better.

(3) Influence of supporting region wall plate slot: The rigid support of this wind tunnel is located in the test section. Its plug ratio weight is 4.26%. By Fig. 3 we can see, if the supporting region wall plate has no slot, then when porosity is small the influence of the supporting plug effect to the upper area is very serious, causing the airflow uniform region to greatly shorten, and the above-mentioned phenomenon behind the supporting region slot greatly lightenes. We can see that the supporting region wall plate slot is neccessary. To sum up, the flow field uniform degree of this wall plate is better than the fixed straight hole wall that this wind tunnel formerly used (Fig. 4).

2. The Station Reference Point Mach Number M_c

Through calibration we discovered that the pressure distribution of the lower part of the station is relaticely uniform, therefore we each took a calibration pressure point of comparatively advanced position in the lower section up and down the station and according to the total made a reference point. The same time as calibrating the nucleus flow Mach number, we calibrated the reference point Mach number M_c . Figure 5 gives the deviation value of M_c and M_t under typical conditions.

When the supporting region wall plate has a slot, the effect of the variation toward ΔM_c is relatively small. In Fig. 5 (a) the scope of variation of M_c value approximately corresponds to $2^\circ M$, this and the ADP wall plate test results in literature (5) are similar. When the wall plate has no open slot, with the reductio of the K value, ΔM_c markedly reduces, this and the LAR wall plate test results of literature (5) are similar. We can see that the wall plate slot (slot ventilation area is not following K variation) can reduce the effect of K on ΔM_c .

In order to research the effect of the model existence on M , when

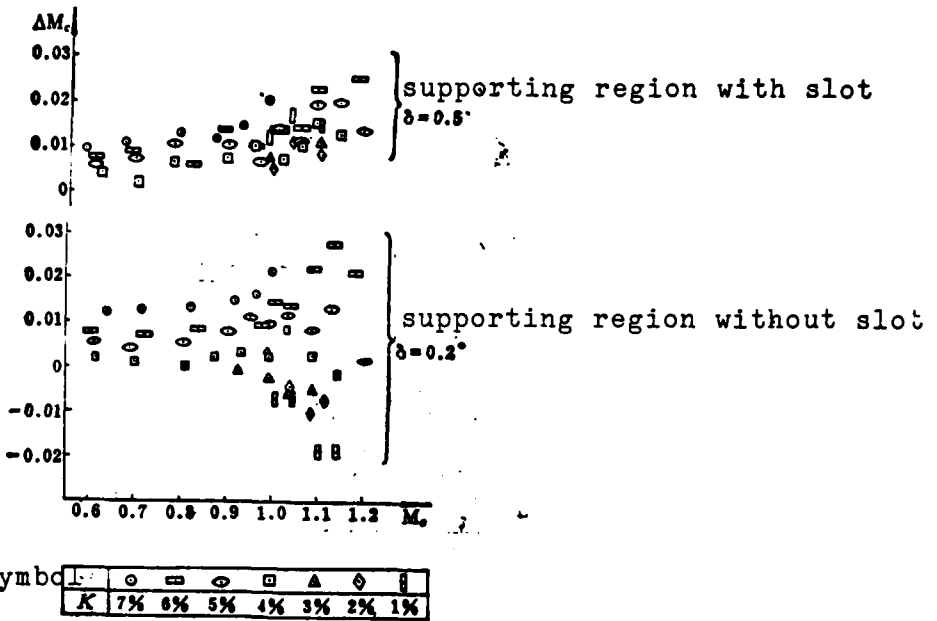


FIG. 5: TYPICAL ΔM_c VALUES

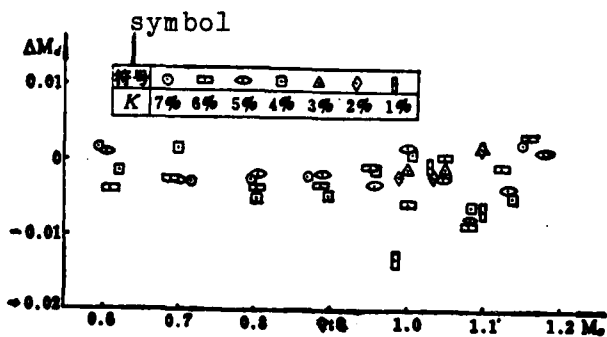


FIG. 6: MODEL EFFECT ON THE CALIBRATING MACH NUMBERS ($\delta=0.5^\circ$, supporting region with slot)

conducting 20 cone-cylinder model calibration tests, we also calibrated the model front of M_w (when $M \leq 1.05$, the calibration point is located in the center of the side wall of 155mm of the model top point front, when $M > 1.05$ M_w takes the side wall calibrated Mach num-

ber of the front of the model top shock wave). Through computing $M_d = (M_w - M_c)$ with model - $(M_w - M_c)$ without model of the corresponding calibration point that is obtained, such as Fig. 6 expresses.

As to the 20° cone-cylinder model where the plug ratio is 1%, notice that ΔM_d is not very large.

3. 20° Cone-Cylinder Model Calibration Test Results

General test results are shown in Fig. 7. In the figure, the solid line is the non-interference curve (refer to the photograph in material (6)); The test point corresponding M is the M_t that is arrived at by M_c seen in Fig. 5; not carried out ΔM_d correctly. Because the tail supporting shaft of this model is too short, in the figure the position of $x_1/D = 7$ is equal to $x = 900\text{mm}$, making the model back section of $x_1/D > 7$ receiving at different degrees the supporting effect (Refer to Fig. 3). Hereafter we will draft a longer tail supporting shaft to conduct tests.

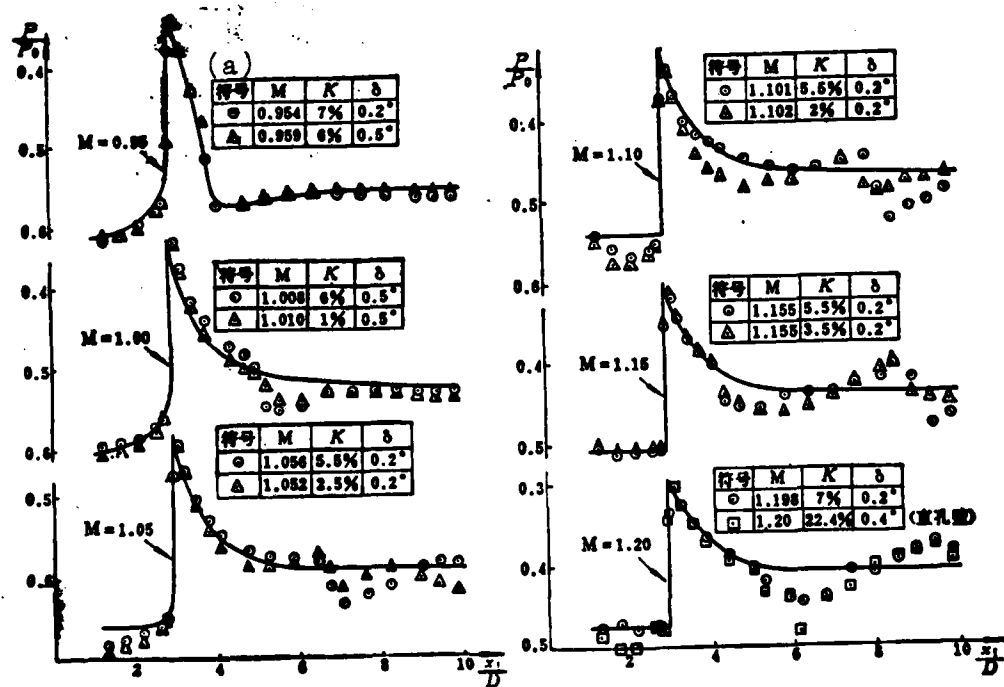


FIG. 7: PRESSURE DISTRIBUTION ON THE 20° CONE-CYLINDER MODEL
KEY: (a) symbol

When $M < 1$, $K = 5\%$ both can obtain relatively good pressure distribution that is with a non-interference curve (in agreement with literature (1) and (2)).

When $M \geq 1$, the expansion wave tunnel wall reflection back that the model shoulder section sends out becomes a compressed wave and reaches on the model (When $M=1$ it reaches $x_1/D=5.5$ approximately, when $M=1.15$ it reaches $x_1/D=9.5$ approximately). This shows that the porosity has enlarged. With the reduction of K value, this reflection wave weakens. The results when $M=1$ and of Fig. 9.21 of reference material (6) are close. But when number M is comparatively large, a four wall open hole wind tunnel emerges^(1,6) in which there are no contradictory phenomena. For example when $M=1.1$, with the reduction of K value, approximately $x_1/D=4$ emerges obvious compression. This is the result of the front section shock wave longitudinal tunnel wall reflexion becoming compression wave arriving on the model. This makes it clear to the front section shock wave, the K value is also too small. In addition, when $M=1.2$ and when K increases to 7% it still assumes a solid wall effect. We consider the primary reasons that these phenomena emerge are probably that this wind tunnel only has two wall holes. When $M=1\sim 1.05$, the K requirements to eliminate the waves are very small, the wave reflection of side wall production is not strong. With the increase of the Mach number, the K value that is required to eliminate waves is also very large, but the solid wall effect of the two sides then becomes more and more striking. In the tests we also calibrated pressure distribution of certain points on each line of the left and right sides of the 20° cone-cylinder model and discovered that the pressure distribution of each line from top to bottom is basically alike. When the K value of the whole wall changes, the pressure distribution of each line simultaneously changes. From the reflection wave system of the four walls, before arriving on the model, we see that they already passed through a series of complex mixed processes (but this is not a simple counteraction relationship).

4. AGARD-B Standard Calibration Test Results

In order to make clear the effect of variable porosity on

conventional calibration tests, we yet carried out three kinds of AGARD-B standard calibration tests⁽⁷⁾. The plug ratio of the model in the test section is 0.71%. The wall plate expanse angle is 0.2°, porosity variation regulations are shown in Fig. 8. Regulation A is with porosity fixed at 6%, regulation C is the proposed applied porosity value based on previous flow field calibration and 20° cone-cylinder model test results. Regulation B is situated between A and C.

Typical test results are shown in Fig. 9. In order to make comparison, Fig. 9 separately draws the test results of this tunnel in 1974 using $K=22.4\%$ straight hole wall and the combined calibration results of each wind tunnel inside the country and foreign standard model calibration curves. By the figure we can see:

- (1) The porosity wall test results of $K=6\%$ and the straight porosity wall test results of $K=22.4\%$ are balanced.

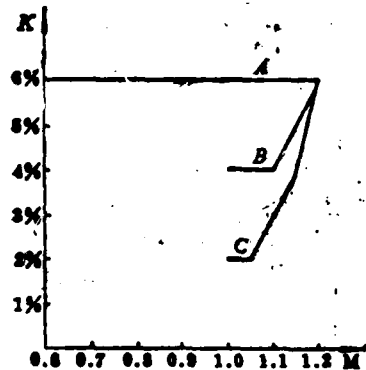


FIG. 8: VARIATION OF POROSITY WITH MACH NUMBER

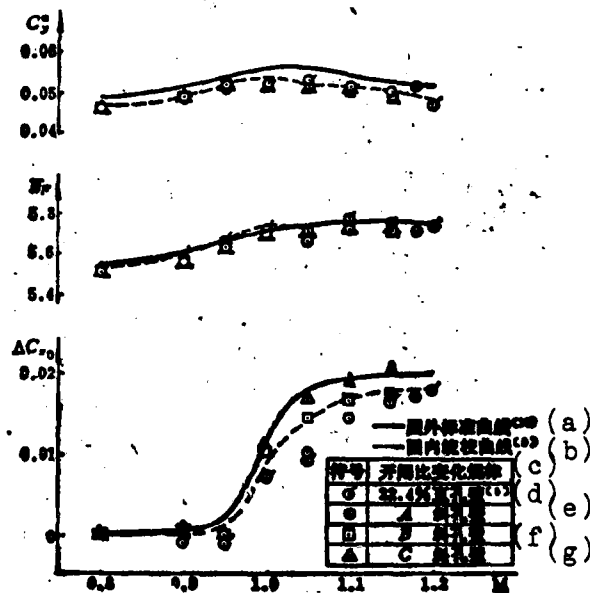


FIG. 9: TEST RESULTS OF THE AGARD-B CALIBRATION MODEL
KEY: (a) Foreign calibration curve;
(b) China calibration curve; (c) Variable porosity regulation; (d) straight hole wall; (e,f,g) hole wall.

(2) When porosity is close to regulation C, ΔC_x is clearly close to no plug interference value. The reason can possibly be: when K value is comparatively large, the expanded wave longitudinal tunnel wall reflection that the model front section sends out is compressed and arrives on the model back section (See Fig. 7), using the pressure lift of the wing back section, and resistance reduces. With the reduction of K value, the above-mentioned reflective wave weakens. When we arrive at regulation C, the model back section, although not completely at a non-interference state, the model front section pressure has raised (See Fig. 7). Both have a comprehensive effect, causing resistance to increase to non-interference value. In the calibration test suitable to variable porosity we see that we can reduce the tunnel plug interference when $M > 1$.

(3) The influence of porosity variations to C_y^a and \bar{x}_F all are not noted. The reason could possibly be that AGARD-B standard test is not sensitive to tunnel wall lift disturbance, and there is no tail wing.

VI. CONCLUDING REMARKS

We in the up and down, two walls, with holes transonic wind tunnel test section carried out preliminary experimental research on variable porosity walls. Through experiments we preliminarily grasped some distinguishing features of the flow field when using variable porosity walls. The test results express variable porosity walls are beneficial to reduce tunnel wall plug interference when $M > 1$. But because there are only two walls with holes, when $M > 1$ it cannot eliminate the reflection wave system of the right and left side walls, and in the 20° cone-cylinder model calibration pressure test eliminating the wave effect is not ideal. We intend from now on to further develop the research on wing model calibration pressure tests.

Reference Literature

- (1) Felix, A. R., "Variable porosity walls for transonic wind tunnel." NASA TM X-63295.
- (2) Davis, J.W., "Optimization of wave cancellation in variable porosity transonic wind tunnel flows." NASA TN-D 7432.
- (3) NH-1 Feng Tong She Ji Yu Shi Yong. Nanjing Hang Kong Xue Yuan 1977.11. "Design and Use of the NH-1 Wind Tunnel, Nanjing Aeronautic Institute, 1977.11"
- (4) Zhang Qiwei, NH-1 Feng Tong Shi Yan Duan Bian Kai Bi Bi Kua Yin Su Bi Ban He Zheng Ti Chao Yin Su Bi Bang De She Ji. "Zhang Qiwei, Nanjing Aeronautical Institute, The design of the NH-1 Wind Tunnel Test Section Variable Porosity Transonic Wall Plate and Whole Supersonic Wall Plate, Nanjing Aeronautical Science and Technology Material Pneumatic Force Category No. 631."
- (5) Parker, R. L., "Flow generation properties of five transonic wind tunnel test section wall configurations." AEDC-TR-75-73.
- (6) Goethert, B.H., "Transonic wind tunnel testing." 1961.
- (7) Zhang Qiwei, Bian Kai Bi Bi Feng Tong Bi Dui AGARD-B Biao Mo Ce Li Shi Yan Jie Guo De Ying Xiang, Nan Hang Ke Ji Ze Liao Qi Dong Li Lei 769 Hao. "Zhang Qiwei, The Influence of Variable Porosity Walls on AGARD-B Model Calibration Test Results, Nanjing Aeronautics Science and Technology Material Pneumatic Force Category No. 769.
- (8) Zhang Jingzhen and Gu Jiajin, NH-1 Feng Tong Kua Chao Yin Su Biao Mo Shi Yan Bao Gao (1), Nanjing Hang Kong Xue Yuan, 1975. "Zhang Jingzhen and Gu Jiajin, Report on the NH-1 Wind Tunnel Trans and Supersonic Standard Test, Nanjing Aeronautic Institute, 1976.
- (9) Wang Fayang, Guo Nei Tong Feng Biao Mo Shi Yan Jie Guo Hui Ji, 7210 Xue Bao, 1979 Nian De 1 Qi. "Wang Fayang, Compiled Wind Tunnel Standard Test Results (from)Inside the Country, 7210 Journal, 1979, No.1".
- (10) Valk H. and Van der Zwaan J. H., "A review of measurements on AGARD calibration model B in the transonic speed range". NLP-MP. 197.

A NEW SIMULTANEOUS ITERATION ALGORITHM FOR EVALUATION OF EIGENPROBLEMS IN LARGE STRUCTURES

Liu Guoguang and Li Junjie, Aircraft Structural Mechanics Research Institute

Abstract:

A new improved algorithm of simultaneous iteration is presented for evaluation of generalized eigenproblems in dynamic analysis of large structures. The convergence of this algorithm is proved by the concepts of E_k subspace and eigendirection and some details of how to perform this algorithm in computer are discussed.

Based on statistics of computational quantity required for each step of iteration and a great number of practical computations, it is shown that in convergence rate the present method is comparable to some simultaneous or subspace iteration algorithms available up to now, but it can cut down the computer run time for each step of iteration and raise the computation efficiency.

I. FORWARD

The eigenproblem in structure dynamic analysis, after passing through some strange treatment (for example primary point displacement) its model is:

$$Kx = \lambda Mx \quad (1)$$

In which K and M are n exponent solid symmetry positive fixed and scattered distance. The eigenvalue of the present design system (1) is $\lambda_1, \lambda_2, \dots, \lambda_n$. Moreover, there is:

$$0 < \lambda_1 < \lambda_2 < \dots < \lambda_n \quad (2)$$

The corresponding eigen vectors are x_1, x_2, \dots, x_n .

As to large structures, the exponent number of system (1) can be raised to several thousand. Under this kind of condition, using the scattered characteristics of K and M will be extremely necessary.

Therefore, simultaneous iteration algorithm already becomes one of the strong powerful methods of evaluating the section lower level eigen face (eigen value and corresponding eigen vector) of system (1). Previously, the structure algorithm method put forward by Rutishauser, McCormick, Bathe, and Nicolai was prevalent. Among them the previous two kinds of algorithm were conducted by Cholesky on resolution to M, later again turned system (1) into a standard eigenproblem $Ay=\lambda y$ solution. If we don't consider the production error influence by resolution of M, using this kind of algorithm solution system (1) section eigenproblem also is not beneficial (See Table 4). This is not only because the resolution of M in itself will waste a certain amount of machine time, but also because resolution "pack" will be able to produce new non-zero elements, and therefore after it is used each step of iteration increases a certain amount of computer run time, thereby effecting computer efficiency.

Additionally, the algorithm of Reinsch and Nicolai used Gram-Schmidt perpendicular process, and therefore we can stop the already weakened test vector and not again add later iteration. This treatment technique^[2] is generally called the "reduced dimension" treatment. When the number of treated eigen faces is comparatively large, using the reduced dimension treatment can greatly raise computer efficiency (See Table 6).

This text gives a new, improved algorithm and is comparative to the preceding algorithm, aside from the unresolved M and the useable reduced dimension treatment, it yet has the primary characteristic of further reducing each step of iteration that wastes computer run time.

In the following section we will simply explain the E_k subspace concept of system (1) to prove the basic theory of convergence provided. The third section explains some certain particular problems of algorithm and recounts some aspects realized in the computer. Method comparisons and numeric value test results will be given separately in the two sections 4 and 5.

We will use capital letters to express matrix. Especially, we will use R to express the upper triangle matrix, and use r_{ij} to express its (i, j) elements. We will use D to express the matrix to the angle, and d_{ij} to express its j diagonal elements. We will use X, Y, Z, and S to express $n \times p$ vector matrix, and separately use x_j , y_j , z_j , and s_j to express their j series of vectors. We will use the capital letter O to express the same exponent small mass.

II. THE SUBSPACE OF E_k IN SYSTEM (1)

Assuming $x_1^{(o)}, x_2^{(o)}, \dots, x_p^{(o)}$ as in the n dimension subspace holding a linear, non related vector form. If E_0 is the subspace that they opened, then the E_k subspace of system (1) can be defined as:

$$E_k = \{x | Kx = My, y \in E_{k-1}\} \quad (3)$$

By the positive fixed symmetry of K and M we can know that the dimension of the E_k subspace to the arbitrary k all is p. Moreover $\lim_{k \rightarrow \infty} E_k$ exists, and is an unvariable subspace of system (1). If it is by the front of system (1) p lower level eigen vector x_1, x_2, \dots, x_p opened, then it calls E_k to be a stable convergent.

In this theory, under stable convergent conditions, on E_k all we can find to call it is the best direction of p vector $u_1, \dots, u_p^{(1)}$, and we have:

$$\|u_j - x_j\| = O(q^j) \quad (4)$$

Among which

$$q_j = \lambda_j / \lambda_{p+1} \quad (5)$$

Because there is no method to compute the best direction, every algorithm of the simultaneous iteration is p vector on E_k that goes through a form already known to compute a new vector $x_1^{(k)}, \dots, x_p^{(k)}$, to use when K is amply large, they gradually tend toward the favorable direction. Therefore:

$$\|x_j^{(n)} - x_j\| = O(q_j^n) \quad (6)$$

Here q_j is the same as in formula (5).

The preceding simultaneous iteration various algorithms, when computed on E_k have the preceding quality $x_j^{(k)}$, Each method used is different. The algorithm this text proposes will adopt of E_k the computation system:

$$(KM^{-1}K)x = \lambda^* Mx \quad (7)$$

the eigen vector $X_k = (x_1^{(k)}, \dots, x_p^{(k)})$, it satisfies that:

$$X_k^T M X_k = I, \quad (8)$$

$$X_k^T (KM^{-1}K) X_k = D_k^2 \quad (9)$$

In which D_k is p exponent matrix to the angle, and itself from start to finish assumes its diagonal element $d_{jj}^{(k)}$ to satisfy that:

$$d_{11}^{(k)} \leq d_{22}^{(k)} \leq \dots \leq d_{pp}^{(k)} \quad (10)$$

On E_k to compute the preceding X_k is not difficult (see the following section), and moreover this kind of X_k still has a following extremely important characteristic.

Theorem: Under stable convergent conditions, if X_k is the eigen direction of system (7) on E_k , then:

$$\|x_j^{(k)} - x_j\| = O(q_j^{(k)}) \quad (11)$$

$$|d_{jj}^{(k)} - \lambda_j| = O(q_j^{(k)}) \quad (12)$$

In which q_j is the same as in formula (5). For proof please refer to literature (1).

III. ALGORITHMS

In n dimensional space, assuming to take the beginning n x p matrix $S_0 = (s_1^{(0)}, \dots, s_p^{(0)})$, later we use the following iteration form to progressively produce a new S_k :

1. Evaluate the equations, to obtain Z_k :

$$KZ_k = S_{k-1}$$

2. Gram-Schmidt perpendicularization, to obtain Y_k and R_k :

$$MZ_k = Y_k R_k$$

$(Y_k^T M^{-1} Y_k = I)$, R_k is on the triangle.

3. Form given effect matrix B_k :

$$B_k = R_k R_k^T$$

4. Evaluate the eigenproblem of given effect matrix B_k :

$$Q_k^T B_k Q_k = D_k^{-1} \quad (D_k \text{ is the diagonal})$$

5. Form the next necessary step S_k :

$$S_k = Y_k Q_k \quad (13)$$

If in the above algorithms we make:

$$S_k = MX_k \quad (14)$$

then it is not hard to prove that X_k is the eigen direction in the E_k subspace in system (7). In fact,

$$X_k^T M X_k = Q_k^T Y_k^T M^{-1} Y_k Q_k = I, \quad (15)$$

$$X_k^T (KM^{-1} K) X_k = Q_k^T (R_k R_k^T)^{-1} Q_k = D_k \quad (16)$$

Therefore, by the above theorem we know that the convergence rate of algorithm (13) is (11) and (12). In fact, formulas (11) and (12) are the convergence rate of the preceding simultaneous iteration that each algorithm shares.

The following firstly explains some problems worthy to point out of algorithm (13) and of aspects realized in the computer. Later we use a flow chart (see Fig. 1) to describe the complete computation process.

1. Firstly, p test vectors are selected for use through a stochastic process ⁽²⁾, or selected through the Bathe method ⁽³⁾.

2. Iteration formula 2 is one which is brought about by

the Gram-Schmidt perpendicular process. In fact, if we make:

$$Z_k = X_k R_k \text{ (Gram-Schmidt perpendicular)} \quad (17)$$

In which $X_k^T M X_k = I_p$, R_k is the upper triangle matrix. The two sides of the above formulas simultaneously the remainder takes M and makes $Y_k = M X_k$, thus it is not difficult to prove:

$$Y_k^T M^{-1} Y_k = I_p \quad (18)$$

The computation of the related Y_k is shown in Fig. 1.

3. Because algorithm (13) can use the reduce dimension treatment technique, therefore while some certain test vectors in a short time satisfy the convergence conditions, we will not again let them add later iteration. But due to the reason for computation error, in the later iteration, we still must on the other test vectors "purify" and shed these already converged vectors. Additionally, we yet must point out the B_k exponent of algorithm (13) will continually reduce with the increase of already converged numbers of test vectors. The upper triangle matrix R_g in Fig. 1 is the left lower angle $p-q$ exponent matrix of the p exponent upper triangle matrix $R = (r_{ij})_0$. Its g is an already converged eigenface number.

4. After iteration step 1, when the obtained q eigenface are completely converged, the diagonal element $d_{jj}^{(1)}$ in D_1 is simply the similar eigen value λ_j , and the series $s_j^{(1)} (j=1, 2, \dots, g)$ of S_1 still is not the similar vector $x_j^{(1)}$ of the eigen value x_j , but it is not difficult to see that the two have the following relationship:

$$s_j^{(1)} = M x_j^{(1)} \quad (j=1, \dots, q) \quad (19)$$

In order to obtain $x_j^{(1)}$ we still must make the following few operations:

$$M x_j^{(1)} = s_j^{(1)} \quad (20)$$

$$x_j^{(1)} = d_{jj}^{(1)} s_j^{(1)} \quad (j=1, \dots, q) \quad (21)$$

Generally, test vector number p is determined by the following equation:

$$p = \min\{q + s, 2q\} \quad (22)$$

5. Criterion for convergence can be referred to in literature (2) and (8). The criterion for the proposed effect in literature (8):

$$\left| \frac{d\mathbf{y}^j - d\mathbf{y}^{j-1}}{d\mathbf{y}^{j-1}} \right| < \epsilon^2 \quad (23)$$

In which ϵ is the allowable error of the eigen vector.

6. X, Y, Z, and S in the flow chart can apply the identical storing up position.

7. Because various algorithms of simultaneous iteration all can apply multiple sum formula or primary point displacement to conduct acceleration, it is not recounted again in the flow chart. The interested reader can refer to material 1, 2, and 6.

8. Because the M formation in the iteration process remains invariant, the proposed effect eliminates the compressed storage method of the whole zero element.

IV. METHOD COMPARISON

In this section, we will compare the algorithm in the text with several other frequently used algorithms. Before we compare, we first will explain several points:

1. Assuming b_k and b_m separately to be the half tape width of K and M. Although in the algorithm of the unresolved M, M can program storage according to compression, but in order to still make it convenient we still use b_m to count operational quantity.

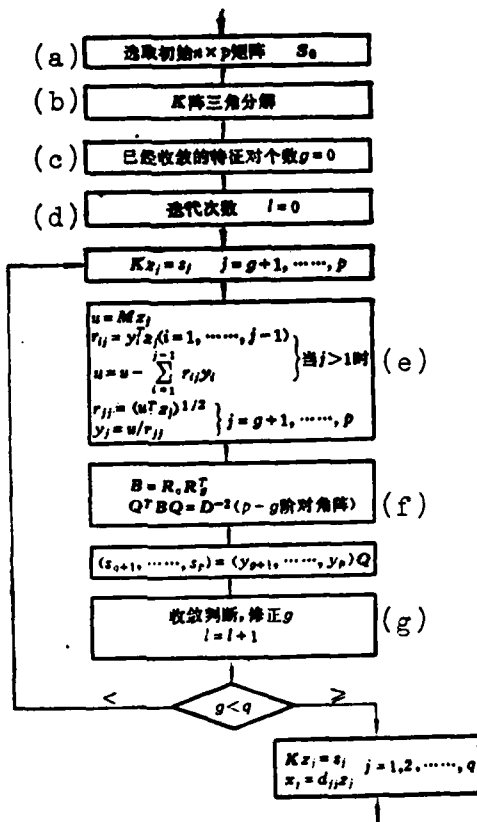


FIG. 1: FLOW DIAGRAM FOR THE PROPOSED ALGORITHM

KEY: (a) Selected first nxp matrix; (b) K formation triangle solution; (c) Already converged eigenface number $g=0$; (d) iteration frequency; (e) When $j>1$; (f) $(p-g)$ exponent to the angle formation); (g) Convergence determination, revised g .

2. In the algorithm in which we can use the "reduce dimension" treatment, when counting each step of the computational quantity, we use the equal value method. If we assume a convergence that already has i eigenface, at this moment the computational quantity for each step of iteration is $T(p-i)$, then the average computational quantity for each step of iteration is:

Algorithm	Rutishauser ⁽¹⁾	Reinsch ⁽²⁾	McCormick ⁽³⁾	Nicolaie ⁽¹⁰⁾	Bartels ⁽⁵⁾	Proposed
Iteration Formula	$AZ_k = Y_{k-1}$ $B_k = Z_k^T Z_k$ $Q_k^T B_k Q_k = D_k^{-1}$ $Y_k = Z_k Q_k D_k$	$A\bar{Z}_k = Y_{k-1}$ $\bar{Z}_k = Z_k R_k$ $(Z_k^T Z_k = I_{R_k})$ $B_k = R_k R_k^T$ $Q_k^T B_k Q_k = D_k^{-1}$ $Y_k = Z_k Q_k$	$KZ_k = MX_{k-1}$ $B_k = Z_k^T M Z_k$ $(Z_k^T M Z_k = I_{R_k})$ $X_k = Z_k Q_k D_k$	$K\bar{Z}_k = MX_{k-1}$ $\bar{Z}_k = Z_k R_k$ $(Z_k^T M Z_k = I_{R_k})$ $X_k = X_k^T \cdot Z_k$ $M_k = Z_k^T Y_k$ $B_k = R_k R_k^T$ $Q_k^T B_k Q_k = D_k^{-1}$ $X_k = Z_k Q_k$	$KZ_k = X_{k-1}$ $Y_k = MZ_k$ $(Y_k^T M^{-1} Y_k = I_{R_k})$ $M_k = X_k^T \cdot Z_k$ $K_k Q_k = M_k Q_k D_k$ $X_k = Y_k Q_k$	$KZ_k = S_{k-1}$ $MZ_k = Y_k R_k$ $(Y_k^T M^{-1} Y_k = I_{R_k})$ $B_k = R_k R_k^T$ $Q_k^T B_k Q_k = D_k^{-1}$ $S_k = Y_k Q_k$
Resolution of M	Resolved $M = LL^T$ $A = L^{-1}KL^{-T}$ $Y = L^T X$	Resolved $M = LL^T$ $A = L^{-1}KL^{-T}$ $Y = L^T X$	Unresolved	Unresolved	Unresolved	Unresolved
Dimension Treatment	unable to use	able to use	unable to use	able to use	unable to use	able to use
Projecting Matrix Form	Standard	Standard	Standard	Standard	Generalized	Standard
Computation Quantity of Each Iteration	$2np(b_k + b_m)$ $+ \frac{1}{2}np^2 + J(p)$	$np(b_k + b_m) + np^2$ $+ \left(\sum_{i=1}^p J(i) \right)/p$	$2np(b_k + b_m)$ $+ 2npb_m + np^2$ $+ \left(\sum_{i=1}^p J(i) \right)/p$	$np(b_k + b_m)$ $+ npb_m + np^2$ $+ \left(\sum_{i=1}^p J(i) \right)/p$	$2np(b_k + b_m)$ $+ 2np^2 + 2J(p)$	$np(b_k + b_m) + np^2$ $+ \left(\sum_{i=1}^p J(i) \right)/p$

TABLE 1: COMPARISON OF SEVERAL ALGORITHMS

$$\frac{\sum_{i=0}^{p-1} T(p-i)}{p} \quad (24)$$

3. We use $J(p)$ to represent the computational quantity that uses the whole eigenproblem for evaluating symmetrical matrix p . We use $2J(p)$ to similarly represent the computational quantity of corresponding generalized eigenproblems.

Examples of comparative conditions of several algorithms are given in Table 1.

From the table we can clearly obtain the following conclusions:

The algorithm proposed in this text

1. makes resolution with the first order M formation less than the algorithms of Rutushauer and Reinsch. Moreover, when M is in accordance with the compression program storage, the computational quantity of each step of iteration in reality must be less than the computational quantity of Reinsch.

2. in each iteration step, is less than the algorithms of McCormick and Nicolai in making the product of the first order M formation and the test vector.

3. is comparable to Bathe's algorithm, except that it can carry out the reduce dimension treatment, and doesn't need each step of iteration to evaluate the generalized eigenproblem of p .

V. NUMERIC VALUE TESTS

In order to test the dependability and efficiency of the algorithm in this text, we applied FORTRAN language on a SIEMENS-7760 computer and did numeric value test operations of many areas. Now we will list examples of related conclusions.

1. Computed Example 1: Applying the Reisch method and the method of this text, we computed the eigenproblems of certain complete aircraft. The main point of this computed example is the convergence method that is used to compare the two methods (See Table 2) and the conclusion precision (See Table 3). The test vectors that this computed example used were 25, and obtained 17 eigenfaces. The 17 eigen values that were required only had differences measured in the tenth place (on the tens place after the decimal point), and limited by length were not again listed in the table.

<u>Iteration frequency</u>	1	2	3	4	5	6	7	8	9	10
Convergence number	0	0	0	0	4	14	15	17		
Reinsch	0	0	0	2	11	15	16	16	17	

TABLE 2: COMPARISON OF REINSCH'S ALGORITHM WITH THE PROPOSED ONE

2. Computed Example 2: Exponent is 500; half tape width of K and M is 301. This computation is mainly used to assess the computer efficiency of each algorithm. It uses 13 test vectors and computes 5 eigenface (See Table 4).

<u>Eigenvector sequence number</u>	1	2	3	4	5	6	7	8
This text _(10⁻⁴)	0.0064	0.0143	0.0559	0.0062	0.0830	0.0403	0.0064	0.0007
Reinsch _(10⁻⁴)	0.0100	0.1231	0.0653	0.0040	0.0188	0.0251	0.0219	0.0447

TABLE 3: COMPARISON OF REINSCH'S ALGORITHM WITH THE PROPOSED ONE IN EIGENVECTOR ACCURACY.

<u>Algorithm</u>	Ratishauer	Reinsch	McCormick	Nicolai	Bathe	Text
Time-seconds	1106	1000	992	978	780	758

TABLE 4: COMPUTER RUN TIME OF SEVERAL ALGORITHMS

3. Computed Example 3: Separately uses Bathe's algorithm and the proposed one to compute three eigenproblems. This example was computed in order to confirm that this text's algorithm has higher efficiency than Bathe's when the required eigenface are comparatively many (See Table 6).

Problem	Exponent	Half Tape Width	Test Vector Number	Required Eigenface Number
1	100	5	30	25
2	200	20	33	25
3	500	10	38	30

TABLE 5: PARAMETERS FOR THREE PROBLEMS

Problem	1	2	3
This text-seconds	93	234	558
Bathe-seconds	194	383	986

TABLE 6: COMPARISON OF BATHE'S ALGORITHM WITH THE PROPOSED ONE IN COMPUTER RUN TIME

VI. CONCLUSION

This text proposed simultaneous iteration improved algorithm, proved its convergency rate, discussed the problem of performing this algorithm in the computer, and made comparisons with several frequently used simultaneous iteration algorithms. We can conclude, the scale and dimensions of system (1) and the tape width are exceedingly large. Comparison of the proposed algorithm's computer efficiency with those of Rutishauser, Reinsch, McCormick, and Nicolai then is also exceedingly high, and the required eigenface of system (1) are many. The computer efficiency of the proposed algorithm compared with Bathe's algorithm is exceedingly high.

In the research period of this method, we obtained Comrade Guang De's concrete guidance and support, and obtained the help of Li Guang-

quan. In this we deeply express our gratitude.

Reference Literature

- (1) H. Rutishauser, Computational aspects of F. L. Bauer's simultaneous iteration method, *Numer Math* 13, 4-11, 1969.
- (2) H. Rutishauser, Simultaneous iteration method for symmetric matrices, *Numer Math* 16, 205-223, 1970.
- (3) A. Jennings, A direct iteration method for obtaining the largest roots and vectors of symmetric matrix, *Proc. Comb. Phil. Soc.*, 63, 755-765, 1967.
- (4) M. Clift and A. Jennings, The evaluation of eigenvalues and eigenvectors of real symmetric matrices by simultaneous iteration, *Computer J.*, 13, 76-80, 1970.
- (5) R. B. Corr and A. Jennings, A Simultaneous iteration algorithm for symmetric eigenvalue problems, *Int. J. Num Meth. Engng.* 10, 647-663, 1976.
- (6) Yamamoto and Ohtsubo, Subspace iteration accelerated by using Chebyshev polynomials for eigenvalue problems with symmetric matrices, *Int. J. Num Meth. Engng.* 10, 935-944, 1976.
- (7) K. J. Bathe and E. L. Wilson, Large eigenvalue problems in dynamic analysis, *J. Engng Math. Div.*, *Proc. ASCE EM6*, 1471-1485, 1972.
- (8) K. J. Bathe and E. L. Wilson, *Numerical Methods in Finite Element Analysis*, Englewood Cliffs, 1976.
- (9) S. P. McCormick and T. Noe, Simultaneous iteration for the matrix eigenvalue problem, *J. Linear Algebra & its Application*, 16, 43-56, 1977.
- (10) P. J. Niclai, Eigenvectors and eigenvalues of real generalized symmetric matrices by simultaneous iteration, *ALGORITHM 538 Collected Algorithms from ACM*, 1979.

SOME PROBLEMS OF PLATE BENDING HYBRID MODEL WITH SHEAR EFFECT

Wu Changchun, Chinese University of Science and Technology

Abstract:

A triangular plate bending hybrid element is constructed according to Reissner's principle. It has 9 degrees of freedom and takes the shear effect into account. The C⁰ formulation of the thick plate is extended to the thin plate and the "shear locking" phenomenon can be avoided through imposing the discrete type of Kirchhoff's constraints. It is interesting to note that the kind of discrete constraints can be directly imposed by means of Hermite interpolation. This is one of the features which distinguish the paper from ref. (5) and (1). On the other hand, the specific matching between bending and shearing is discussed in the analysis of the thick plate. It is shown that the reasonable matching between bending and shearing complementary energies may be destroyed by inhomogeneous magnification of the discretization errors. Furthermore, a principle of energy regulation is put forward, with the aid of which this matching problem is effectively treated so that the unified analysis of the thick and thin plates is achieved. Finally, numerical examples are given.

I. FORWARD

In recent years, the limited primary analysis of hard plate with shear effect and the general primary research of thick plate construction is receiving more and more serious attention. This is no doubt because the deserved question for discussion has extensive practical value. But what is even more important is in view of its theoretical significance. The essence of this kind of research is the problem of using the simplified C⁰ sample to approach the C¹ category.

As to the displacement method, the key of constructing commonly used elements lies in wanting to make the thick plate formula independently selected deflection field ω and corner θ , able to automatically satisfy the zero shear strain thin plate time condition:

$$\gamma_j = \theta_j + \omega_j = 0 \quad (1)$$

Otherwise the so-called shear locking phenomenon will be able to emerge and bring about an ordinary solution. Various limited model problems all can emerge from this kind of condition⁽¹⁾.

In order to bring about the thin plate constraint (1), we can use ω , γ_j , and their derivatives as basic variables⁽²⁾, define the independent deflection field and shear strain field, and the corner thus is defined by formula (1). This way, when plate thickness $h \rightarrow 0$, shear rigidity tends toward ∞ , and naturally we have the result of $y_j \rightarrow 0$. Literature^{(3) and (4)} thus acquire very great success. Their inadequacy is that they gain numerous and jumbled units. Their rigid matrices separately are 20 and 36.

As to Kirchhoff's constraint (1), if it can't be strictly satisfied, then the discrete type of Kirchhoff's constraints can be implemented. In literature⁽⁵⁾ the best selection proposes the concept of discrete Kirchhoff assumptions, causing formula (1) to only be implemented in the unit's section point place, thus we take the sample of the C° type and successfully apply it to the thin plate bending problem of the C' model. But because this method must omit shearing deformation, it is not suitable to thick plates.

Rationally utilizing the reduction integral method is helpful to resolve the thick-thin plate problem. Literature⁽⁶⁾ proposes that only in the energy function of matching plates can the shearing deformation part, if to the integral sum:

$$• \int \int (\theta_j + \omega_j)^2 dA \quad (2)$$

reducing the numeric value integral exponent, this therefore is the "selective reduction integral method". In this way we retard the rigidity problem of the unit when the plate is thick, and the integral sample point of the unit implements the discrete type of Kirchhoff constraint. If we regard the shear rigidity a in formula (2) as a penalty factor treatment, then the selective reduction integral method is simply the penalty function method⁽¹⁾. To make this kind of

method suitable to plates of different thick-thin proportions, we must select a different numeric value integral exponent and a different penalty factor value. Clearly this is an experiential, very strongly improvised process.

This text attempts to avoid the displacement method, and starting out from the thick plate mixed variable formula construct a current stress hybrid component of a shearing triangle. In this area, Cook⁽⁷⁻⁹⁾ has done forerunning work, systematically analyzed and compared this type of numeric value performance of elements. This text purports to further advance the work in this area.

II. GENERAL HYBRID ELEMENT OF 9 DEGREES OF FREEDOM-UH

Here we will directly give guidance to the unit rigidity matrix of the element, and various discussions will be carried out in each section remaining after. The Reissner functional equation of the shear effect is:

$$\begin{aligned} \pi' = & \int \int_{A^e} [(M_{ij}, \theta_{ji} + Q_j(\theta_i + \omega_i) - B_1(M_{ij}) - B_2(Q_j) - \bar{p}\omega) dA \\ & - \int_{C_e^s} [(\omega - \bar{\omega})Q_s + (\theta_s - \bar{\theta}_s)M_s + (\theta_s - \bar{\theta}_s)M_{ss}] ds \\ & - \int_{C_e^s} (\bar{Q}_s\omega + \bar{M}_s\theta_s + \bar{M}_{ss}\theta_s) ds \end{aligned} \quad (3)$$

Where B_1 and B_2 separately express the bending complimentary energy density and the shearing complimentary energy density of the plate element. For the significance of other symbols refer to literature {2}.

Utilizing the balanced equation $M_{ij},_i - Q_j = 0$ eliminates shearing stress, and makes partial integrals, when the geometric boundary conditions are satisfied, the entire functional equation of the dispersed system can be expressed as :

$$\begin{aligned} \Pi = & \sum_e \Pi'_e = \sum_e \left\{ - \int \int_{A^e} [(M_{ij},_{ji} + \bar{p})\omega + B_1(M_{ij}) + B_2(M_{ij},_j)] dA \right. \\ & \left. + \oint_{\partial A^e} (\bar{Q}_s\omega + M_s\theta_s + M_{ss}\theta_s) ds - \int_{C_e^s} (\bar{Q}_s\omega + \bar{M}_s\theta_s + \bar{M}_{ss}\theta_s) ds \right\} \end{aligned} \quad (4)$$

where $\tilde{Q}_e = M_{ij} \omega_{ij}$ is the weight of the vector of the element boundary point outside the unit. If we ensure the continuity of the element common boundary point $\tilde{\omega}_e$ and $\tilde{\theta}_e$, then by the fixed common conditions $\tilde{\theta}_e = 0$ we can obtain the crosswise balanced equation of the plate element, geometric equations, and surface mechanics boundary conditions. Aside from this, we still will obtain the balanced condition of the element common boundary pressure point⁽¹⁰⁾. Reflecting this, we can apply the dividing continuous internal force field to formula (4).

According to what Fig. 1 expresses, each variable referred to can define the following test solution fields:

The linear moment of force field in the element*

$$\begin{aligned}\{M_{ij}\} &= \{M_x, M_y, M_{xy}\}^T = (\Phi)\{\beta\} \\ \{\beta\} &= (\beta_1, \beta_2, \dots, \beta_6)^T \\ (\Phi) &= \begin{bmatrix} 1 & x & y & 0 & 0 & 0 & 0 & 0 & 0 \\ 0 & 0 & 0 & 1 & x & y & 0 & 0 & 0 \\ 0 & 0 & 0 & 0 & 0 & 0 & 1 & x & y \end{bmatrix}\end{aligned}\quad (5)$$

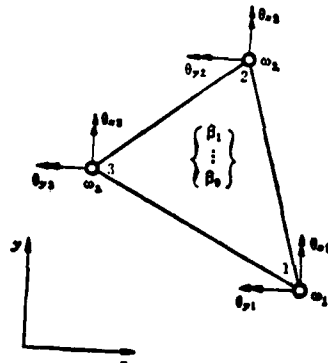


FIG. 1: PARAMETERS AND NODAL VARIABLES OF UH MODEL

*When M_{ij} obtains linear dispersion, M_{ij}, i, j in formula (4) then dissolves. At this moment formula (4) is equivalent to the improved complimentary energies function formula that the following study earliest applies.

The cubic deflection deflection field on the element boundaries:

$$\{\omega\} = [\tilde{\omega}_{11} \tilde{\omega}_{21} \tilde{\omega}_{31}]^T = (\tilde{N})\{\delta\} \quad (6)$$

and

$$\{\delta\} = [\omega_1 \theta_{x1} \theta_{y1} \omega_2 \theta_{x2} \theta_{y2} \omega_3 \theta_{x3} \theta_{y3}]^T$$

Here $\tilde{\omega}_{ij}$ expresses the ω dispersment of the element i-j side, and it is taken as:

$$\tilde{\omega}_{ij} = H_{ij}\omega_i + H_{ji}\omega_j + \bar{H}_{ij}(\theta_i) + \bar{H}_{ji}(\theta_j), \quad (7)$$

Here H_{ij} , \bar{H}_{ij} , etc. are the cubic Hermite interpolation value function. The linear directional rotational angle and the linear torse angle field of the element boundaries separate into:

$$\{\theta_s\} = [\theta_{s11} \theta_{s21} \theta_{s31}]^T = (N_s)\{\delta\} \quad (8)$$

$$\{\theta_r\} = [\theta_{r11} \theta_{r21} \theta_{r31}]^T = (N_r)\{\delta\} \quad (9)$$

By formulas (5)~(9) we yet can deduct the following matrix formulas:

The directional bending matrix and torse matrix on the element boundaries separately are:

$$\{M_s\} = (\Phi_s)\{\beta\} \text{ 和 } \{M_r\} = (\Phi_r)\{\beta\} \quad (10)$$

The bending complimentary energy:

$$B_s(M_{ss}) = \frac{1}{2} \{\beta\}^T (\Phi)^T \frac{12}{Eh^3} [C] (\Phi) \{\beta\} \quad (11)$$

$$[C] = \begin{bmatrix} 1 & -v & 0 \\ -v & 1 & 0 \\ 0 & 0 & 2(1+v) \end{bmatrix} \quad (12)$$

If we remember that $\{M_{sr}\} = (\Phi')\{\beta\}$, then the shearing complimentary energy expression is:

$$B_s(M_{sr}) = \frac{1}{2} \{\beta\}^T (\Phi')^T \frac{a}{Gh} (\Phi') \{\beta\} \quad (13)$$

In which $G = E/2(1+v)$, a is the shearing force coefficient (normally taking the value $6/5$). The constant shearing force field on the element boundaries:

$$\begin{aligned}\{\bar{Q}_e\} &= (\bar{Q}_{e11} \ \bar{Q}_{e22} \ \bar{Q}_{e31})^T = (I_m) (\Phi') \{\beta\} \\ (I_m) &= \begin{bmatrix} l_{11} & m_{12} \\ l_{22} & m_{22} \\ l_{31} & m_{31} \end{bmatrix} \quad (14)\end{aligned}$$

l_{ij} and m_{ij} are the exterior normal line direction cosine of element i-j side.

With (5)~(14) substitute (4) to obtain:

$$\pi' = -\frac{1}{2} \{\beta\}^T (H_{ss}) \{\beta\} + \{\beta\}^T (H_{se}) \{\delta\} - \{G\}^T \{\delta\} \quad (15)$$

$$(H_{ss}) = \iint_A \left(\frac{12}{Eh^3} (\Phi)^T (C) (\Phi) + \frac{a}{Gh} (\Phi')^T (\Phi') \right) dA \quad (16)$$

$$(H_{se}) = \oint_{\partial A'} ((\Phi')^T (I_m)^T (\bar{N}) + (\Phi_s^T) [N_s] + (\Phi_e^T) [N_e]) ds \quad (17)$$

$$\{G\}^T = \iint_A \bar{p}(N) dA + \int_{C'_e} ((\bar{Q}_e)^T (\bar{N}) + (\bar{M}_e)^T [N_e] + (M_e)^T [N_e]) ds \quad (18)$$

Formula (18) is the equivalent point load vector, $\{N\}$ is the torque value matrix of the ω field inside the element. This internal ω field is desirable for abic dispersment and boundary ω dispersment to be mutually alike, but according to the principle of the partial sum approach², it is also desirable as simplified linear dispersment.

By the fixed constant conditions of formula (15) we can obtain the formula for the element internal force and the balanced formula:

$$\begin{aligned}\{\beta\} &= (H_{ss})^{-1} (H_{se}) \{\delta\} \\ (H_{se})^T \{\beta\} &= \{G\} \quad \left. \right\} \quad (19)\end{aligned}$$

Eliminating $\{\beta\}$ we then obtain $\{K\} \{\delta\} = \{G\}$, in which the element rigid formation (9x9):

$$[K] = [H_{\theta\theta}]^T [H_{\theta\theta}]^{-1} [H_{\theta\theta}] \quad (20)$$

III. THE DISCRETE TYPE OF KIRCHHOFF CONSTRAINT AND GENERALIZATION OF MODEL FORMULAS

In the above section, the ω field of the element boundaries adopted the cubic Hermite interpolation value (7), this signifies in point i we have:

$$(\theta_i)_i = -\left(\frac{\partial \omega}{\partial x}\right)_i, \quad (\theta_j)_j = -\left(\frac{\partial \omega}{\partial y}\right)_j, \quad (21)$$

The detailed dividing yet strengthening with the network of this kind of Kirchhoff constraints is equivalent to the numeric value techniques in literature [1 and 7]. Both use the discrete formula to implement thin plate constraints (1), only however here the treatment is even more simplified and more direct.

Under the conditions of extremely thin plates, the UH element also cannot emerge to solve the difficulty of the locking phenomenon or the numeric value abnormal state. A living example of numeric value gives the thick span ratio as the UH solution of extremely thin plate of 1/10000. We can see that the numeric value is stable, the precision is good, and the reduced integral method under extreme con-

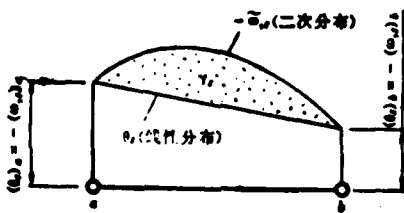


FIG. 2: DISTRIBUTION OF DISPLACEMENT SAMPLE ON THE ELEMENT BOUNDARIES

ditions of thin plate of $h \rightarrow 0$ is difficult to obtain dependable numeric value results.

We want to analyze the use of thick plate with the stress hybrid model. We must satisfy the following few conditions:

1. The computation of the shearing complimentary energy;
2. The independence of test solution θ , and $\tilde{\omega}$;
3. The matching relationship of rational winding-shearing.

As to the UH element of this text, the preceding condition "1" clearly can be satisfied. As to condition "2", by Fig. 2 we can see, because along the element boundary ab, $\tilde{\omega}$ takes cubic interpolation, $\tilde{\omega}$, then is quadratic distribution and test solution θ , thus is linear distribution. In this way, fully at point a and b constraint (1) is brought on. But on the whole element boundary section, $\gamma_r = \theta_r + \tilde{\omega}_r \neq 0$, this then ensures the independence of the UH element test solution θ , and $\tilde{\omega}$. The hybrid element HTC in literature (9) in the same way uses the cubic deflection field (7); but the above element is not applicable to thick plate distribution because its corresponding direction rational angle definition is $\theta_r = \tilde{\omega}_r$ on the whole element boundary, therefore condition "2" is violated. In the next section we will carry out discussion of condition "3".

IV. PRINCIPLES OF MATCHING BETWEEN BENDING AND SHEARING AND ADJUSTMENT OF ENERGY

The problems of the matching relationship of the hybrid model exists in two areas. Firstly, if a stress hybrid element increases the number of the internal force coefficient B, that then will increase the rigidity of the element, and the exponential order of the test solution that raises the displacement then will increase the degree of flexibility of the element. Therefore the problem exists of matching an internal force and exponential order of displacement. It is common knowledge that this matching must satisfy the so-called order condition⁽¹¹⁾, otherwise mobil deformation will emerge and thus zero energy model state.

As to thick plates, the problem will become even more complicated. Equation (16) can be expressed as :

$$(H_{\text{m}}) = \frac{12}{Eh^3} ((H_1) + \alpha h^2 (H_2)) \quad (22)$$

In which

$$(H_1) = \iint_A (\Phi)^T (C) (\Phi) dA \text{ 和 } (H_2) = \frac{1+v}{6} \iint_A (\Phi')^T (\Phi') dA$$

Separate and complimentary energies B_1 and B_2 are mutually corresponding. Remember the discrete errors of these two discrete matrices rising are R_1 and R_2 , thus the equation for the total complimentary energies of the element can be expressed as:

$$\begin{aligned} \iint_A (B_1 + B_2) dA &= -\frac{1}{2} \frac{12}{Eh^3} [(\beta)^T (H_1) (\beta) + R_2] \\ &\quad + \alpha h^2 ((\beta)^T (H_2) (\beta) + R_1) \end{aligned} \quad (23)$$

Clearly, the shearing complimentary energy R_2 of the plate element will be amplified h^2 fold (corresponding to R_1). Moreover the plate, the more the discrete solution of the thick standard as to the deviation of the true solution, the larger. In short, the rational matching relationship of the bending complimentary energy and the shearing complimentary energy will meet with violation due to unequal amplification of the discrete error. Cook⁽⁷⁾ had a test solution for the same kind of displacement, changed to using a different internal force field and element form to construct four kinds of hybrid elements, among which only "H5" is commonly used with the thick plates, the reason being the imbalance of the bending-shearing match.

Generally speaking, the rigid characteristics of the preceding two kinds of variations of matching relationships to the hybrid element both have obvious effects. Therefore, if we can adjust the β coefficient to improve the element rigidity, we can also go through matching adjustments of B_1 and B_2 to improve the element rigidity. Clearly, the former is due to the limitations of receiving the order condition, the adjustable scope of β is very small. Moreover, the adjusted effect is not continuous. Contrarily, the latter under the conditions of unchanged displacement and internal force test solutions can in a very large scope continually improve the rigidity or flex-

ibility of the element. Based on this kind of consideration, we site the following energy adjustment principles.

As to the error sums of R_1 and $a h^2 R_2$ of equation (23), people have much difficulty directly controlling their proportion. But we can indirectly go through the adjustment to the shearing complimentary energy to equalize their influence. A simple and effective method is to change the factor α value in formula (22). If we make $0 < \alpha < 6/5$ then due to the unequal amplification of R_1 and R_2 causes the excess shearing complimentary energy to be reduced and consequently eliminated. The chosen value of α can be determined by a simple computation, to the UH element we can take $\alpha = 0.6$, if we make $\alpha = 0$, then there is no shearing effect; thus the UH conveniently deteriorates into the universal thin plate hybrid element.

V. COMPUTED EXAMPLES

To examine the general use of UH, we carried out comprehensive computations of the square plate that possesses various different thickness span proportions. By Fig. 3 we can clearly show the mechanism of the above-mentioned energy adjustment principles. In the figure the α condition solution curve of UH (dotted line) with $\alpha = 1.2 \rightarrow 0.6$ and gradually draws near to the thick plate theory solution curve. Henceforth, when $\alpha > 0$, the curve again gradually opens into a straight line and parallel or mutual with the thin plate theory solution. Clearly, the transformation of α is not sensitive to the effect of thin plate solution. The so-called energy adjustment can only be significant by raising the thick plate analysis of the controlled effect to the shearing effect.

Figure 3 simultaneously draws the boundary α field changing to be the solution curve of linear distribution time (dot-dash line). We can see that this simplified linear α test solution can be adopted to the thick plate, because it possesses C' continuity, moreover it ensures the independence of α and θ . But it does not completely satisfy Kirchhoff's constraints, therefore it is not applicable to

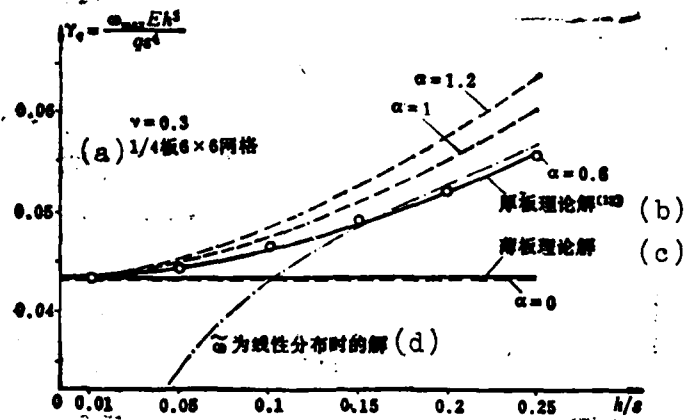


FIG. 3: CENTER DEFLECTION CURVES OF SIMPLY SUPPORTED SQUARE PLATE UNDER UNIFORM LOAD q

KEY: (a) 1/4 plate 6x6 mesh size; (b) Thick plate theoretical solution; (c) Thin plate theoretical solution; (d) Solution when ω is linear distribution.

thin plates, and consequently the left end of the corresponding solution curve of Fig. 3 follows the reduction of h to rapidly deviate the true solution and distribution. This converse example further explains the necessity in UH of implementing the discrete type of Kirchhoff constraints.

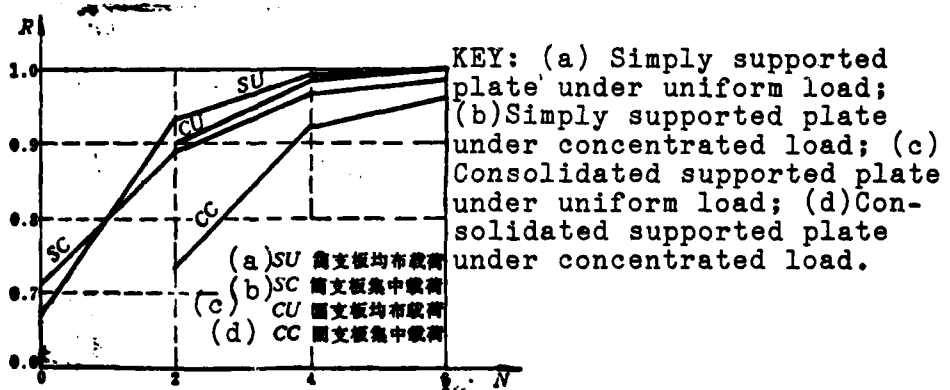


FIG. 4: CONVERGENCE CURVES OF SQUARE PLATE UNDER UNIFORM LOAD q AND CENTRAL CONCENTRATED LOAD P RESPECTIVELY ($h/s = 0.01$, N is the mesh size, R is the ratio of finite element solution (UH) to theoretical solution for ω_{max})

Tables 1~4 and Fig. 4 and 5 further express the various numeric value energies of the UH element. We can see that regardless of displacement or internal force UH uniformly gives satisfactory results.

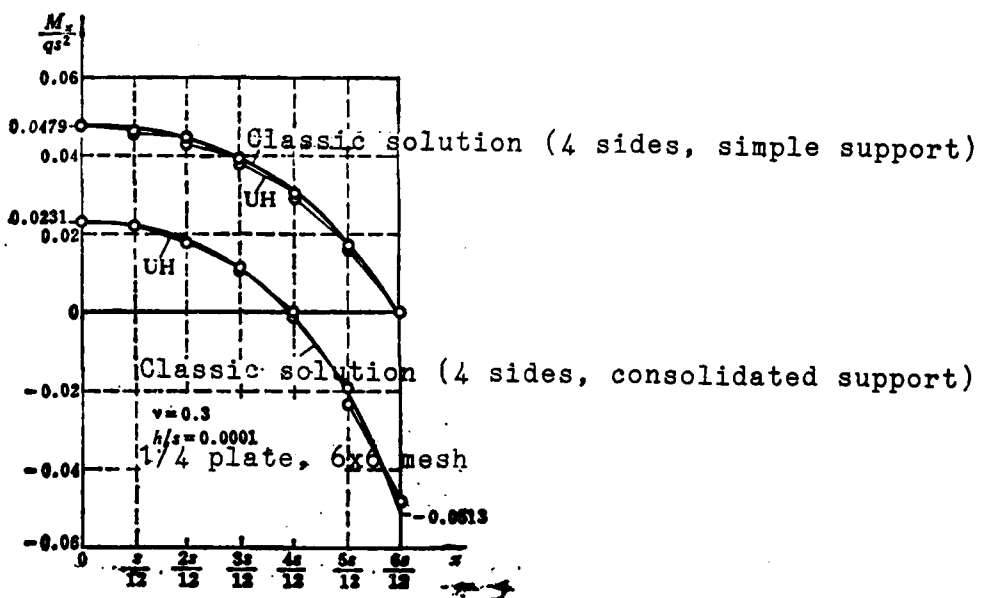


FIG. 5: DISTRIBUTION OF M_x ALONG CENTER LINE OF SQUARE PLATE UNDER UNIFORM LOAD

Thick-thin ratio $\frac{h}{s}$	Theory Solution		Hybrid Element		Suitable element	
	Classical thin plate	Reisner lit. 12	UH	Cook, Hs lit. 7	Pryor et al. lit. 3	Rao et al. lit. 4
0.0001	0.04437		0.04419		0.04423	
0.01	0.04437	0.04439	0.04422		0.04409	0.04433
0.05	0.04437	0.04486	0.04487		0.04469	0.04527
0.10	0.04437	0.04632	0.04669		0.04612	0.04656
0.15	0.04437	0.04876	0.04932		0.04852	0.04886
0.20	0.04437	0.05217	0.05256		0.05106	0.05201
0.25	0.04437	0.05656	0.05632	0.05620	0.05617	0.05631
1/4 plate mesh division → Point unknown mass sum total (before constraint)			8 × 8 n = 147	8 × 8 n = 243	8 × 8 n = 245	2 × 2 n = 106

TABLE 1: DEFLECTION COEFFICIENT r_q OF SIMPLY SUPPORTED SQUARE PLATE UNDER UNIFORM LOAD q

$$r_q = \Phi_{max} E h^3 / q s^4, \text{ taking } \alpha = 0.8, v = 0.3$$

h/s	Thin plate theoretic solution	UH	literature 4	literature 3
0.0001	0.01160	0.01141		
0.01	0.01160	0.01142		0.01170
0.05	0.01160	0.01169	0.01182	0.01219
0.10	0.01160	0.01247	0.01255	0.01353
0.15	0.01160	0.01370	0.01469	0.01551
0.20	0.01160	0.01533	0.01542	0.01801
0.25	0.01160	0.01734	0.01755	0.02101

TABLE 2: DEFLECTION COEFFICIENT r_p of SIMPLY SUPPORTED SQUARE PLATE UNDER CENTRAL CONCENTRATED LOAD P . $r_p = W_{max}D/P_s^2$, taking $a=0.6$, $v=0.3$, D is the bending stiffness.

1/4 plate mesh size	4 sides simply supported		4 sides fixed		note
	r_q distrib- uted load	r_p concen- trated load	r_q distrib- uted load	r_p concen- trated load	
1x1	0.02981	0.00819			
2x2	0.04126	0.01033	0.001234	0.004091	
4x4	0.04382	0.01121	0.001355	0.005131	$r_q = \frac{W_{max} Eh^3}{qs^4}$
6x6	0.04422	0.01142	0.001373	0.005380	
Thin plate classic solution	0.04437	0.01160	0.001376	0.0056	$r_p = \frac{W_{max} D}{ps^2}$

TABLE 3: CONVERGENCE OF THE CENTER DEFLECTION OF SQUARE PLATE WITH MESH REFINEMENT (UH:a=0.6, h/s=0.01, v=0.3)

1/4 plate mesh size	Center point bending moment coefficient M_x	Angle point torsion moment coefficient M_{xy}	note
1x1	0.0384	0.034	
2x2	0.0462	0.054	
4x4	0.0477	0.064	
6x6	0.0479	0.065	$m_x = \frac{M_{xmax}}{qs^2}$
Thin plate classic solution	0.0479	0.065	$m_{xy} = \frac{2M_{xymax}}{qs^2}$

TABLE 4: MOMENT COEFFICIENTS OF SIMPLY SUPPORTED SQUARE PLATE UNDER UNIFORM LOAD q (UH:h/s=0.0001, v=0.3)

References:

- (1) Zienkiewicz, O. C. and Hinton, E. "Reduced integration, function Smoothing and non-conformity in finite element analysis", J Franklin Inst, 302, 443-61, 1976.
- (2) Hu Haichang, Tan Xing Li Xue De Bian Fen Yuan Li Ji Qi Ying Yong, Ke Xue Chu Ban She, 1981. "Hu Haichang, Variation Principles of Elastic Mechanics and Other Applications, Science Publishing Co. 1981."
- (3) Pryor, C. W. et al., "Finite element bending analysis of Reissner plates", J Eng. Mech. Div, ASCE, 96, 907-920, 1970.
- (4) Rao, G. V. et al., "A high precision triangular plate bending element for the analysis of thick plates" Nac Eng. Des, 30, 408-412, 1974.
- (5) Wempner, G. A. et al., "Finite element analysis of thin shells", Proc. ASCE, Vol. 94, EM6, 1968.
- (6) Zienkiewicz, O. C. et al., "Reduced integration techniques in general analysis of plates and shells", znt. J. Num. Meth. Eng, Vol. 3, 275-290, 1971.
- (7) Cook, R. D., "Two hybrid elements for analysis of thick, thin and Sandwich plates", znt. J. Num. Meth Eng, Vol. 5, 277-288, 1972.
- (8) Cook, R. D., "Some elements for analysis of plate bending", J. Eng. Mech. Div, ASCE, 98, 1453-1470, 1972.
- (9) Cook, R. D. and dadkaay, S. G., "Observations regarding assumed-stress hybrid plate elements", Znt. J. Num. Meth. Eng, Vol. 8, 513-518, 1974.
- (10) Wu Changchun, Li San Ti Xi De' Hun He Bian Fen YuanLi Ji You Xian Yuan Hun He Mo Shi, Li Xue Xue Bao, 1981 Te Kan. "Wu Changchun, Hybrid Variation Principles of Discrete Systems and Limited Element Hybrid Models, Mechanics Journal, 1981 Special Publication".
- (11) Pian, T. H. H., "On hybrid and mixed finite element methods", Report at the finite element invitational Symposium, Hefei, China, 1981.
- (12) Salerno, V. L. and Goldberg, M. A., "Effect of shear deformation on the bending of rectangular plates", J. Appl. Mech, Vol. 27, 1960.

A LOCAL STRAIN FATIGUE ANALYSIS METHOD AND COMPUTER PROGRAM

Wu Yisheng, Institute of Mechanics, Chinese Academy of Sciences

Abstract:

A local strain fatigue analysis method is presented for evaluation of fatigue life. First, the three parameter elements of load increment, strain increment and stress increment are constructed by using the cyclic stress-strain curve of the material and the cyclic load notched strain curve of notched specimens. Then, the local stress-strain analysis of notched specimens under complex load is made by means of these elements and "availability coefficient matrix" given by R. M. Wetzel. The damage of each cycle is determined on the basis of local strain amplitude and correction for the effect of mean stress. Last, the damage can be cumulated according to Miner's linear cumulative damage theory and the life can be evaluated.

The features of this method consist in adoption of three parameter elements of load increment, stress increment and strain increment; one-step transformation from loadtime histories to local stress and strain-time histories, then the computation procedure is simplified.

The example of the Cumulative Fatigue Damage Division of the SAE Fatigue Design and Evaluation Committee has been computed with our program. The crack formation lives of the notched specimens for two materials under vehicle transmission load have been evaluated and the results are quite consistent with W. R. Brose's results and experiments. This demonstrates that the presented method and program are simple, reliable and rapid. This program can work more than 50 peaks per second and may be available for engineering evaluation of the crack formation life.

I. FORWARD

Structure fatigue damage analysis and life estimated computations are always a problem that many departments of industry pay close attention to. Traditional life estimated computations have adopted nominal stress methods. If the life is computed according to the nominal stress-time histories that the component receives and the S-N curve of the component is obtained through fatigue tests, it is generally necessary to pay a very large price. This kind of method for

life estimated computations cannot correctly reflect the damage process of the stress cumulative position; therefore it is not accurate enough.

The even more accurate life estimated computation method that is presently used is the total life of the component divided into crack formation and crack formation expanding into two phases. Crack formation phases are indicated by the appearance of macroscopic, evident cracks. As to the length of the engineered cracks, this is at present still not clearly defined; based on experience this can be determined as 2mm. The life of the phase of crack expansion can use the method of break-crack mechanics based on material of crack expansion characteristics to be determined; crack formation life can be determined based on local stress and strain analysis and strain fatigue material of the stress concentrated position. This text only touches upon crack formation life computations. In the construction of excelling material and referring to secure life designs, crack formation phases are extremely important.

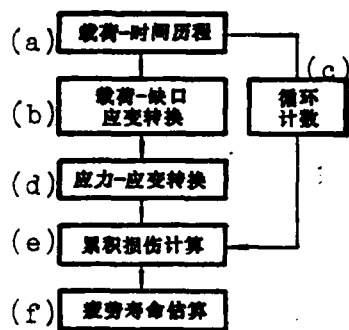
Local strain fatigue analysis method has been developed by foreigners in the last ten some years, has already begun to correspond to departments of the aeronautics industry, and has already broadened to the automotive industry and other industry departments^①. This text introduces this kind of method and its computer programs.

II. METHOD OF LOCAL STRAIN FATIGUE ANALYSIS

The first step of this method of analysis (also the key step) is the transformation of load-time histories received by the component to local stress-strain time histories of the stress accumulation position. Later again based on the size of local stress-strain to compute damage, the life can be evaluated. The major advantage of this method is: we only need to grasp the fatigue test data of the material, then we can forecast the life of each type of component under various load history effects. Additionally, we can compute damage according to the sequence of added load. In this way then, we consider the

inside with the mutual effects between loads. Therefore it is comparatively precise. Under the conditions of stress concentration position with model deformation and cyclic added load, due to the main linearity of the material in itself, the material hardens or softens under cyclic load increments, and the mutual effects between loads are equal factors, causing local stress-strain analysis to become very complex. The principle says that using the model flow theory, the method that uses limited elements can carry out cyclic load increment analysis. But at this moment its operation weight is too large, when exceeding the cycle a few times, in reality there is already no way to carry it out. Therefore we must look for a suitable simple method. Based on large amounts of experimental research, present local strain fatigue analysis uses some sample assumptions that follow:

1. Using a cyclic stress-strain curve to make the material's basic stress-strain relationship. Because the hard or soft phase of the cycle of the material in the fatigue cycle process only constitute a very small proportion after going through a determined cycle, the material then becomes stable. Therefore we can use a cyclic stress-strain curve to represent the interrelation of stress size value and strain size value.
2. Cyclic stress-strain hysteresis loop and cyclic stress-strain curve conditions are similar. The former multiply by the latter.
3. Load cycle and local stress-strain cycles correspond one by one. If the load completes a cycle, the local stress-strain also completes a cycle. Therefore we can construct a cyclic load-strain curve, and this curve represents the relation of load size value and local strain size value.
4. The material possesses memory. If after the stress-strain leaves the original means to complete a cycle, it still returns to the original means.



KEY: (a) Load-time history; (b) Load-notched strain transformation; (c) Cycle count; (d) Stress-strain transformation; (e) Accumulated damage computation; (f) Fatigue life estimated computations.

FIG. 1: THE STEPS OF
LOCAL STRAIN FATIGUE
ANALYSIS

5. Under the conditions of stress concentration position in local model deformation, because the model deformation area is surrounded by the surrounding elastic deformation area, therefore is similarly placed in strain control conditions and we can control the strain fatigue experimental data to carry out damage analysis. Regarding the basic principles of stress-strain analysis, please refer to literature (2).

General steps of local strain analysis are shown in Fig. 1⁽³⁾. Firstly, utilizing cycle load-strain curve with the load-time histories received by the component to transform into notched strain-time histories, and again, utilizing the cyclic stress-strain curve with notched strain-time histories to transform into notched stress-time histories. In the transformation process we use the rainflow counting method to differentiate cycles, and we use the strain-life curve to compute damage. Later according to Miner's linear cumulative damage theory to cumulate damage, the life can be estimated.

In this text we integrate considerations with the cyclic load-strain curve and the cyclic stress-strain curve, constructing the

•When the notch is in single axis stress condition (For example a thin plate notch specimen) it can directly cause a smooth specimen determined cyclic stress-strain curve; when the notch is in tri-axis stress condition (For example thick plate notch specimen), it can cause limited element computed cyclic notch stress-strain curve.

three dimensional cyclic load-stress-strain curve. In the later computation sequence, we use the three parameter element of load-strain- stress increments one step transformation from load-time histories to local stress-strain time histories. From this step of simplified local stress-strain analysis, it shortens the time of analysis and computation.

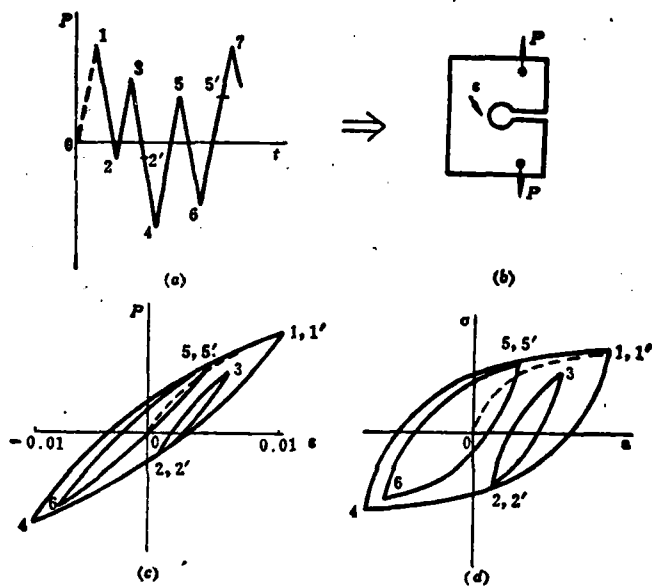


FIG. 2: LOCAL STRESS-STRAIN ANALYSIS FOR CYCLIC LOADING

Now using Fig. 2 as an example to show the process of local stress-strain analysis, and at the same time show how to utilize the above-made assumptions. Establishing Fig. 2(b) to show notch specimen receiving Fig. 2(a) to show the effect of load-time histories. In order to conduct local stress-strain analysis, firstly we must go through experiments to determine cyclic stress-strain curve of the material, as the dotted line in Fig. 2(d) shows, and go through experimental or limited element computation to determine the cyclic load-strain curve, as the dotted line in Fig. 2(c) shows. The corresponding hysteresis loop uses multiple principles to be determined. Analysis from the load peak value point 1 begins, and using cyclic load-strain curve determination and the largest peak value load cor-

responding notched strain, if point 1 in Fig. 2(c) assumes the specimen is very thin, the notch similarly is in single axis stress condition, therefore we can directly use the cyclic stress-strain curve determination and the notched stress corresponding notched strain, thus point 1 in Fig. 2(d). Loading from point 1 removing to point 2, the notch strain and stress separately follow the hysteresis loop transformation that sets out from point 1 to point 2 (the point 2 of Fig. 2(c) and 2(d)). Loading from point 2 adding to point 3, notch strain and stress follow the hysteresis loop that sets out from point 2 transforming to point 3 (the point 3 of Fig. 2(c) and 2(d)). Loading from point 3 removing to 2', at this moment loading completes a cycle, notch strain and stress follow the hysteresis loop that sets out from point 3 to point 2' (the 2' of Fig. 2(c) and 2(d)). At this moment stress and strain also complete a cycle. When continually removing loads from point 2', due to the memory of the material, strain and stress break and return to the hysteresis loop transformation that sets out from point 1, goes directly to point 4, and the later process analogizes. In the figure using 2' and 5' to express the points both are points where loading and stress-strain complete a cycle. In local stress-strain analysis of cyclic loading, correctly determining the completion of stress-strain cycle, and correctly selecting the memory of stress-strain means to reflect the material, both are extremely important.

III. WORKING OUT AND COMPUTING EXAMPLES OF COMPUTATION TECHNIQUE AND COMPUTATION SEQUENCE

The analysis of local stress and strain is very complex. The transformation from load-time histories to local stress and strain-time histories must be conducted on an electronic computer. In order to evaluate linear problems with non-linear problems we can divide a certain amount of elements with the cyclic load-strain curve and the cyclic stress-strain curve; for now each element is represented by a straight line. In order to effectively utilize these units to compute stress and strain transformation, and correctly reflect the material's memory and differentiate the completion of the cycle, the specified useable coefficient that composes each element, we adopt the effective coefficient matrix that Wetzel established⁽⁴⁾. This

text introduces how attached load increments on each element stress-strain increment establish three parameter elements of load strain-stress, and utilize these elements with load transformation to compute transformation of strain-stress. The following simply explains this method of computation and the steps of computation.

1. Intake source data

(1) Load-time histories. Load-time histories use the sequence delivery of peak value and valley value. In order to obtain completed closed load and stress-strain cycles, the best piece of each cycle is from the biggest load beginning to the biggest load end, or is from the smallest load beginning to the smallest load end.

(2) Cyclic load-strain curve. This curve generally can be expressed by the following functional equation:

$$\epsilon_a = \frac{p_a}{c_1} + \left(\frac{p_a}{c_2} \right)^{1/d} \quad (1)$$

Here c_1 , c_2 , and d are the curve drafting together the constant; p_a and ϵ_a separately are cycle size value and strain size value. With c_1 , c_2 , and d three constants are delivered.

(3) Cycle stress-strain curve. This curve generally can be expressed with the following functional equation:

$$\epsilon_a = \frac{\sigma_a}{E} + \left(\frac{\sigma_a}{k'} \right)^{n'} \quad (2)$$

Here E is elastic model weight; k' is cycle intensity constant; σ_a is stress size value. With E , k' , and n' the three constants are delivered.

(4) Strain-life curve. This curve can generally be expressed by the following functional equation:

$$\epsilon_a = \frac{\sigma'_1}{E} (2N_a)^b + \epsilon'_1 (2N_a)^c \quad (3)$$

Where N_f is the violated cycle number; $\sigma_{f,i}$, b , $e_{f,i}$, and c separately are called fatigue intensity coefficient, fatigue intensity index, and fatigue ductility index. They all are constants related to the material quality. It is accumulated by these four parameters.

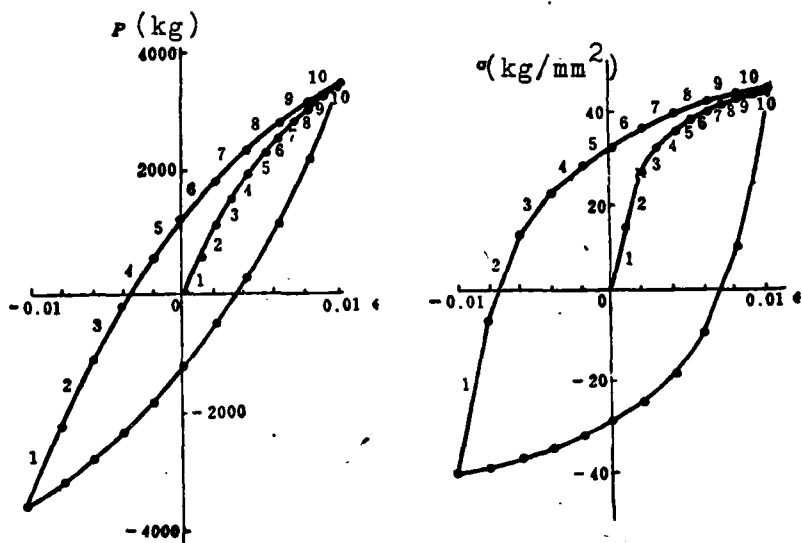


FIG. 3: CYCLIC LOAD-STRAIN CURVE, CYCLIC STRESS-STRAIN CURVE AND RESPECTIVE HYSTERESIS LOOP REPRESENTED BY TEN ELEMENTS

2. Establish the three parameter element of load-strain increment-stress increment. By the computations of formula (1) and the related notch strain of the highest peak value load, taking these strain increment values as the largest strain values, by the cyclic load-strain curve and cyclic stress-strain curve are divided into strain increments equal to the certain amount of elements. Based on formula (1) and formula (2) using alternate solutions to find the load and stress numeric value that corresponds with each point strain, this text adopts the Newton alternative method, using the given load, strain, and stress increments that each element represents. The hysteresis loop also respectively divides into the same kind of numbered elements, and the increment multiple that each element represents is obtained. Figure 3 expresses the cyclic load-strain curve, the cyclic stress-strain curve, and the respective hysteresis loop represented

by ten elements.

3. Establish an effective coefficient matrix, compute the transformation of stress and strain. According to the following rules determine the available coefficient of each element:

(1) If we begin from the largest peak value, then not all the element available coefficients in the beginning uniformly take +1, otherwise they take -1.

(2) The available coefficients of removing load time elements by +1 change to -1, with the computed load descending. When removing load we only can use the elements where the original available coefficients are +1 ; and the elements where the original available coefficients are -1 are "unavailable elements".

(3) The available coefficients of added load time elements by -1 change to +1, with the computed load rising. When adding load we can only use the elements where the original available coefficients are -1; the elements where the original available coefficients are +1 are "unavailable elements".

(4) The elements are each used once and the symbols change once.

(5) Regardless of added load or removed load, always start utilization from the first element.

In the computation process, whenever the condition of unavailable elements is met with, then expressing load and stress and strain completes a cycle. The emergence of unavailable elements becomes the key to using the effective coefficient method to distinguish stress-strain cycles. It raises the identical effect with the rainflow counting method.

4. Compute damage. The damage that each stress-strain cycle creates can be computed according to the following formulas:

$$1/N_i = 2 (\epsilon'_i / \epsilon_{pe})^{1/\alpha} \quad \epsilon_{pe} > \epsilon_{ee} \quad (4)$$

$$1/N_i = 2 \left(\frac{\sigma'_i - \sigma_e}{\sigma_e} \right)^{1/\beta} \quad \epsilon_{ee} > \epsilon_{pe} \quad (5)$$

In the above formulas σ_a is stress size value; σ_0 is average stress; while ϵ_{ee} and ϵ_{pe} separately are elastic strain and model strain. They can be computed according to the following formulas:

$$\epsilon_{ee} = \sigma_a / E \quad (6)$$

$$\epsilon_{pe} = (\sigma_a / k')^{1/\alpha'} \quad (7)$$

5. Accumulate damage. If a phase of load-time histories include n stress-strain cycles, then total damage can be accumulated according to Miner's linear accumulative damage theory:

$$DAMSUM = \sum_{i=1}^n 1/N_i \quad (8)$$

Here $1/N_i$ is damage that the i stress-strain cycle has created. If this phase of load-time histories is repeatedly exerted on the specimen, then the violated number is:

$$BTI = 1/DAMSUM \quad (9)$$

The appendix of this text gives the entire text of the procedure that is drawn up using Fortran language (omitted here). This procedure is the improved form on the basis of literature [3]. What is major is adopting the three parameter element of load-stress-strain increments, simplify the steps of computation, and increase the automatic dividing procedure of the element, greatly reducing machine operation time. To use this computation procedure refer to the examples given in literature [5]. Figure 2 shows the load-time histories that the notched specimen receives constituted of 1709 peak value load. The largest loads separately are 7265, 3633, and 1592 kg.

Specimens were manufactured of copper by the trademarks Man-Ten and RQC-100. Table 2 and Fig. 4 and 5 we can see that the results of this computation and the results of computations in literature [3] are perfectly close. Moreover they coincide with experimental results. Table 3 gives computation time. Using the procedure drawn up in the text, on the average it can compute 50 peak values per second. The level of foreign reports is computing 30 peak values per second [6].

Parameters Materials	E	k'	n'	σ_f'	b	ϵ_f'	c	c_1	c_2	d
Man-Ten	20750	90.07	0.15	109.07	-0.11	1.0	-0.61	639576	30255	0.39
RQC-100	20750	146.37	0.14	140.74	-0.094	1.0	-0.75	639576	29711	0.31

TABLE 1: THE RELEVANT PARAMETERS OF SPECIMENS AND MATERIALS
 E , k' , σ_f' unit: kg/mm^2 ; c_1 , c_2 unit: kg.

Largest Comparison load (kg)	Violated Number	Computer re- sults (this text)	Computer re- sults (3)	Experimental results (5)
7265	6.4 12.5 12.8	16.3	15.2	
3633	420.0 154.0 74.0	182.8	156.3	
1592	2755.0 4270.0 5800.0	4688.2	5000.0	

TABLE 2a: THE COMPARISON BETWEEN COMPUTER RESULTS AND TEST RESULTS OF MAN-TEN NOTCHED SPECIMENS

Largest load (kg.)	Comparison			Violated Number Experimental results (5)
	Computer re-sults (this text)	Computer re-sults (3)		
7265	11.3	5.8		29.0 23.5 22.2
3633	197.6	141.9		269.0 460.0 374.0
1593	94017.3	80448.9		57090.0 88020.0 88020.0

TABLE 2b: THE COMPARISON BETWEEN COMPUTER RESULTS AND TEST RESULTS OF RQC-100 NOTCHED SPECIMEN

Translation	Linked Translation	Operation	Sum Total
13.30	6.81	14.09	34.20

TABLE 3: TIMES TAKEN FOR COMPUTING 1709 PEAKS

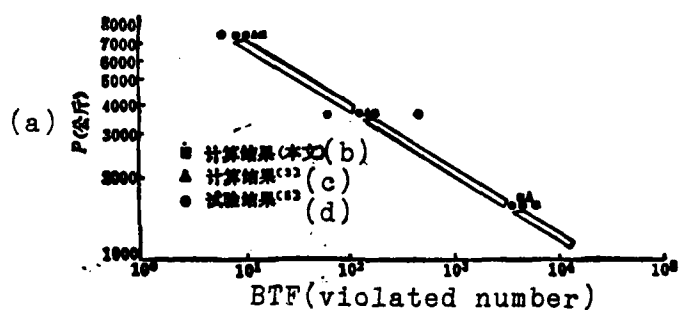


FIG. 4: THE COMPARISON BETWEEN COMPUTER RESULTS AND TEST RESULTS OF MAN-TEN NOTCHED SPECIMENS

KEY: (a) kg; (b) Computer results (this text);
(c) Computer results (3); (d) Experimental results (5).

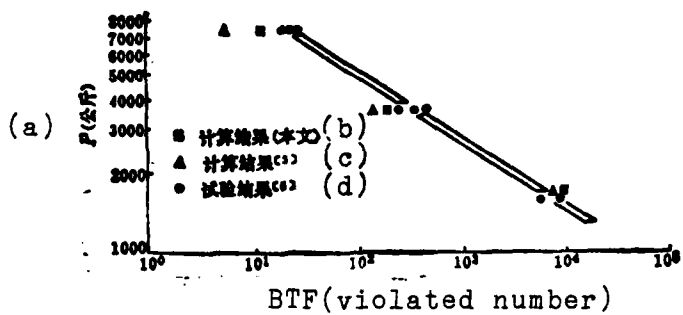


FIG. 5: THE COMPARISON BETWEEN COMPUTER RESULTS AND TEST RESULTS OF RQC-100 NOTCHED SPECIMENS

KEY: (a) kg; (b) Computer results (this text); (c) Computer results (3); (d) Experimental results (5).

IV. CONCLUDING REMARKS

1. The computer results make clear, the life that the computer obtains, using the local strain fatigue analysis method and experimental results are comparatively close. Using this method to compute the life we only must basically test the data of the material, and therefore it is more advantageous than the nominal stress method.

2. The local strain fatigue analysis can conveniently compute accomplishments on the machine. The procedure drawn up in this text adopts the three parameter element of load increment-strain increment-stress increment. Computation is rapid, simple, dependable, and can be used to estimate computations of notched specimen crack formation life.

References:

- (1) R. M. Wetszel, Editor "Fatigue Under Complex Loading, Analyses and Experiments" Advances in Engineering, Vol 6, S. A. E. 1977.
- (2) N. E. Dowling, W. R. Brose, and W. K. Wilson "Notched Member Fatigue life Predictions by the Local strain Approach" S. A. E. Vol 6 P55-64.
- (3) W. R. Brose "Fatigue life Predictions for a Notched Plate With Analysis of Mean Stress and Overstrain Effects" S. A. E. Vol 6 P117-138.

- (1) R. M. Wetzel "A Method of Fatigue Damage Analysis" Pho Thesis, Dept of Civil Eagrg, Univ of waterloo, ontario, Canada 1971.
- (5) L. Tucker "The SAE Cumulative Fatigue Damage Test program" S. A. E. Vo 16 P1-53.
- (6) D. V. Nelson and H. O. Fuchs "Predictions of cumulative Fatigue Damage Using Condensed Load Histories" S. A. E. Vo 16 P175.

SHOCK WAVE BOUNDARY LAYER INTERACTION IN COMPRESSOR CASCADES

Yu Shen, Institute of Engineering Thermophysics, Chinese Academy of Science

Abstract:

Shock wave boundary layer interaction in compressor cascades is an extremely complicated problem. In case of the existence of the separation, it is one of the most important factors which determine the performances of transonic compressor.

However, no thorough investigation has been made on shock wave boundary layer interaction in compressor cascades and only a few papers on this topic have been published.

It is shown by calculation and analysis that the main form of the interaction in compressor cascades is the interaction between shock wave and turbulent boundary layer in channels.

The analysis has made clear that the separation criterion proposed by Pearcey is an empirical criterion obtained from wind tunnel tests of a RAE102 airfoil. The conditions are quite different from the restrained channel flow in compressor cascades with strong adverse pressure gradient. As for compressor cascades, the boundary layer grows rapidly and separates at lower Mach number upstream of the shock wave. the length of separated region and the location of vortex sheet are all different from those in the case of Pearcey's single airfoil. The conclusion has been drawn that it is inappropriate to apply Pearcey's separation criterion directly to shock wave boundary layer interaction in compressor cascades.

It is proposed that the separation criterion for shock wave boundary layer interaction in compressor cascades be in the form $f(M_1, p_1/p_{L.E.}, p_{r.e.}/p_1, Re_c) = 0$, which involves the effects of pressure gradients in front of and behind the shock wave.

I. INTRODUCTION

Shock wave boundary layer interaction rising separation is one of the major factors influencing transonic compressor performance. Shock wave boundary layer interaction in compressor cascades is an extremely complicated problem, however, up until now there still has been no deep research carried out on it, and very few papers have been published. Moreover, it is simple, that among them some viewpoints are not comprehensive. Therefore, we very much need to carry out systematic and deep research on this very important topic.

II. THE FORM IN CASCADE SHOCK WAVE BOUNDARY LAYER INTERACTION

Shock wave boundary layer interaction has many kinds of forms. Straight shockwaves or slanted shockwaves, laminar boundary layers or turbulent boundary layers, different wall surface forms, flow restraints or not, shock wave strength or weakness, boundary layer separation or not; Under the above different conditions, the forms of shock wave boundary layer interaction all are different. Mainstream intensity is different conditions of high supersonic speed and low supersonic speed. The same is low supersonic speed, and the forms of interaction of the M number less than 1.4 and greater than 1.4 can also be different⁽¹⁾. Therefore there are many kinds of forms of shock wave boundary layer interaction. For thirty some years research work on shock wave boundary layer interaction has been carried out as fully as possible, but it still appears very insufficient and scattered.

As to compression cascades we can say, shock wave outcome is either with laminar boundary layer interaction or with turbulent boundary layer interaction: this is the first problem we must resolve. The two have great differences⁽²⁾.

On the surface of the cascade blade, the boundary layer is at the outset laminar ; after going through a distance it turns into turbulent boundary layer. The length of this laminar area can be

long or short, depending on Reynolds number Re and the degree of turbulence of the flow Tu . But from the front blade origin all have laminar flow area. If the entrance orifice of the force one compressor (If there is a front fan, then it is the force one fan) the degree of turbulence generally is not large, and possibly as small as 1% or 0.5%⁽³⁾; the force one rear motor is 2%; the rear forces are 5~6%⁽⁴⁾, even reaching approximately 10%. This all is data under not stalled conditions. Here Tu is referring to $\sqrt{u'^2}/v$, v is average flow velocity; u' is velocity fluctuation value of average airflow direction.

Schlichting⁽⁵⁾ points out that in view of the Reynolds number Re_c the blade hypotenuse is approximately 10^5 to 10^6 ; under high altitude conditions Re_c is smaller. The author chose some parameters to test compute Re_c . The results that were obtained are listed in Table 1. They are approximately 3×10^5 to 3×10^6 , similar to Schlichting's results.

What Klock⁽³⁾ researched was the position of the transition point under conditions of low speed and small Reynolds number. When the degree of turbulence is low, from the blade front edge rising directly to 50% hypotenuse close by within this length all is laminar boundary layers, as seen in Fig. 1.

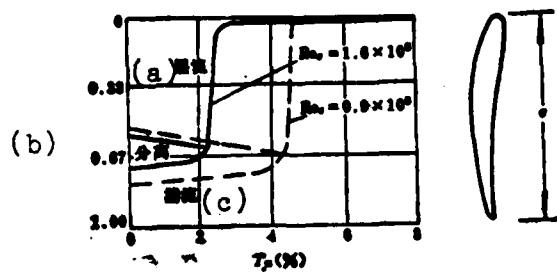


FIG. 1: EFFECT OF Re_c AND Tu
ON THE TRANSITION POINT
KEY: (a) Laminar flow; (b)
Separation; (c) Turbulent flow

Flight Altitude H (m)	Flight M Number	Airflow condition at Compressor entrance orifice					Blade entrance point corresponding flow speed W(m/sec)	blade length c (mm)	Reynolds number $Re_c \times 10^{-5}$
		Axial M Number	Density p_1 kg/m ³	Temper-ature T1(K)	Viscosity $\mu \times 10^5$ kg/m·sec	Sonic speed a m/sec			
0	0	0.4	1.132	280	1.76	335	435	60	16.8
11000	0.85	0.6	0.429	232	1.53	305	397	120	13.3
11000	2.2	0.6	1.662	398	2.27	400	520	80	30.5
20000	2.2	0.6	0.403	398	2.27	400	520	80	7.4
30000	3.0	0.6	0.194	566	2.95	478	622	80	3.3

TABLE 1: THE ACTUAL RANGE OF Re_c

The density of the compressor cascade along the radial changes, the cascade tip density of different compressors also is different, generally speaking transonic speed compressor cascade tip density is constantly between 1.05 and 1.35, also the density of some supersonic compressors is greater than the above scope. As to the commonly used dual circular arc, multiple circular arc, advanced compression, and other forms of cascades, based on the selected density, cascade blade installed angle, the facing angle, and the M number flow, we can approximately determine the position of the shock wave shooting to the blade; this generally is the back half of the blade. Therefore, the shock wave boundary layer interaction in the cascade is generally the interaction of the shock wave and the turbulent boundary layers.

III. SEPARATION CRITERIA OF SHOCK WAVE BOUNDARY LAYER INTERACTION

When shock wave intensity reaches a certain degree, it can then lead to boundary layer separation.

On flat plates when the M number of straight shock waves reach 1.3, it then can lead to turbulent boundary layer separation⁽⁶⁾. As to convex surfaces, bending frequency is exceedingly large, separation area is exceedingly long, and lower pressure is exceedingly small.

Pearcey⁽⁷⁾ established experiential separation criteria: Boundary layer separation occurs on the wing model when the forward shock wave M number is 1.27 (Note: this is not the free-flow M number. The research Pearcey conducted on the model was when the free-flow M number was less than 1, airflow on the wing surface accelerated to supersonic speed.), or there is separation when the rising static pressure of the shock wave rises to reach p_s/p_1 is 1.4. Here p_1 is the static pressure of the forward shock wave; p_s is the static pressure separation point; realistically it indicates the static pressure when there is separation influence. To conduct

computations according to the static pressure when there is sonic speed, see Fig. 2⁽⁷⁾.

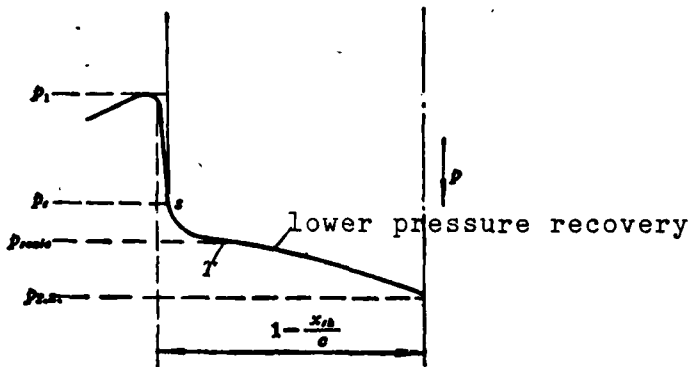


FIG. 2: SURFACE PRESSURE DISTRIBUTION BEFORE AND BEHIND THE SEPARATION POINT

Up till now, because we still have not established the separation criteria in the cascade under shock wave boundary layer interaction, some literature^(8,9) takes the Pearcey separation criteria and directly applies it on the cascade, but because the Pearcey criteria are the experiential criteria that the tests obtained that were conducted on the element wing of the RAE 102 wing model at the thickness ratio being 10%, the coming flow was at high subsonic speed, the angle of attack was 2°, acceleration on the wing surface reached supersonic speed, and passed through quasi-straight shock waves reducing to subsonic speed. Pearcey conducted tests under different forward wave M numbers. To sum it up, distribution occurred when p_s/p_1 was 1.4. This is not precise enough. In reality the p_s/p_1 test point of many numbers is close to 1.5. Because transonic speed cascade appropriately moves under working conditions of both possible separation and possible non-separation, therefore we should look for more precise separation criteria.

We still should point out that Pearcey's element wing test under high subsonic speed and the conditions of supersonic speed cascade are very different. The front edge of the supersonic speed cascade has shock waves, the entrance orifice of various cascade models are different, the degree of airflow expansion is different, the J model cascade back and front sections are even and straight, the S model cascade first goes through a phase of compression, therefore the development of the groove forward shock wave boundary layer and Pearcey's element wing condition are very different.

The author considers that we especially should point out that in the cascade, airflow receives constraints, flows inside the groove, the counter pressure gradient increases, and therefore boundary layer increases to a faster velocity, and separation can then be produced under smaller forward shock wave M numbers; when there is separation the shock wave forks at the place close by the sonic speed area. The length and vortex of the separated region are different from Pearcey's constrained motion of the element wing.

Therefore the author considers that we cannot directly apply Pearcey's separation criteria to compressor aircraft cascades.

The author proposes, as to compressor cascade flow, we should use the separation criteria of the included interaction forward shock wave pressure gradient (we also can use boundary layer thickness) and shock wave pressure gradient. Its functional relationship should be $f(M_1, p_1/p_{L.E.}, p_{T.E.}/p_2, Re_c) = 0$ (This $p_{L.E.}$, $p_{T.E.}$, and p_2 separately are the front edge, the rear edge, and the static pressure of the rear shock wave). Because the forward shock wave M_1 is the primary parameter of resolving shock wave strength and weakness, it naturally should be one of the parameters of separation criteria. The cascade back and front sections have many kinds of different forms, the compression level to the airflow is different, and this has a fairly large influence on the boundary layer increasing velocity and separation. Therefore separation criteria should

include $(p_1 - p_{L.E.})$ or adopt its immeasurable outline form $(p_1 - p_{L.E.})/p_1$, thus $1 - (p_{L.E.}/p_1)$; also we can use the interacting forward boundary layer thickness as a parameter. The tests of Mateer and others⁽¹⁰⁾ clearly indicate that between the separation region length and the interacting forward boundary layer thickness there is a direct ratio relationship, but calibrating the boundary layer thickness is not as convenient as calibrating pressure, and therefore we still use $p_{L.E.}/p_1$ as a parameter.

The major effect of separation to pneumatic performance is causing damage to increase. From the practical viewpoint we come to see that what is serious still does not lie in completely not producing separation, but lies in avoiding producing comparatively large separation areas, so as not to let damage markedly increase. From this point of view we can see that because the major separation of compressor cascade in the groove is turbulence separation, rear shock wave subsonic expands pressure, counter pressure gradient is comparatively large, and has a very large influence on the separation area. Therefore we can also take the counter pressure gradient of the rear shock wave as one of the parameters of separation criteria, using its immeasurable outline form $(p_{T.E.}/p_2) - 1$. According to the test results of Chapman and others⁽¹¹⁾, as to turbulent separation we can say, the influence of the Re number to the beginning separation point is not great, but the Re number has fairly great influence on the length of the separation area⁽¹⁾. These the foregoing are the major parameters of separation criteria.

Because the interaction of shock wave boundary layers is perfectly complicated, we still cannot completely go through theoretical analysis to obtain concrete separation criteria. But conducting tests in a supersonic speed cascade wind tunnel, and analysis, we can obtain half experiential, comparatively precise separation criteria.

IV. CONCLUSION

Shock wave boundary layer interaction in compressor cascades is an extremely complicated problem. Under conditions of rising separation it is one of the major factors of resolving transonic pressure performance.

The author has gone through simple computations and analysis to clearly show the main interaction form of cascades is groove shock wave and turbulent boundary layer interaction.

The author carried out analysis of Pearcey's separation criteria. Because in cascades, boundary layers increase to a faster velocity, under the M number of smaller forward shock waves we thus can have separation. The development of forward shock wave boundary layer, separation area increase, and vortex position also are different from Pearcey's element wing conditions. Therefore, the author considers that it is not suitable to directly apply Pearcey's separation criteria to compressor cascades.

Through analysis, the author proposed to use separation criteria on shock wave boundary layer interaction in compressor cascades that includes forward shock wave pressure gradient, rear shock wave pressure gradient, and also include in the criteria M_1 and Re numbers. The form is $f(M_1, p_1/p_{L.E.}, p_{T.E.}/p_2, Re_c) = 0$. We can conduct tests and analysis in a supersonic speed cascade wind tunnel to obtain concrete separation criteria for shock wave boundary layer interaction in compressor cascades.

Reference Literature

- [1] Vidal, R.J., Wittiff, C.E., Catlin, P.A. and Sheen, B.H., Reynolds number effects on the shock wave-turbulent boundary layer interaction at transonic speeds. AIAA paper 73-661 (1973) p. 7 and p. 1.
- [2] Liepmann, H.W., Roshko, A. and Dhawan, S., On reflection of shock wave from boundary layers. NACA Report 1190 (1951) p. 28.

- [3] Klock, R., Influence of the degree of turbulence on the aerodynamic coefficients of cascades. Published in: AGARD-AG-184. (1972) p. 77-88.
- [4] deHaller, P., DasVerhalten von Tragflügelgittern in Axial-vrdichtern und im Windkanal. VDI-Bericht Bd. 3 (1958) p. 27-31.
- [5] Schlichting, H., Recent progress in boundary-layer research. AIAA Journal Vol. 12, No. 4. (1974) p. 427.
- [6] Fage, A. and Sargent, R.F., Shock wave and boundary layer phenomena near a flat plate surface. Proc. Royal Soc. (London) Ser. A Vol. 190 №. 1020 (1947) p. 1-10.
- [7] Pearcey, H. H. Some effects of shock-induced separation of turbulent boundary layers in transonic flow past airfoils. A.R.C.R. and M. №. 3108. p. 28 and p. 34 (1959).
- [8] Chauvin, J., Sieverding, C. and Griepeartog, H. Cascade flow in transonic regime. Published in: Dzeng, L. S., Flow research on blading. Amsterdam: Elsevier Publishing Company. (1970) p. 183.
- [9] Criepeartog, H. Shock wave boundary layer interaction in cascades. Published in: ACARD-AG-184. (1972) p. 445.
- [10] Mateer, G. G., Brosh, A., Viegas, J. R., A normal shock wave turbulent boundary layer interaction at transonic speeds. AIAA paper 76-161 (1976) p. 1.
- [11] Chapman, D. R., Kuska, D. M., and Larson, H. K., Investigation of separated flows in supersonic and subsonic streams with emphasis on the effect of transition. NACA Report №. 1386 (1958) p. 34.

EXPERIMENTAL STUDY ON DISCHARGE AND LOSS COEFFICIENTS OF COMBUSTOR SWIRLERS

Zhang Chunxia, Wuxi Aircraft Engine Research Institute
Wang Yulian, Shenyang Liming Machinery Company

Abstract:

The blade-type swirlers have been used in many air engine combustors to control the primary airflow of flame tube and establish a strong recirculation zone. The losses produced by the swirler depend on stagger angle, pitch/chord ratio and passage area of blades.

Some test results of the swirlers with different stagger angles, numbers of blades and flow areas are presented. A set of discharge characteristics and relations between loss coefficient and swirl number, stagger angle or blade number are provided. In addition, the correlation of loss coefficient to discharge coefficient of blade-type swirlers has been established. It is found out that the discharge coefficient varies from 0.6 to 0.9 for swirlers with different stagger angles. The correlation $\psi = 31.0(1.53s - 1)$ indicates that the selection of swirl number must retain the loss coefficient at an acceptable level (aerodynamically).

It can be seen from the test results that the blade loss is evidently smaller than the secondary expansion loss for a given combustor swirler. The value of the blade loss is about 18 percent of the total loss for a straight blade swirler with stagger angle varying from 68° to 70°.

The tests have also proved that the twisted blade swirler is superior to the straight one from the aerodynamic point of view. But its manufacture is more complicated. Therefore, the straight blade swirlers (with stagger angle $\geq 45^\circ$) have been used in a large number of combustors.

I. TEST PREPARATIONS

Scheme of the test facility is shown in Fig. 1.
Calibrated air discharge of the test facility is 0.06~0.14 kg/seconds.
Mach number of swirlers entrance orifice $M=0.03\sim 0.14$.

Inside the polymethyl methacrylate tube the diameter of the

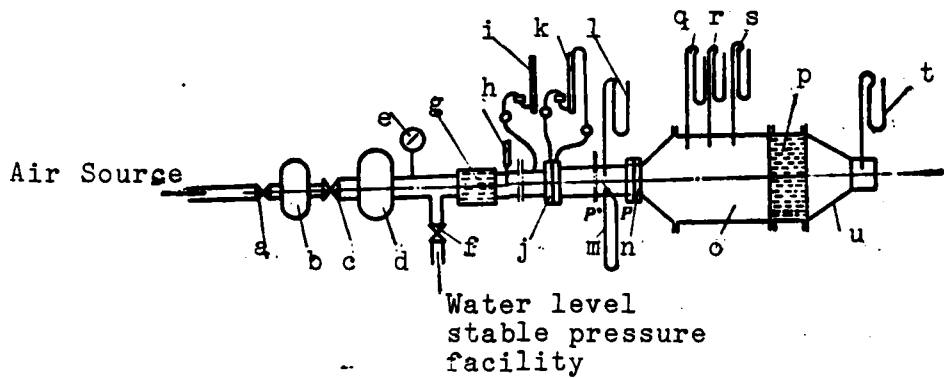


FIG. 1: SCHEME OF THE TEST FACILITY

KEY: (a) Voltage valve; (b) Air-liquid separator; (c) Voltage valve; (d) Air desiccator; (e) Pressure table; (f) Valve; (g) Rectifier; (h) Mercury thermometer; (i) Opening plate forward pressure gauge; (j) Opening plate; (k) Differential pressure gauge; (l) Entrance orifice total pressure gauge; (m) Entrance orifice moving pressure head gauge; (n) Swirler test specimen; (o) Polymethyl methacrylate tube; (p) Rectifier; (q, r, s) Swirler exhaust orifice static pressure gauge; (t) Exhaust orifice total pressure gauge; (u) Exhaust orifice convergence section.

installed swirlers is ϕ 235mm, taking the size of the observance recirculation zone and the variations of its edge axial.

In front of the opening plate flow meter and behind the swirler (In front of the exit orifice pressure calibration section) devices are installed that have many openings rectification to eliminate tone, utilizing the U form tube to calibrate each pneumatic parameter.

To eliminate system errors, the system total pressure damage that is measured when there are no swirlers follows the variable value of the entrance orifice airflow parameters, in order to finally compute when arranging the loss coefficients of the swirlers.

When experimenting, air temperature is within 20-30° C.

II. CONSTRUCTING COEFFICIENTS OF TESTED SWIRLERS

The main experimental specimen is the straight blade swirler. For the purpose of comparison, experiments were also conducted on the twisted blade swirler of the combustion chamber of certain types of engines. Its minute details of construction and dimensions are seen in Table 1 and Fig. 2 and 3. In the Table each dimension uniformly is a realistic measurement value.

To conveniently compare the swirl intensity, the table yet lists the swirl number S of each swirler. The ratio of the angular momentum and the axial momentum of the swirler coefficient exhaust orifice airflow and the effective diameter product of the swirler is computed according to the following formula:

$$S = \frac{2}{3} \left[\frac{1 - (R_n/R)^2}{1 - (R_n/R)^4} \right] \operatorname{tg} \beta \quad (1)$$

Where

R_n is ring radius inside the swirler;

R is ring radius outside the swirler;

β is staggered angle of the blade.

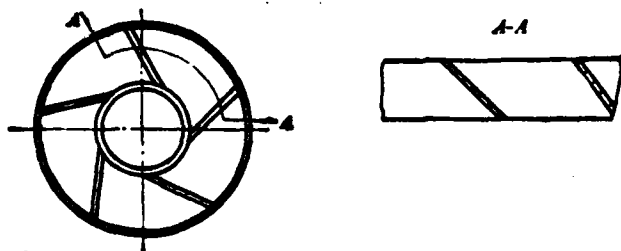


FIG. 2: STRAIGHT BLADE SWIRLER

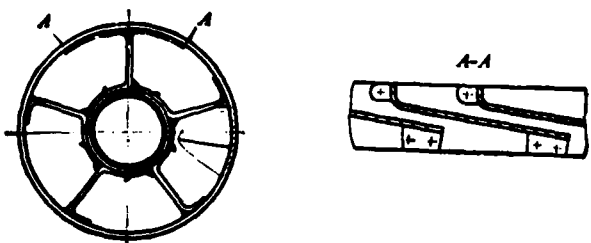


FIG. 3: TWISTED BLADE SWIRLER

TABLE 1 CONSTRUCTION FACTORS OF TESTED SWIRLERS

Parameter Number	Blade Staggered Angle β	Blade Number n	Blade thickness mm	Swirler outside diameter mm Ds	Swirler inside diameter mm d	Swirler Exhaust Orifice Cross-section mm ² Fs	Swirler number S
A-1	67° 46'	5	1.15	70.0	40.0	8.9374	1.9698
A-2	67° 09'	5	1.15	70.0	40.0	9.1964	1.9108
A2-1	69° 35'	6	1.15	70.0	40.0	8.0033	2.1632
A2-2	68° 2'	6	1.15	70.0	40.0	8.6561	1.9962
A3-1	69° 5'	9	1.15	70.0	40.0	7.6956	2.1068
A3-2	68° 41'	9	1.15	70.0	40.0	7.8666	2.0635
B-1	48° 36'	9	1.15	70.0	40.25	13.6985	0.9133
B-2	46° 56'	9	1.20	70.0	40.25	13.6233	0.8615
B2-1	52° 1'	10	1.20	70.0	40.30	14.0542	1.0312
B2-2	49° 24'	10	1.30	70.0	40.30	14.8139	0.9394
B3-1	52° 13'	12	1.20	70.0	39.90	13.7514	1.0387
B3-2	50° 21'	12	1.30	70.0	39.90	14.5002	0.9715
C2-1	57° 45'	6	1.20	70.0	39.90	12.7799	1.2762
C2-2	57° 30'	6	1.20	70.0	40.25	12.8886	1.2639
C3-1	59° 9'	9	1.20	70.0	40.30	11.7167	1.3481
C3-2	58° 26'	9	1.20	70.0	39.30	11.9757	1.3105
811	79° 0'	5	1.20	71.0	30.0	4.30	2.1800

● Twisted blade swirler

● Blade staggered angle is average value.

III. TEST METHODS

1. Determination of Swirler Discharge Coefficient μ_s

a. According to calibrated parameter computations opening plate discharge is G_k .

b. According to discharge continuity, $G_k = G_s$ (G_s is air discharge going through swirler), seeking the swirler discharge coefficient μ_s .

2. Determination of Loss Coefficient ↓

According to

$$\psi_1 = \Delta P^* / (P_1^* - p_1) \quad (2)$$

Where

ψ_1 is corresponding to the airflow loss coefficient of the swirlor intake orifice.

ΔP^* is the total pressure damage going through the swirlor.

$P_1^* - p_1$ is the swirlor intake orifice moving pressure head.

The loss coefficient corresponding to the swirlor exhaust orifice cross section:

$$\psi_s = \psi_1 (F_s / F_1)^2 \quad (3)$$

Where

F_s is swirlor exhaust orifice cross section area;

F_1 is swirlor intake orifice flow tube cross section area.

In order to obtain the swirlor loss coefficient of the non-quadratic expanded damage (thus blade damage coefficient), we still adopt the following test programs:

The swirlor exhaust orifice directly opens wide into the atmosphere, calibrates the sum pressure of the exhaust orifice passage-way among each blade of the swirlor following all along the circumference and all along the diameter, and lastly takes its arithmetic mean to compute the loss coefficient.

IV. TEST RESULTS AND DISCUSSION

Test results are shown in Fig. 4 through Fig. 9.

1. Discharge Coefficient of the Swirlor

The tests clearly show that the primary discharge coefficient

of the swirler is related to the constructed model that was adopted and the blade stagger angle.

(1) Comparing the test results of twisted blade swirlers and other straight blade swirlers, we can know that the average blade stagger angle of the one most fully forward reaches 79° , but many straight blade swirlers where its discharge coefficient is even smaller than the stagger angle are all large. Estimating this is due to using back twisted blade, its upper area side edge is parallel to the airflow; the airflow angle of attack is zero; thus we obtain the low of the straight blade swirler where the damage is greater than the angle of attack.

(2) The same constructed model swirler discharge main coefficient is related to the stagger angle of the blade. Under the conditions of this test, the approximate range is:

- a. as to $45^\circ < \beta < 50^\circ$, $\mu_s = 0.80 \sim 0.90$;
- b. as to $50^\circ < \beta < 60^\circ$, $\mu_s = 0.65 \sim 0.75$;
- c. as to $60^\circ < \beta < 70^\circ$, $\mu_s = 0.60 \sim 0.70$.

As to the twisted blade swirler of $\beta = 79^\circ$, $\mu_s = 0.74 \sim 0.84$.

(3) The discharge coefficient follows the increase and reduction through the swirler airflow pressure decline. Within the range of the pressure decline of the tests in this text assume a linear relationship. But the discharge coefficient reduces very slowly, in similar computations we can assume each kind of swirler discharge coefficient is a constant.

2. Characteristics of Swirler Discharge

As in Fig. 5, each characteristic line corresponds to a β and n value. Refer to the figure.

Model coordinates $\bar{G} = G, \sqrt{T}/F, P$

Where G_s is air discharge of each second through the swirler (kg/seconds);

T_1^* is the sum temperature of the swirler intake orifice (K);

P_1^* is the sum pressure of the swirler intake orifice (kg/cm^2);

F_s is the circulation area of the swirler (cm^2).

Longitudinal coordinates are $\bar{x} = (P_1^* - P_2)/P_1^*$

Where p_2 is the static pressure of the swirler exhaust orifice.

The checking computations of the flow circuit parameters in the combustion chamber can apply to this formula curve, by \bar{G} check \bar{p} , to obtain p_{20} .

3. Loss Coefficient of Swirler

(1) The damage of the swirler is composed of the two parts which are the quadratic expanded damage and the blade damage. According to the test results in literature (1), when β value is within $65^\circ \sim 85^\circ$, the blade damage of the straight blade swirler approximately holds 23% of the total damage. Making $\bar{\psi} = \psi/\psi_t$. (ψ is the blade damage coefficient, ψ_t is the total damage coefficient), the tests made clear:

a. Blade stagger angle is bigger, $\bar{\psi}$ is bigger, moreover we can take 60° as the dividing line, after $\beta < 60^\circ$, $\bar{\psi}$ unobviously increases;

b. The $\bar{\psi}$ value distance of the twisted blade is smaller than that of the straight blade;

c. As to the straight blade swirler,

When $\beta = 68^\circ \sim 70^\circ$, $\bar{\psi}_{\text{uniform}} = 0.18$

When $\beta = 50^\circ \sim 60^\circ$, $\bar{\psi}_{\text{uniform}} = 0.08$.

Because the total pressure calibration error of the blade passage exhaust orifice is fairly large, and moreover the total pressure distribution in the straight blade exhaust orifice is not as uniform as that of the twisted blade exhaust orifice, therefore test results only are approximate values.

(2) The relationship between the swirler loss coefficient and the blade stagger angle, blade number, and swirl number.

a. With blade stagger angle increase and blade number increase, the swirler loss coefficient increases:

$$\psi_1 = 16.5(0.75 \sec^2 \beta - 1) \quad (\beta = 45^\circ \sim 70^\circ) \quad (4)$$

b. Swirl number S is an important parameter when the swirler is designed. For the combustion chamber of an aircraft motor it is necessary to make $S > 0.6$, then we can establish a stable combustory recirculation region. But with the increase of S, the swirler efficiency drastically reduces, therefore the two must be given consideration. Based on the test results, this text establishes the formula for the relationship between the swirler number and the loss coefficient:

$$\psi_1 = 3.10(1.53S - 1) \quad (5)$$

4. The Relationship Between Swirler Discharge Coefficient and Loss Coefficient

Through linking each test swirler discharge coefficient and loss coefficient, we obtain the curve that Fig. 9 expresses, and can express it as:

$$\mu_s = \frac{1}{1 + 0.07\sqrt{\psi_1}} \quad (6)$$

As it is convenient to compare, according to the computation of similar hydraulic formula $\mu_s = \frac{1}{1 + \sqrt{\psi_1}}$ the curve is shown in the figure.

V. SUMMARY

The preliminary results that this test obtained are:

1) Swirler discharge coefficients are different than blade type and stagger angle, regarding the straight blade.

$$(1) \mu_s = 0.8 \sim 0.9 \quad (45^\circ < \beta < 50^\circ)$$

$$(2) \mu_s = 0.65 \sim 0.75 \quad (50^\circ < \beta < 60^\circ)$$

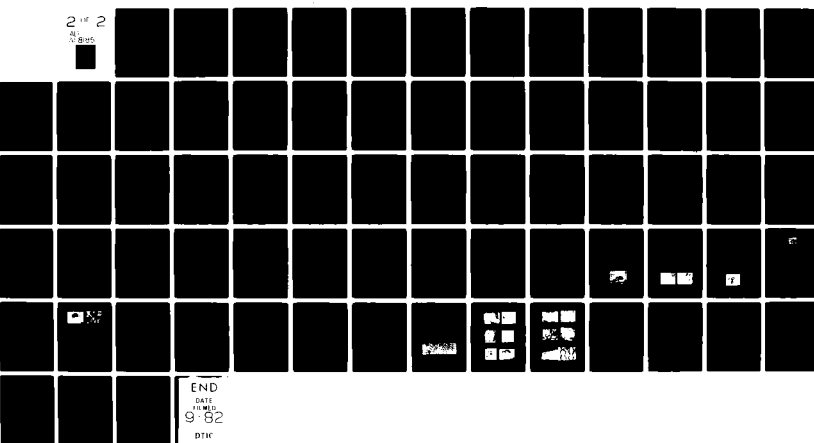
AD-A118 185 FOREIGN TECHNOLOGY DIV WRIGHT-PATTERSON AFB OH
JOURNAL OF AERONAUTICS. (U)

F/6 20/4

JUL 82
UNCLASSIFIED FTD-ID(RS)T-0621-82

NL

2 of 2
NL
B65



END
DATE
FILED
9-82
DTIC

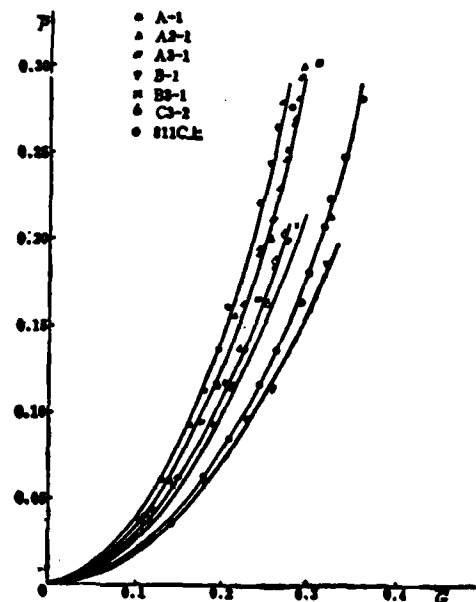


FIG. 4: GENERAL DISCHARGE CHARACTERISTICS OF SWIRLERS

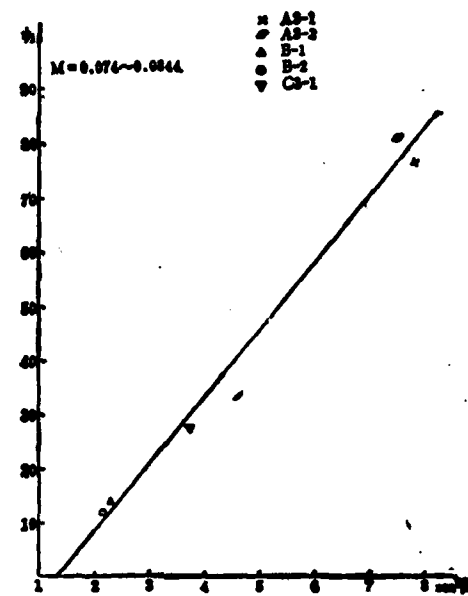


FIG. 5: VARIATION OF LOSS COEFFICIENT WITH STAGGER ANGLE

$$(3) \mu_s = 0.60 \sim 0.70 \quad (60^\circ < \beta < 70^\circ)$$

2) Obtaining a formula that correlates to general discharge characteristics of swirlers of different stagger angles and blade numbers.

3) The proportion of swirler blade damage to total damage is very small. Under conditions of this test, when $\beta = 68^\circ \sim 70^\circ$, $\psi_{uniform} = 0.18$, when $\beta = 50^\circ \sim 60^\circ$, $\psi_{uniform} = 0.08$.

4) Between swirler loss coefficients and blade stagger angle and swirl number the following linking formulas are established:

$$\begin{aligned}\psi_1 &= 16.5(0.75 \sec^2 \beta - 1) \\ \psi_2 &= 31.0(1.53 S - 1)\end{aligned}$$

5) After $\beta \geq 60^\circ$, loss coefficient markedly increases.

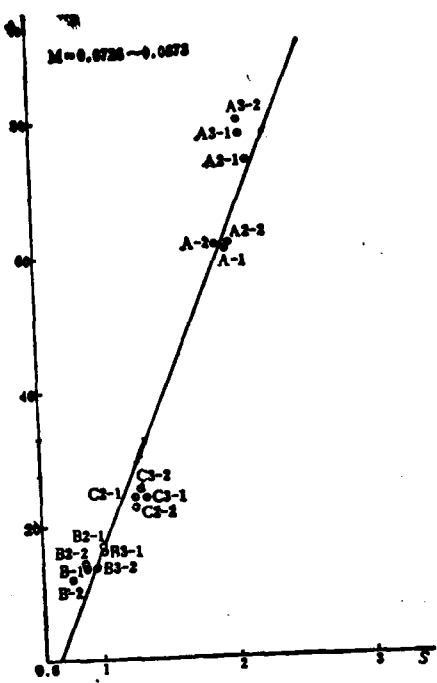


FIG. 6: VARIATION OF LOSS COEFFICIENT WITH SWIRL NUMBER

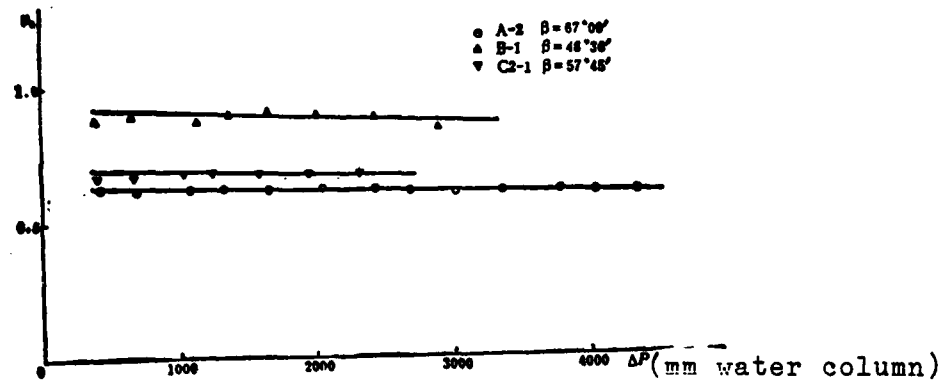


FIG. 7 VARIATION OF DISCHARGE COEFFICIENT WITH PRESSURE DROP

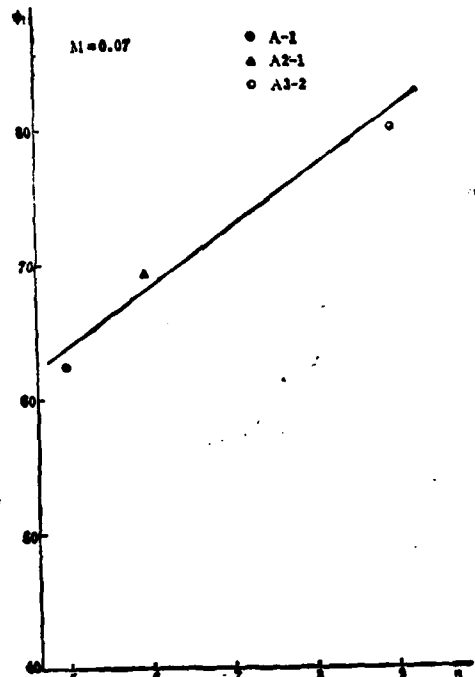


FIG. 8: VARIATION OF LOSS COEFFICIENT WITH BLADE NUMBER

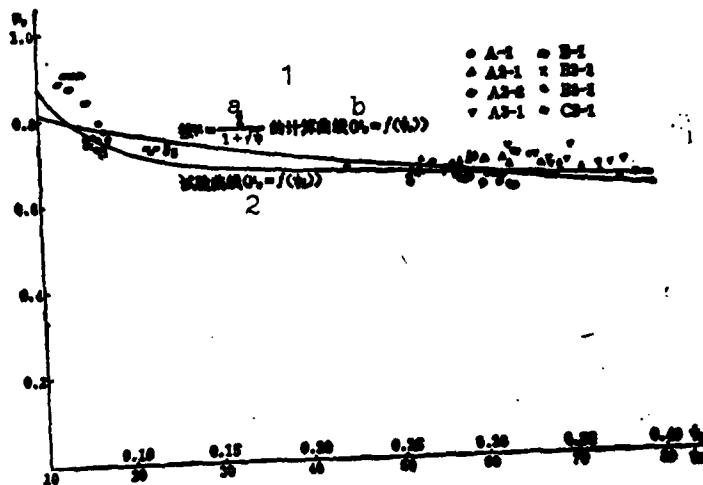


FIG. 9: CORRELATION OF LOSS COEFFICIENT TO DISCHARGE COEFFICIENT
KEY: (1) Computed curve b that is in accordance with a; (2) Test curve

Reference Literature

- (1) H. A. Knight and R. B. Walker "The Component Pressure Losses in Combustion Chambers" A. R. C. T. R. R. & M. No. 2987.
- (2) R. J. Mado and R. Roberts "A pollutant emissions prediction model for gas turbine combustors". AIAA/SAE, 10th Propulsion Conference October 21-23, 1974.
- (3) J. M. Beer and Chigier "Combustion Aerodynamics"
- (4) Huang Zhaoxiang, Hang Kong Rao Qi Wo Lun Pen, Qi Fa Dong Rao Shao Shi, Guo Fang Gong Ye Chu Ban Shi. "Huang Zhaoxiang, Combustion Chamber of an aeronautic Combustion Turbine Jet Engine, Country Defense Industry Publishing Bureau".

ASYMPTOTIC STABILITY OF PARTIALLY DAMPED MECHANICAL SYSTEMS

Gao Weibin, Beijing Institute of Aeronautics and Astronautics

Abstract:

In this paper the asymptotic stability of the partially damped linear mechanical system with gyroscopic forces is studied. The equation of motion for the system is a second order linear matrix differential equation. The stiffness matrix is assumed to be positive definite representing the conservative forces and then Lyapunov's second method is employed. By splitting the system matrices in block matrices the condition of asymptotic stability (e. g. the condition of pervasiveness) can be expressed as a rank condition of certain matrix with dimension lower than that of the system. Several cases with different gyroscopic coupling are discussed. The stability condition is not only simpler than that obtained by former authors, but also gives some insight to the mechanical properties of the system since it may be considered as two coupled subsystems then.

I. INTRODUCTION

The problem of stability of mechanical systems is an age-old problem. In recent years some mechanical system problems have emerged in aeronautic and astronauitic flight instruments and other technologies, again arousing the attention of researchers. For the work in this area we can refer to literature (1~7).

Taking the generalized coordinate vectors of mechanical systems as $x^t = (x_1, \dots, x_n)$, then the equation for the linearized motion differential of mechanical systems:

$$M\ddot{x} + D\dot{x} + Gx + Kx = 0 \quad (1-1)$$

is a second order linear matrix differential equation. In it M expresses inertia matrix, generally a positive definite: $M = M^T > 0$;

D expresses the damping matrix, generally a positive definite:
 $D = D^T \geq 0$; G expresses the gyroscopic force matrix, it is a slanted symmetrical $G = G^T$; K expresses the rigidity matrix, it is a symmetrical matrix: $K = K^T$. Were it not for every generalized damping force not equal to zero just $\det D \neq 0$, then we say the system receives incomplete damping, or the system is called partially damped.

In literature (3) with the classic theorems of Kelvin, Tait, Chetayev together are called the K-T-C theorem: the stability of system (1-1) is equal to the stability of the conservative mechanical system:

$$M\ddot{x} + Kx = 0 \quad (1-2)$$

When $K > 0$ (positive definite) and $D \geq 0$ (semi-positive definite), Zajac points out if at this moment system (1-1) asymptotically stabilizes, then the damper is called "pervasive damped". Literature (4 and 5) carry out research on this condition. To the gyroscopic system:

$$M\ddot{x} + D\dot{x} + Kx = 0 \quad (1-3)$$

in which $M > 0$, $D \geq 0$, $K > 0$, literature (6) gives the criteria for asymptotic stability (thus conditions of pervasive damping):

$$\text{order } \begin{bmatrix} D \\ D(M^{-1}K) \\ \dots \\ D(M^{-1}K)^{n-1} \end{bmatrix} = * \quad (1-4)$$

and literature (7) proves the criteria for asymptotic stability to even more generalized mechanical system (1-1) after changing into a first order system:

$$\text{order } \begin{bmatrix} C \\ CA \\ \dots \\ CA^{n-1} \end{bmatrix} = 2n, \quad A \triangleq \begin{bmatrix} O & I_n \\ -M^{-1}K & -M^{-1}G \end{bmatrix}, \quad C \triangleq [O \ D] \quad (1-5)$$

The results of this text (2-10) and (3-1) are somewhat more simplified than (1-5) and (1-4).

II. CRITERIA FOR ASYMPTOTIC STABILITY

To research mechanical system (1-1), in which $n \times n$ matrix $M > 0$, $K > 0$, and $G = -G^T$, the damping matrix can be expressed as:

$$D = \begin{bmatrix} D_0 & O \\ O & O \end{bmatrix}, \det D_0 \neq 0, D_0 \in \mathbb{R}^{n \times n}, r < n \quad (2-1)$$

With formula (1-1) written into a first order form, we have:

$$\dot{x} = y, \dot{y} = -M^{-1}Dy - M^{-1}Gy - M^{-1}Kx \quad (2-2)$$

drawn into a split matrix that corresponds with (2-1):

$$\begin{aligned} x &= \begin{bmatrix} x_1 \\ x_2 \end{bmatrix}, x_1 \in \mathbb{R}^r, x_2 \in \mathbb{R}^{n-r}, y = \begin{bmatrix} y_1 \\ y_2 \end{bmatrix}, y_1 \in \mathbb{R}^r, y_2 \in \mathbb{R}^{n-r}, \\ M^{-1}D &= \begin{bmatrix} D_1 & O \\ D_2 & O \end{bmatrix}, M^{-1} = \begin{bmatrix} M_1 & M_2 \\ M_2 & M_4 \end{bmatrix}, G = \begin{bmatrix} G_{10} & G_{20} \\ G_{30} & G_{40} \end{bmatrix} \\ M^{-1}G &= \begin{bmatrix} G_1 & G_2 \\ G_3 & G_4 \end{bmatrix}, M^{-1}K = \begin{bmatrix} K_1 & K_2 \\ K_3 & K_4 \end{bmatrix}, K = \begin{bmatrix} K_{10} & K_{20} \\ K_{30} & K_{40} \end{bmatrix} \end{aligned} \quad (2-3)$$

Thus we can resolve with formula (2-2), to obtain two systems:

$$\begin{aligned} \dot{x}_1 &= y_1, \dot{y}_1 = -D_1 y_1 - G_1 y_1 - G_3 y_2 - K_1 x_1 - K_3 x_2 \\ \dot{x}_2 &= y_2, \dot{y}_2 = -D_2 y_1 - G_2 y_1 - G_4 y_2 - K_2 x_1 - K_4 x_2 \end{aligned} \quad (2-4)$$

Constructing Lyapunov's function to system (2-2):

$$v = \frac{1}{2} y^T M y + \frac{1}{2} x^T K x$$

It clearly is a positive definite, seeking the derivative of the solution of the v edge (2-2), we obtain:

$$\dot{v} = -y^T D y = -y_1^T D_1 y_1 \quad (2-5)$$

It is only a semi-negative definite. In order to prove that (2-2) or (2-4) asymptotically stabilize and seek the criteria for asymptotic stabilization, we use La Sall's theorem⁽⁹⁾. For this reason it requires satisfaction of:

$$v \equiv 0 \text{ if } D_0 y_1 \equiv 0 \quad (2-6)$$

the solution of formula (2-4) only has balanced conditions, $x_1 = 0$, $x_2 = 0$, $y_1 = 0$, $y_2 = 0$. Condition (2-6) gives out: $y_1 = 0$ this way formula (2-4) becomes:

$$\begin{aligned} y_1 &= 0, \quad x_1 = A, \quad G_1 y_1 + K_1 x_1 = -K_1 A \\ \dot{x}_1 &= y_1, \quad \dot{y}_1 = -G_1 y_1 - K_1 A - K_1 x_1 \end{aligned} \quad (2-7)$$

In which A is a constant vector-product constant. Formula (2-7) can also be expressed as:

$$(K_1 \quad G_1) \begin{bmatrix} x_1 \\ y_1 \end{bmatrix} = -K_1 A \quad (2-8a)$$

$$\begin{bmatrix} \dot{x}_1 \\ \dot{y}_1 \end{bmatrix} = \begin{bmatrix} 0 & I \\ -K_1 & -G_1 \end{bmatrix} \begin{bmatrix} x_1 \\ y_1 \end{bmatrix} - \begin{bmatrix} 0 \\ K_1 \end{bmatrix} A = L \begin{bmatrix} x_1 \\ y_1 \end{bmatrix} - I \quad (2-8b)$$

$$L \Delta \begin{bmatrix} 0 & I \\ -K_1 & -G_1 \end{bmatrix}, \quad I = \begin{bmatrix} 0 \\ K_1 \end{bmatrix} A \quad (2-8c)$$

With formula (2-8a) we seek a derivative towards t to obtain:

$$(K_1 \quad G_1) \begin{bmatrix} \dot{x}_1 \\ \dot{y}_1 \end{bmatrix} = 0 \quad (2-9a)$$

Substituting formula (2-8b) we have:

$$(K_1 \quad G_1) L \begin{bmatrix} x_1 \\ y_1 \end{bmatrix} = (K_1 \quad G_1) I$$

Again seeking a derivative towards t to obtain:

$$(K_1 G_1) L \begin{bmatrix} \dot{x}_1 \\ \dot{y}_1 \end{bmatrix} = 0 \quad (2-9b)$$

Continuing down, we obtain:

$$(K_k G_k) L^k \begin{bmatrix} \dot{x}_1 \\ \dot{y}_1 \end{bmatrix} = 0, \quad k = 0, 1, 2, \dots \quad (2-9c)$$

Matrix L is $2(n-r) \times 2(n-r)$ dimensional. According to the Hamilton-Cayley theorem⁽¹⁰⁾, the least $L^{2(n-r)}$ will be the linear combination $I, \dots, L^{2(n-r)-1}$. One of the reasons is in formula (2-9c) the most has $2(n-r)$ that are independent. When:

$$\text{order } S = 2(n-r), \quad S \triangleq \begin{bmatrix} (K_1 G_1) \\ (K_1 G_1) L \\ \dots \\ (K_1 G_1) L^{2(n-r)-1} \end{bmatrix}. \quad (2-10)$$

formula (2-9) only has zero solution: $\dot{x}_2 = 0, \dot{y}_2 = 0$, if

$$y_2 = 0, \quad x_2 = B \quad (2-11)$$

In which B also is a constant vector. At this time equation (2-7) becomes:

$$K_1 A + K_2 B = 0, \quad K_3 A + K_4 B = 0$$

Because the coefficient matrix of the above equation if K satisfies the order, one of the reasons is $A=0, B=0$. This precisely shows the system only has zero solutions under the condition of (2-10), thereby proving formula (2-10) is the pervasive condition of the asymptotic stability of the system.

Now we prove that condition (2-10) is also necessary. We established the asymptotic stability of the system, but formula (2-10) is not established. At this time, the necessary existing vector C* satisfies:

$$C^* \in \text{Ker } S, \quad C^* \neq 0 \quad (2-12)$$

If C^* satisfies:

$$(K_1 G_1) L^k C^* = 0, \quad k = 0, 1, 2, \dots \quad (2-13)$$

the solution of the differential equation (2-7) possesses the form:

$$\begin{bmatrix} x_1 \\ y_1 \end{bmatrix} = \exp(Lt) C + L^{-1} I \quad (2-14)$$

Because L satisfies the order, L^{-1} exists. According to literature (11) there is

$$\exp(Lt) = \sum_{k=0}^{2(n-r)-1} a_k(t) L^k$$

In which $a_k(t)$ is the function of t . With $a_k(t)$ multiplied (2-13) all formulas later mutually increase, to obtain:

$$(K_1 G_1) \sum a_k(t) L^k C^* = (K_1 G_1) \exp(Lt) C^* = 0 \quad (2-15)$$

Taking integral constant $C=C^*$, substitute formula (2-15) with formula (2-14) thus to obtain:

$$(K_1 G_1) \begin{bmatrix} x_1 \\ y_1 \end{bmatrix} = (K_1 G_1) L^{-1} I$$

Again substitute form (2-8a) with (2-8c) and consider that:

$$L^{-1} = \begin{bmatrix} -K_4^{-1} G_4 & -K_4^{-1} \\ I & 0 \end{bmatrix}$$

We can derive:

$$K_1 A = G_2 K_4^{-1} K_3 A$$

Because K_1 satisfies the order, and the right end is not equal to $K_1 A$, consequently we inevitably have:

$$A = 0, \quad I = 0, \quad (2-16)$$

$$\begin{bmatrix} x_1 \\ y_1 \end{bmatrix} = \exp(Lt) C^*, \quad \begin{bmatrix} x_1 \\ y_1 \end{bmatrix} = 0$$

This clearly shows under condition (2-6), formula (2-7) or (2-8) has no zero solution (2-16), and is contradictory with the assumption, it is necessary to obtain proof.

The asymptotic stability fully required condition of the partially damped system. Assume the system:

$$M\ddot{x} + D\dot{x} + Gx + Kx = 0$$

Where $M > 0$, $-G = G^T$, $K > 0$, $D = \begin{pmatrix} D_0 & 0 \\ 0 & 0 \end{pmatrix}$, $D_0 > 0$, the order of the $r \times r$ matrix D_0 is equal to r , its balanced state asymptotic stability fully required condition is (2-10):

$$\text{order } S = 2(n-r)$$

Note 1. Matrix S generally has $2(n-r)$ arrangement and in literature 7 matrix (1-6) has $2n$ arrangement. The determination of the order obtains simplification, this particularly is notable when r approaches near n .

Note 2. Matrix S is the split matrix expression of each coefficient matrix through system (1-1), one of the reasons is that it is easy to analyze the influence of each matrix block on the stability.

Note 3. On direct observation, adding the fully damped D_0 of the system that is expressed by x_1 , inevitably brings about $x_1(t) \rightarrow 0$, and only when condition (2-10) is established, if when a certain gyroscopic coupling and rigid coupling exist, then can it cause x_2 to also have asymptotic stability. Condition (2-10) also is precisely a pervasive damped condition.

Note 4. The selection through the coordinate system causes M to become the diagonal matrix, and will cause simplification of determination.

III. PARTIALLY DAMPED GYROSCOPIC SYSTEMS AND NON-GYROSCOPIC SYSTEMS

1. Non-gyroscopic systems, the condition of $G=0$. At this moment

the system equation is:

$$M\ddot{x} + D\dot{x} + Kx = 0 \quad (1-3)$$

Considering that $G=0$, condition (2-10) can be simplified by:

$$L = \begin{bmatrix} 0 & I \\ -K_4 & 0 \end{bmatrix}, \quad S = \begin{bmatrix} (K_1, 0) \\ (0, K_2) \\ -(K_2, K_3, 0) \\ -(0, K_3, K_4) \\ \dots \end{bmatrix} = \begin{bmatrix} S_1 & 0 \\ 0 & S_2 \\ \vdots & \vdots \\ 0 & S_n \end{bmatrix}, \quad S_0 \triangleq \begin{bmatrix} K_1 \\ K_2 K_4 \\ K_2 K_3 \\ \dots \\ K_2 K_4^{n-1} \end{bmatrix}$$

In which certain positive-negative numbers are omitted (this does not influence the determination of order), to obtain equivalent condition:

$$\text{order } S_0 = n - r \quad (3)$$

Note 1. Condition (3-1) has comparatively greater simplification than condition (1-4) in literature [6]. This is similar to the situation in the second section.

Note 2. We still can directly derive condition (3-1) from condition (1-4). By formula (2-1) and (2-3), remember:

$$D = \begin{bmatrix} D_0 & 0 \\ 0 & 0 \end{bmatrix}, \quad D(M^{-1}K) = \begin{bmatrix} L_1^1 & L_1^2 \\ 0 & 0 \end{bmatrix}, \quad L_1^1 \triangleq D_0 K_1, \quad L_1^2 \triangleq D_0 K_2$$

$$D(M^{-1}K)^2 = \begin{bmatrix} L_1^1 & L_1^2 \\ 0 & 0 \end{bmatrix}, \quad L_1^1 \triangleq L_1^1 K_1 + L_1^2 K_2, \quad L_1^2 \triangleq L_1^1 K_2 + L_1^2 K_3$$

$$\dots$$

$$D(M^{-1}K)^{n-1} = \begin{bmatrix} L_1^{n-1} & L_1^n \\ 0 & 0 \end{bmatrix}, \quad L_1^{n-1} \triangleq L_1^{n-1} K_1 + L_1^n K_2, \quad L_1^n \triangleq L_1^{n-1} K_2 + L_1^n K_3$$

They have the following equal relationship:

$$\begin{aligned}
 \text{Order } S &= \text{order} \begin{bmatrix} D_0 & O \\ O & O \\ \overline{L_1^1 - L_2^1} \\ O & O \\ \vdots \\ \overline{L_1^{n-1} - L_2^{n-1}} \\ O & O \end{bmatrix} = \text{order} \begin{bmatrix} D_0 & O \\ L_1^1 & L_2^1 \\ \dots \\ L_1^{n-1} & L_2^{n-1} \end{bmatrix} = \text{order} \begin{bmatrix} D_0 & O \\ O & L_2^1 \\ \dots \\ O & L_2^{n-1} \end{bmatrix} \\
 &= r + \text{order} \begin{bmatrix} L_2^1 \\ L_2^2 \\ \vdots \\ L_2^{n-1} \end{bmatrix} = r + \text{order} \begin{bmatrix} D_0 K_1 \\ L_2^1 K_2 \\ \vdots \\ L_2^{n-1} K_n \end{bmatrix} = r + \text{order} \begin{bmatrix} D_0 K_1 \\ D_0 K_1 K_2 \\ \vdots \\ D_0 K_1 K_{n-1} \end{bmatrix} = r + \text{order } S_0
 \end{aligned}$$

The 3, 5, and 6 equal formulas of the above formulas go through multiple determinant transformations to be obtained, the most unequal formula transformation is lengthy and the process is omitted. This way it proves: "Order $S=n$ " is equivalent to "Order $S_0=n-r$ ".

Note 3. According to the dissipation we can conduct the following classifications with mechanical systems:

- a. Fully damped, $D>0$; System asymptotic stabilization.
- b. Partially damped, $D>0$:
 - (1) Pervasively damped, order $S_0=n-r$: System asymptotic stabilization.
 - (2) Not pervasively damped, order $S_0< n-r$: System stable but not asymptotically stable.

2. Partially gyroscopic system: $D=\begin{bmatrix} D_0 & O \\ O & O \end{bmatrix}$, $G=\begin{bmatrix} G_0 & O \\ O & O \end{bmatrix}$, the dimension of block matrix G_0 is equivalent to the dimension of D_0 . In this condition, $M^{-1}G=\begin{bmatrix} G_1 & 0 \\ G_3 & 0 \end{bmatrix}$, condition (2-10) also becomes (3-1), G_0 does not produce an effect on the stability. This can be expected, because the system that x_1 expresses is fully damped.

3. Partially gyroscopic system: $G=\begin{bmatrix} 0 & 0 \\ 0 & G_0 \end{bmatrix}$, $M^{-1}G=\begin{bmatrix} 0 & G_2 \\ 0 & G_4 \end{bmatrix}$. In this condition, due to inertia coupling, adding gyroscopic force of the system that x_2 expresses will produce effect on the whole system. It

influences the order of the S matrix, if influencing pervasive damped conditions. But when inertia coupling does not exist, $M_2 = M_3^T = 0$, then condition (2-10) becomes condition (3-1), and proof is omitted.

4. Gyroscopic coupling system: $G = \begin{bmatrix} 0 & G_1 \\ -G_1^T & 0 \end{bmatrix}$, $M^{-1}G = \begin{bmatrix} G_1 & G_2 \\ G_2 & G_3 \end{bmatrix}$.

This moment generally speaking, the coupling of gyroscopic forces greatly influences the pervasiveness of damping, and moreover, even if the inertia force is without coupling, by:

$$\begin{bmatrix} G_1 & G_2 \\ G_2 & G_3 \end{bmatrix} = \begin{bmatrix} M_1^{-1} & 0 \\ 0 & M_3^{-1} \end{bmatrix} \begin{bmatrix} 0 & G_1 \\ -G_1^T & 0 \end{bmatrix} = \begin{bmatrix} 0 & M_1^{-1}G_1 \\ -M_3^{-1}G_1^T & 0 \end{bmatrix}$$

We can obtain:

$$G_1 = 0, \quad G_2 = 0, \quad G_3 = M_1^{-1}G_1, \quad G_1 = -M_3^{-1}G_1^T$$

It is thus evident that G_1 coupling has influence on the pervasiveness of the damping of the system. It can cause partial damping of the system to become pervasive. From this we can make the system asymptotically stable.

IV. EXAMPLES

1. Consider the mechanical system that is shown in Fig. 1.

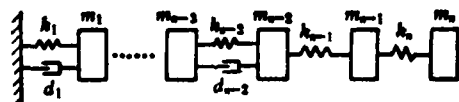


FIG. 1: MECHANICAL SYSTEM WITH PERVERSIVE DAMPING

The equation for the system is:

$$M\ddot{x} + D\dot{x} + Kx = 0$$

$$M = \text{diag}(m_1, \dots, m_n)$$

$$K = \begin{pmatrix} k_1 + k_2 & -k_2 & & O \\ -k_2 & k_2 + k_3 & & \\ & \ddots & k_{n-1} + k_n & -k_n \\ O & & -k_n & k_n \end{pmatrix}, \quad D = \begin{pmatrix} d_1 + d_2 & -d_2 & O & \\ -d_2 & d_2 + d_3 & & \\ & \ddots & -d_{n-2} & \\ O & -d_{n-2} & d_{n-2} & \\ O & & O & O \end{pmatrix}$$

According to the definition, we have:

$$\begin{bmatrix} K_1 & K_2 \\ K_2 & K_4 \end{bmatrix} = M^{-1}K, \quad K_1 = \begin{pmatrix} O & O \\ \vdots & \vdots \\ O & O \\ -\frac{k_{n-2}}{m_{n-2}} & O \end{pmatrix}, \quad K_4 = \begin{pmatrix} \frac{k_{n-1} + k_n}{m_{n-1}} & -\frac{k_n}{m_{n-1}} \\ -\frac{k_n}{m_n} & \frac{k_n}{m_n} \end{pmatrix};$$

Due to:

$$\text{秩 } S_0 = \text{秩} \begin{bmatrix} K_1 \\ K_2 K_4 \\ \vdots \end{bmatrix} = \text{秩} \begin{pmatrix} -\frac{k_{n-2}}{m_{n-2}} & O \\ \times & \frac{k_{n-2} k_n}{m_{n-2} m_{n-1}} \\ \vdots & \vdots \end{pmatrix} = 2$$

We can know the system has asymptotic stability, damping is pervasive, and the conclusive physics phenomenon is obvious.

2. Consider the mechanical system that Fig. 2 shows.

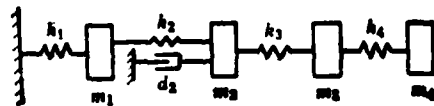


FIG. 2: MECHANICAL SYSTEM WITH NONPERVASIVE DAMPING

The equation for the system is:

$$M\ddot{x} + D\dot{x} + Kx = 0$$

$$M = \text{diag}(m_1, \dots, m_4), \quad K = \begin{pmatrix} k_1 + k_2 & -k_2 & O & O \\ -k_2 & k_2 + k_3 & -k_3 & O \\ O & -k_3 & k_3 + k_4 & -k_4 \\ O & O & -k_4 & k_4 \end{pmatrix}$$

Changing the sequence of coordinates x_1 and x_2 , the coefficient matrix separately becomes:

$$M = \text{diag}(m_1, m_2, m_3, m_4), \quad K = \begin{pmatrix} k_1+k_2 & -k_2 & -k_3 & 0 \\ -k_2 & k_1+k_2 & 0 & 0 \\ -k_3 & 0 & k_3+k_4 & -k_4 \\ 0 & 0 & -k_4 & k_4 \end{pmatrix}$$

$$D = \text{diag}(d_1, 0, 0, 0)$$

Computations are:

$$M^{-1}K = \begin{pmatrix} K_1, K_2 \\ K_3, K_4 \end{pmatrix}, \quad K_4 = \begin{pmatrix} \frac{k_1+k_2}{m_1} & 0 & 0 \\ 0 & \frac{k_3+k_4}{m_3} & -\frac{k_4}{m_3} \\ 0 & -\frac{k_4}{m_4} & \frac{k_4}{m_4} \end{pmatrix}$$

$$K_1 = \left[-\frac{k_1}{m_1} \quad \frac{k_3}{m_2} \quad 0 \right],$$

$$\text{Order So=order } \begin{pmatrix} -\frac{k_2}{m_1} & -\frac{k_3}{m_2} & 0 \\ -\frac{k_1+k_2}{m_1} \frac{k_2}{m_2} & -\frac{k_3}{m_2} \frac{k_1+k_4}{m_3} & \frac{k_3}{m_2} \frac{k_4}{m_3} \\ -\left(\frac{k_1+k_2}{m_1}\right)^2 \frac{k_2}{m_2} & -\frac{k_3}{m_2} \left(\frac{k_3+k_4}{m_3}\right)^2 & \frac{k_3 k_4}{m_2 m_3} \frac{k_3+k_4}{m_3} \\ \vdots & -\frac{k_3 k_4^2}{m_2 m_3 m_4} & +\frac{k_3 k_4^2}{m_2 m_3 m_4} \end{pmatrix}$$

If $k_1=k_2=k_3=k$, $m_1=m_2=m_3=m_4=m$, then S descending order condition is $k=3/2 k_4$. At this moment partial damping is particularly pervasive, and possible motion emerges: m_2 is unmoving, the motion of m_1 with the motion of m_3 and m_4 are reversed resonant motion.

V. CONCLUDING REMARKS

With classic mechanical system differences, there the primary research is on conservative systems, and in modern times in mechanical systems artificial dampers are often recommended and are regarded as the composed means. We recommend dampers of comparatively smaller numbers in order to ensure that the problem of system asymptotic stability has certain reference significance. When analyzing partially damped mechanical systems, with the coefficient matrix of the system

a split block, we can establish an ordered criteria of a lower dimension, and also it is convenient to analyze the mechanical properties of the system.

Reference Literature

- [1] Ziegler H., Linear Elastic Stability, ZAMM, 4, 89-121, 168-185, 1953.
- [2] Debra D. D., Delp R. H., Rigid body stability and Natural Frequencies in Circular Orbit, J. Astronaut. Sci., 8, 14-17, 1961.
- [3] Zajak E. E., The Kelvin-Tait-Chetaev Theorem and Extensions, J. of Aeronaut. Sci., 11, 46-49, 1964.
- [4] Roberson R. E., Notes on the Thompson-Tait-Chetaev Stability Theorem, J. of Astronaut. Sci., 15, 319-322, 1968.
- [5] Conell G. M., Asymptotic Stability of Second-Order Linear Systems with Semidefinite Damping, AIAA J., 7, 1185-1187, 1969.
- [6] Walker J. A., Schmitendorf W. E., A Simple Test for Asymptotic Stability in Partially Dissipative Symmetric Systems, Trans. of ASME, J. of Appl. Mech., 10, 1120-1121, 1973.
- [7] Hughes P. C., Gardner L. T., Asymptotic Stability of Linear Stationary Mechanical Systems, 同上, 12, 1975.
- [8] Fawzy I., A Simplified Stability Criterion for Nonconservative Systems, 同上, 46, 423-426, 1979.
- [9] LaSalle J., Lefschetz S., Stability by Lyapunov's Direct Method, Academic Press, New York, 1961.
- [10] Гант маев Ф. Р., Теория матриц, Гостехиздат, 1954.
- [11] Fortinson T. E., Hitz K. L., An Introduction to Linear Control Systems, Marcel Dekker, 1977.

AERODYNAMIC COEFFICIENT IDENTIFICATION OF TIME-VARYING AIRCRAFT SYSTEM AND ITS APPLICATION

Wang Tong, Beijing Research Institute, China Precision Machinery Corporation

Abstract:

Aerodynamic coefficient identification for time-varying aircraft system has been studied. Usually, the time-varying system identification is quite difficult. On the basis of practical measurement in flight tests and by analyzing trend of the coefficients in aircraft time-varying differential equations, it is possible to transform the individual time-varying coefficient into a known function multiplied by an unknown constant. These unknown constants are referred to as undefined coefficients. With the aid of the Newton-Raphson method extended to the time-varying coefficient differential equations the undefined coefficients can be evaluated by iteration calculation. In this way the complicated time-varying aircraft identification can be carried out.

In order to verify this calculation the aerodynamic coefficients of an aircraft have been evaluated by the data taken from one of its unsteady flight, and the reliability of aerodynamic coefficients obtained from this identification has been discussed. The calculation results matched very well the test data and made a contribution to the improvement of aircraft flight tests.

I. PREFACE

According to the identification theory, using flight test data to compute the aerodynamic coefficient of the flight instrument has a very practical significance. In order to use the identification theory to obtain a more accurate aerodynamic coefficient, except for the problem of computation, we still must provide a series of advantageous conditions: for example the aircraft has suitable motorized motion, causing the flight test data to include sufficient aerodynamic coefficient information; it requires the arrangement of suitable more precise measurement bearing; the aircraft mathematical model is fairly close to realistic conditions. For this reason we can carry out

specialized flight tests, after the aircraft flight stabilizes, the rudder surface carries out movement according to a pre-determined course, the aircraft makes motorized flight, bearing the corresponding data that has been recorded. Under this kind of condition, from the flight test data we compute the aerodynamic coefficient of the aircraft, the motion process of the aircraft generally is a constant coefficient differential equation.

Real flight tests sometimes meet with problems and unstable flight occurs. If the problem does not stem from the pilot apparatus or other components, then it is possible that the original mathematical model of the aircraft is not accurate. The originally determined aerodynamic coefficient and the real aerodynamic coefficient in flight are not in accord. This was objectively then it is necessary to utilize flight test data to compute the aerodynamic coefficient of the aircraft. Clearly at this time the conditions for computation are insufficient, the rudder motion was not specially designed for the purpose of obtaining the aerodynamic coefficient, and there is problem motion. The measured parameter that is advantageous to parameter identification has no certain provision to compute the aerodynamic coefficient, we can only use the existing measured parameters of flight tests, particularly the linking together of frequent problems and acute transformation of parameters. Therefore we cannot take the motion equation of the aircraft and treat it as a constant coefficient differential equation, but should treat it as a variable coefficient differential equation. This text researches parameter identification under this kind of condition.

II. EQUATION FOR VARIABLE COEFFICIENT AIRCRAFT SYSTEM

The following only researches the side motion equation of the aircraft, the side motion compared to the vertical motion is a little more complicated, and the possibility of problems that emerge is sometimes a little more. Additionally, consider that the aircraft is an elastic body, due to elastic vibration of the aircraft, in flight tests the angle degree and angle velocity signal that the telemetering

transducer is affected by, except for including the angle degree and angle velocity signal of aircraft real flights, still includes the rising angle degree and angle velocity information of the aircraft elastic vibration in the transducer.

The equations for aircraft motion are as follows:

$$\begin{aligned}
 \dot{x}_1 &= A_{11}(t)x_1 + A_{12}(t)x_2 + A_{13}(t)x_3 + B_{11}(t)u_1 + B_{12}(t)u_2 \\
 \dot{x}_2 &= A_{21}(t)x_1 + A_{22}(t)x_2 + A_{23}(t)x_3 + B_{21}(t)u_1 + B_{22}(t)u_2 \\
 \dot{x}_3 &= -\frac{\alpha(t)}{57.3}x_1 + x_2 + A_{33}(t)x_3 + A_{34}(t)x_4 \\
 \dot{x}_4 &= x_1 \\
 \dot{x}_5 &= x_2 \\
 \dot{x}_6 &= x_7 \\
 \dot{x}_7 &= -\xi\omega x_6 - \omega^2 x_6 + D_2(t)x_2 + D_3(t)x_3 + D_4(t)u_2 \\
 x_8 &= x_1 + x_7 \\
 x_9 &= x_2 + x_8
 \end{aligned} \tag{1}$$

Where

- x_1 is trundle angle velocity
- x_2 is yaw angle velocity
- x_3 is side slip angle
- x_4 is trundle angle
- x_5 is yaw angle
- x_6 is signal of the elastic vibration of the aircraft on the yaw angle measurement (rudder free gyration)
- x_7 is signal of the elastic vibration of the aircraft on yaw angle velocity measurement (rudder damped gyration)
- x_8 is signal of included aircraft elastic vibration on rudder damped gyration
- x_9 is signal of included aircraft elastic vibration on rudder free gyration
- u_1 is aileron deflector angle
- u_2 is yaw rudder deflection angle
- $A_{11}(t), A_{12}(t), A_{13}(t), A_{21}(t), A_{22}(t), A_{23}(t), A_{33}(t), A_{34}(t)$ are the aerodynamic coefficients of the aircraft
- $B_{11}(t), B_{12}(t), B_{21}(t), B_{22}(t)$ are rudder surface aerodynamic coefficients of the aircraft

ξ is aircraft elastic vibration damping coefficient

ω is aircraft elastic vibration frequency

$a(t)$ is angle of attack

$D_2(t)$, $D_3(t)$, $D_1(t)$ separately are yaw angle velocity, side slip angle, yaw rudder angle regarding the elastic vibration coecion force of the aircraft.

Computing aircraft aerodynamic coefficient from flight test data (if we seek $A_{ij}(t)$, $B_{ij}(t)$, and $D_i(t)$), because these parameters all follow time variations, moreover the amount is fairly much, therefore they are difficult to directly obtain. The following makes suitable transformations to these parameters, with appropriate identification computations.

Coefficients $A_{ij}(t)$, $B_{ij}(t)$, and $D_i(t)$ receive the influence of many factors. If altitude H , flight Mach number M , and aircraft weight G or inertia I that rise due to fuel consumption transform, then we have the expressed formula:

$$A_{ij}(t) = A_{ij}(M(t), H(t), G(t))$$

$$B_{ij}(t) = B_{ij}(M(t), H(t), G(t))$$

$$D_i(t) = D_i(M(t), H(t), G(t))$$

But these factors $M(t)$, $H(t)$, and $G(t)$ in flight tests are comparatively easy to measure or to obtain by computation, and are comparable with real flight aerodynamic coefficients that are difficult to ascertain. The believeable estimate of the value of these factors must be very large, therefore in the process of flight test data that is used to compute the aircraft aerodynamic coefficient, we can extract these already known time varying factors, and the remaining unknown sections, taking undefined coefficient expression, in this way $A_{ij}(t)$, $B_{ij}(t)$, and $D_i(t)$ can be written as $A_{ij}(t) = a_{ij}F_{ij}(t)$, $B_{ij}(t) = b_{ij}G_{ij}(t)$, $D_i(t) = d_iH_i(t)$. In which a_{ij} , b_{ij} , and d_i are undefined coefficients, $F_{ij}(t)$, $G_{ij}(t)$, and $H_i(t)$ are already known time varying functions with computed $A_{11}(t) = a_{11}F_{11}(t)$ as an example to explain this point.

$$A_{11}(t) = \frac{q S_0 D_0^2}{J_x V} m_x^w$$

Where

q is velocity head $q=q(M(t), H(t))$;

v is velocity $V=V(M(t), H(t))$;

S_0 is aircraft's largest cross section;

D_0 is aircraft's largest diameter;

J_x is elastic axis directional rotation inertia $J_x=J_x(t)$;

m_x^w is damping coefficient of the rolling force moment, by theoretical computation or wind tunnel, it follows the regulation of the flight

Mach number M is already known, therefore we have $m_x^w = a_{11} f(M(t))$, a_{11} is an undefined coefficient, $f(M(t))$ is the similar formula of m_x^w following M variable regulation.

Therefore:

$$A_{11}(t) = \frac{q(M(t), H(t)) S_0 D_0^2}{J_x(t) V(M(t), H(t))} a_{11} f(M(t)) = a_{11} F_{11}(t)$$

Using the same kind of method to obtain the rest $A_{ij}(t) = a_{ij} F_{ij}(t)$, $B_{ij}(t) - b_{ij} G_{ij}(t)$, $D_i(t) = d_i H_i(t)$.

Taking the above formulas and substituting equation (1) we thus have:

$$\begin{aligned} \dot{x}_1 &= a_{11} F_{11}(t) x_1 + a_{12} F_{12}(t) x_2 + a_{13} F_{13}(t) x_3 + b_{11} G_{11}(t) u_1 + b_{12} G_{12}(t) u_2 \\ \dot{x}_2 &= a_{21} F_{21}(t) x_1 + a_{22} F_{22}(t) x_2 + a_{23} F_{23}(t) x_3 + b_{21} G_{21}(t) u_1 + b_{22} G_{22}(t) u_2 \\ \dot{x}_3 &= \frac{a(t)}{57.3} x_1 + x_4 + a_{33} F_{33}(t) x_3 + a_{34} F_{34}(t) x_4 \\ \dot{x}_4 &= x_1 \\ \dot{x}_5 &= x_2 \\ \dot{x}_6 &= x_3 \\ \dot{x}_7 &= -\xi \omega x_7 - \omega^2 x_8 + d_1 H_1(t) x_1 + d_2 H_2(t) x_2 + d_3 H_3(t) x_3 + d_4 H_4(t) u_1 \\ x_8 &= x_1 + x_2 \\ x_9 &= x_3 + x_4 \end{aligned} \quad (2)$$

Therefore we compute the aerodynamic coefficient from flight test data and the problem of ξ and ω in a nutshell is to seek the undefined coefficients a_{ij} , b_{ij} , d_i , ξ and ω of the variable coefficient differen-

tial equation (2).

III. COMPUTATION FOR PARAMETER IDENTIFICATION

The above already establishes the mathematical model for the variable coefficient aircraft system. In generalized aircraft tests, through a telemeter we can obtain $u_1 i$, $u_2 i$, x_3^i measured, x_9^i measured, and x_4^i measured (the lower "i" symbol is a time-order of telemetered sampling). The task of parameter identification is simply to take the telemetered rudder yaw $u_1 i$ and $u_2 i$ as input, select suitable aerodynamic coefficients, substitute these aerodynamic coefficients in equation (2), solve the square and as the smallest of the difference of $x_1 i$, $x_8 i$, $x_9 i$, and $x_4 i$ the equation (2) caused to obtain and the corresponding telemetered values x_1^i measured, x_8^i measured, x_9^i measured, and x_4^i measured.

In the mathematical expression, if we establish a function J

$$J = \sum_{i=1}^n [(x_{1i} - x_{1im})^2 + (x_{8i} - x_{8im})^2 + (x_{9i} - x_{9im})^2 + (x_{4i} - x_{4im})^2] \quad (3)$$

take the undefined coefficients a_{ij} , b_{ij} , d_i , ξ , and ω , and compose a vector c.

$$c^T = [a_{11}, a_{12}, a_{13}, b_{11}, b_{12}, a_{21}, a_{22}, a_{23}, b_{21}, b_{22}, a_{31}, a_{32}, \xi, \omega, d_1, d_2, d_3]$$

(T expresses the turning position).

J value is the function of vector c, by J value towards vector c we seek the smallest value to determine vector c.

By using the Newton-Raphson method of iteration formula we can obtain the J value to reach the smallest vector c⁽¹⁾.

$$c_{k+1} = c_k - \left(\sum_{i=1}^n \nabla_c X_i^T \nabla_c X_i \right)^{-1} \left[\sum_{i=1}^n \nabla_c X_i^T (X_i - X_{\text{measured}}) \right] \quad (4)$$

Where X_i is the vector;

$$X_i^T = (x_1 i, x_8 i, x_9 i, x_4 i)$$

$$X_{\text{measured}}^T = (x_{1i}^{\text{measured}}, x_{8i}^{\text{measured}}, x_{9i}^{\text{measured}}, x_{4i}^{\text{measured}})$$

$\nabla_c X_i$ expresses the differential of vector X_i to vector c .

By formula (4) we can know, the iteration computation of vector c can in a nutshell be computed $\nabla_c X_i$. Because the lower symbols that the computations used to be reached are comparatively many, for clear expression, the following computations omit the lower symbol "i".

$\nabla_c X$ uses the matrix expressed as:

$$\nabla_c X = \begin{pmatrix} \frac{\partial x_1}{\partial a_{11}} & \frac{\partial x_1}{\partial a_{12}} & \frac{\partial x_1}{\partial a_{13}} & \frac{\partial x_1}{\partial b_{11}} & \frac{\partial x_1}{\partial b_{12}} & \frac{\partial x_1}{\partial a_{21}} \\ \frac{\partial(x_2+x_7)}{\partial a_{11}} & \frac{\partial(x_2+x_7)}{\partial a_{12}} & \frac{\partial(x_2+x_7)}{\partial a_{13}} & \frac{\partial(x_2+x_7)}{\partial b_{11}} & \frac{\partial(x_2+x_7)}{\partial b_{12}} & \frac{\partial(x_2+x_7)}{\partial a_{21}} \\ \frac{\partial(x_5+x_9)}{\partial a_{11}} & \frac{\partial(x_5+x_9)}{\partial a_{12}} & \frac{\partial(x_5+x_9)}{\partial a_{13}} & \frac{\partial(x_5+x_9)}{\partial b_{11}} & \frac{\partial(x_5+x_9)}{\partial b_{12}} & \frac{\partial(x_5+x_9)}{\partial a_{21}} \\ \frac{\partial x_4}{\partial a_{11}} & \frac{\partial x_4}{\partial a_{12}} & \frac{\partial x_4}{\partial a_{13}} & \frac{\partial x_4}{\partial b_{11}} & \frac{\partial x_4}{\partial b_{12}} & \frac{\partial x_4}{\partial a_{21}} \\ \hline \frac{\partial x_1}{\partial a_{22}} & \frac{\partial x_1}{\partial a_{23}} & \frac{\partial x_1}{\partial b_{21}} & \frac{\partial x_1}{\partial b_{22}} & \frac{\partial x_1}{\partial a_{33}} & \frac{\partial x_1}{\partial a_{34}} \\ \frac{\partial(x_2+x_7)}{\partial a_{22}} & \frac{\partial(x_2+x_7)}{\partial a_{23}} & \frac{\partial(x_2+x_7)}{\partial b_{21}} & \frac{\partial(x_2+x_7)}{\partial b_{22}} & \frac{\partial(x_2+x_7)}{\partial a_{33}} & \frac{\partial(x_2+x_7)}{\partial a_{34}} \\ \frac{\partial(x_5+x_9)}{\partial a_{22}} & \frac{\partial(x_5+x_9)}{\partial a_{23}} & \frac{\partial(x_5+x_9)}{\partial b_{21}} & \frac{\partial(x_5+x_9)}{\partial b_{22}} & \frac{\partial(x_5+x_9)}{\partial a_{33}} & \frac{\partial(x_5+x_9)}{\partial a_{34}} \\ \frac{\partial x_4}{\partial a_{22}} & \frac{\partial x_4}{\partial a_{23}} & \frac{\partial x_4}{\partial b_{21}} & \frac{\partial x_4}{\partial b_{22}} & \frac{\partial x_4}{\partial a_{33}} & \frac{\partial x_4}{\partial a_{34}} \\ \hline 0 & 0 & 0 & 0 & 0 & \\ \frac{\partial x_7}{\partial d_1} & \frac{\partial x_7}{\partial d_2} & \frac{\partial x_7}{\partial d_3} & \frac{\partial x_7}{\partial d_2} & \frac{\partial x_7}{\partial d_3} & \\ \frac{\partial x_9}{\partial d_1} & \frac{\partial x_9}{\partial d_2} & \frac{\partial x_9}{\partial d_3} & \frac{\partial x_9}{\partial d_2} & \frac{\partial x_9}{\partial d_3} & \\ 0 & 0 & 0 & 0 & 0 & \end{pmatrix} \quad (5)$$

Each element of matrix $\nabla c X$ is obtained by resolving the differential equation.

The method of $\frac{\partial x_1}{\partial a_{11}}, \frac{\partial x_2}{\partial a_{11}}, \frac{\partial x_3}{\partial a_{11}}, \frac{\partial x_4}{\partial a_{11}}, \frac{\partial x_5}{\partial a_{11}}, \frac{\partial x_6}{\partial a_{11}}, \frac{\partial x_7}{\partial a_{11}}$

Resolving the following differential equations:

$$\begin{aligned}\frac{\partial \dot{x}_1}{\partial a_{11}} &= a_{11} F_{11}(t) \frac{\partial x_1}{\partial a_{11}} + a_{12} F_{12}(t) \frac{\partial x_2}{\partial a_{11}} + a_{13} F_{13}(t) \frac{\partial x_3}{\partial a_{11}} \\ &\quad + F_{11}(t) x_1 \frac{\partial \dot{x}_2}{\partial a_{11}} = a_{21} F_{21}(t) \frac{\partial x_1}{\partial a_{11}} + a_{22} F_{22}(t) \frac{\partial x_2}{\partial a_{11}} \\ &\quad + a_{23} F_{23}(t) \frac{\partial x_3}{\partial a_{11}} \\ \frac{\partial \dot{x}_3}{\partial a_{11}} &= \frac{a(t)}{57.3} \frac{\partial x_1}{\partial a_{11}} + \frac{\partial x_2}{\partial a_{11}} + a_{33} F_{33}(t) \frac{\partial x_3}{\partial a_{11}} + a_{34} F_{34}(t) \frac{\partial x_4}{\partial a_{11}} \\ \frac{\partial \dot{x}_4}{\partial a_{11}} &= \frac{\partial x_1}{\partial a_{11}} \\ \frac{\partial \dot{x}_5}{\partial a_{11}} &= \frac{\partial x_2}{\partial a_{11}} \\ \frac{\partial \dot{x}_6}{\partial a_{11}} &= \frac{\partial x_3}{\partial a_{11}} \\ \frac{\partial \dot{x}_7}{\partial a_{11}} &= -\xi \omega \frac{\partial x_7}{\partial a_{11}} - \omega^2 \frac{\partial x_6}{\partial a_{11}} + d_1 H_1(t) \frac{\partial x_2}{\partial a_{11}} + d_3 H_3(t) \frac{\partial x_3}{\partial a_{11}}\end{aligned}$$

The coefficients of the above equation $a_{11}, a_{12}, a_{13}, a_{21}, a_{22}, a_{23}, a_{33}, a_{34}, \xi, \omega, d_1, d_3$ are the elements of vector c . In this iteration method we take the value of c_K to go through computations to obtain the value of c_{K+1} , therefore in resolving the above equations, these coefficients are already known values.

When assuming the prior conditions $t=t_0$:

$$\frac{\partial x_1(t_0)}{\partial a_{11}} = \frac{\partial x_2(t_0)}{\partial a_{11}} = \frac{\partial x_3(t_0)}{\partial a_{11}} = \frac{\partial x_4(t_0)}{\partial a_{11}} = \frac{\partial x_5(t_0)}{\partial a_{11}} = \frac{\partial x_6(t_0)}{\partial a_{11}} = \frac{\partial x_7(t_0)}{\partial a_{11}} = 0$$

If when $t=t_0$ flight trajectory is even and steady and variation is slow, this kind of assumption is permitted.

Resolving the above equation, we then can obtain:

$\frac{\partial x_1}{\partial a_{11}}, \frac{\partial x_2}{\partial a_{11}}, \frac{\partial x_3}{\partial a_{11}}, \frac{\partial x_4}{\partial a_{11}}, \frac{\partial x_5}{\partial a_{11}}, \frac{\partial x_6}{\partial a_{11}}, \frac{\partial x_7}{\partial a_{11}}$

Using a similar method we can obtain the yaw derivative of x_1 , x_2 , x_4 , x_5 , x_6 , and x_7 towards a_{12} , a_{13} , b_{11} , b_{12} , a_{21} , a_{22} , a_{23} , b_{21} , b_{22} , a_{33} , and a_{34} , and the yaw derivative of x_6 and x_7 towards ξ , ω , d_1 , d_2 , and d_3 .

After obtaining ∇cX , substitute equation (4), we then can use the iteration method to obtain vector c .

IV. APPLICATION

The following practical example from a flight test explains the application of the above variable coefficient aircraft system identification theory and formulas. Certain aircraft in the operation period emerge from steady flight and develop unsteady flight, so much that the flight diverges (See Fig. 1 through Fig. 5). Through investigating, the factors of unsteady flight are located in the aircraft's original mathematical model that is not accurate, if the aerodynamic data in the wind tunnel and the real aerodynamic data of the aircraft in flight test do not correspond, therefore it is necessary to compute the aircraft aerodynamic coefficient from the flight test data, and find the existing problem of the flight's instability.

The above aircraft mathematical model is a variable coefficient differential equation that includes elastic vibration (See equation 2).

The numeric value of the realistic aircraft system substituting with equation (2), the aerodynamic coefficients that are necessary to compute are regarded as undefined values, and we can obtain:

$$\begin{aligned}
\dot{x}_1 &= a_{11}(0.26t - 0.17)x_1 + a_{12}(0.26t - 0.17)x_2 + a_{13}(0.46t - 1.06)x_3 \\
&\quad + b_{11}(0.46t - 1.06)u_1 + b_{12}(0.46t - 1.06)u_2 \\
\dot{x}_2 &= a_{21}(0.26t - 0.17)x_1 + a_{22}(0.26t - 0.17)x_2 + a_{23}(0.46t - 1.06)x_3 \\
&\quad + b_{21}(0.46t - 1.06)u_1 + b_{22}(0.46t - 1.06)u_2 \\
\dot{x}_3 &= \frac{a(t)}{57.3}x_1 + x_1 + a_{33}(0.26t - 0.17)x_2 + \frac{0.1}{1+t}x_4 \\
\dot{x}_4 &= x_1 \\
\dot{x}_5 &= x_2 \\
\dot{x}_6 &= x_7 \\
\dot{x}_7 &= -\xi\omega x_7 - \omega^2 x_6 + d_1(0.4t - 0.82)u_1 + d_2(0.4t - 0.82)x_2 \\
&\quad + d_3(0.4t - 0.82)x_3 \\
x_8 &= x_1 + x_2 \\
x_9 &= x_6 + x_7
\end{aligned} \tag{6}$$

From flight test telemetered data we can obtain rudder yaw u_1 and u_2 . In equation (6), u_1 and u_2 are regarded as input symbols, therefore in identification computation, it is an already known value.

Flight test telemetered data also gives angle degree and angle velocity symbols x_1 _{measured}, x_8 _{measured}, x_9 _{measured}, x_4 _{measured}.

Applying formula (4), seeking the undefined coefficient in formula (6), causes the square and J as the smallest of the difference of x_1 , x_8 , x_9 , and x_4 that are computed in formula (6) and the measured values x_1 _{measured}, x_8 _{measured}, x_9 _{measured}, and x_4 _{measured}.

The computations in the computer clearly express that the undefined coefficients are many, they not only greatly increase computer time but also sometimes in the iteration process it is not easy to converge. The preliminary computations of the example in this text indicate that the above-mentioned aircraft elastic vibration only holds a very small amount in the exhaust numeric value of the yaw angle sensor and yaw angle velocity sensor. Under the premise that does not influence attainment of the aerodynamic coefficient value that plays a major role towards the instability process, the computer did not take ξ , ω , d_1 , d_2 , d_3 and regard them as undefined values, the damping

coefficient ξ and vibration frequency ω take the test value, and d_1 , d_2 , and d_3 take the designed value. By the aerodynamic coefficient that the computations obtained we see the following:

a_{11}	a_{12}	a_{13}	b_{11}	b_{12}	a_{21}	a_{22}	a_{23}	b_{21}	b_{22}	a_{33}
-1.55	-2.59	-0.06	-55.99	-2.41	0.15	-1.16	-41.6	-0.12	44.73	-0.85

Taking the aerodynamic coefficient that the computer obtained and substituting them with equation (6), we take the yaw u_1 and u_2 that the telemeter obtained as input, resolve equation (6), and computed value and flight test value can better agree (See Fig. 3 through Fig. 5).

When practically applying these aerodynamic parameters that identification computations obtained, because telemetered parameters always have errors, the bearing of this example of flight test did not in advance consider the requirements of identification computations, and errors were also somewhat large. Clearly we only must have those aerodynamic coefficients that were not very sensitive to the telemetered signal errors, then they can be believable. If these aerodynamic coefficients are closely linked together with the appearance of the aircraft of the whole flight test trajectory transformation, it has a significant influence on the flight test results, therefore even if the telemetered data has some error, after identification computations, these aerodynamic coefficients also cannot have a great many transformations.

In order to determine which aerodynamic coefficients possess relative stability toward the transformation of telemetered data, we made the following investigation: Taking the aileron deflation u_1 _{measured} and the yaw rudder deflection u_2 _{measured} of this example as the input signal, with each different disturbance on x_1 _{measured}, x_8 _{measured}, x_9 _{measured}, and x_4 _{measured} later take the telemetered value of this kind of artificial disturbance and regard it as a supposition measured value, and again form these supposition values carry out aerodynamic

coefficient identification computations. The computer results show the rising trajectory that corresponds to the rudder deflection transformation in this example, after each different disturbance, some aerodynamic coefficient variations are fairly large, but the aileron aerodynamic coefficient b_{11} and yaw rudder aerodynamic coefficient b_{22} however have corresponding stability. This explains the value of b_{11} and b_{22} possess certain believable degrees.

The rudder surface aerodynamic coefficients that identification computations obtain are much greater than originally designed values, causing amplification system of the aircraft and pilot apparatus return loop to greatly raise the original designed value. This then explains the factor of aircraft instability. In later test flights, we used reduced pilot apparatus return loop to amplify the coefficient in an equal manner, causing the aircraft to obtain a successful stable flight.

V. CONCLUDING REMARKS

This text researched the problem of aerodynamic coefficient identification of variable coefficient flight systems with elastic effect. Through the analysis of variable coefficient transformation regulations on inside equations, it turned the variable coefficient in the equation into a variable regulation already known function and unknown constant product, regarding these unknown constants as undefined coefficients, applying the Newton-Raphson method to reach the variable coefficient equation, and through iteration computation seek these undefined coefficients. This kind of method this text used is generally so that the parameter identification computation of the corresponding difficult variable coefficient aircraft system can be achieved. This text applies the above method to successfully compute its aerodynamic coefficient from the flight test data of one unsteady flight of an aircraft. When applying in practice the aerodynamic coefficients that the identification computations obtained, if the measurement errors are large, we must pay attention to the believable degree of the aerodynamic coefficient that these computations obtained in analysis and differen-

tation.

This work was carried out under the guidance of Comrade Bao Keming. In the process we obtained much help from Comrade Wang Guolin. Please accept my sincere thanks.

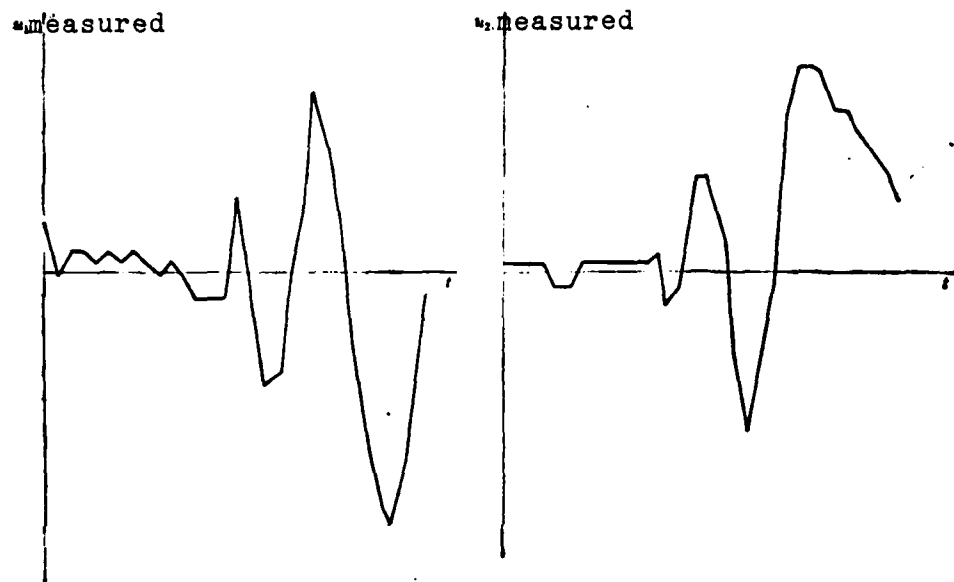


FIG. 1: THE TIME HISTORY OF
AILERON DEFLECTION MEASURED
IN FLIGHT

FIG. 2: THE TIME HISTORY OF
RUDDER DEFLECTION MEASURED
IN FLIGHT

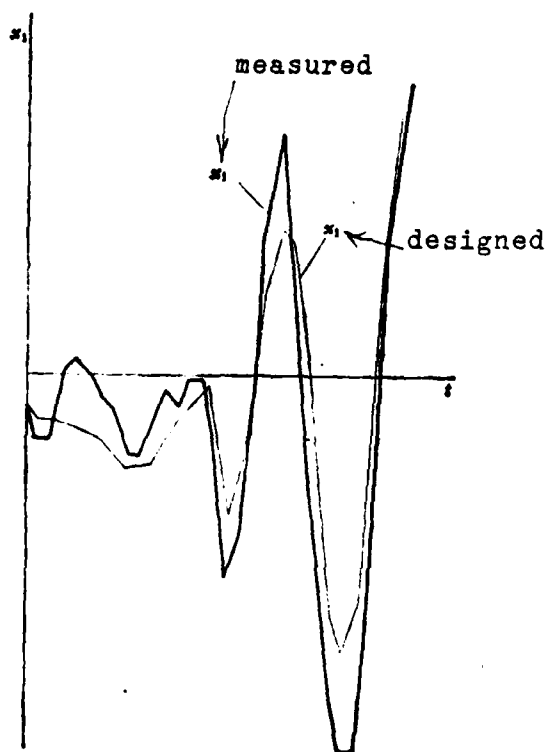


FIG. 3: COMPARISON OF ROLL RATE
TIME HISTORIES MEASURED IN FLIGHT
AND COMPUTED

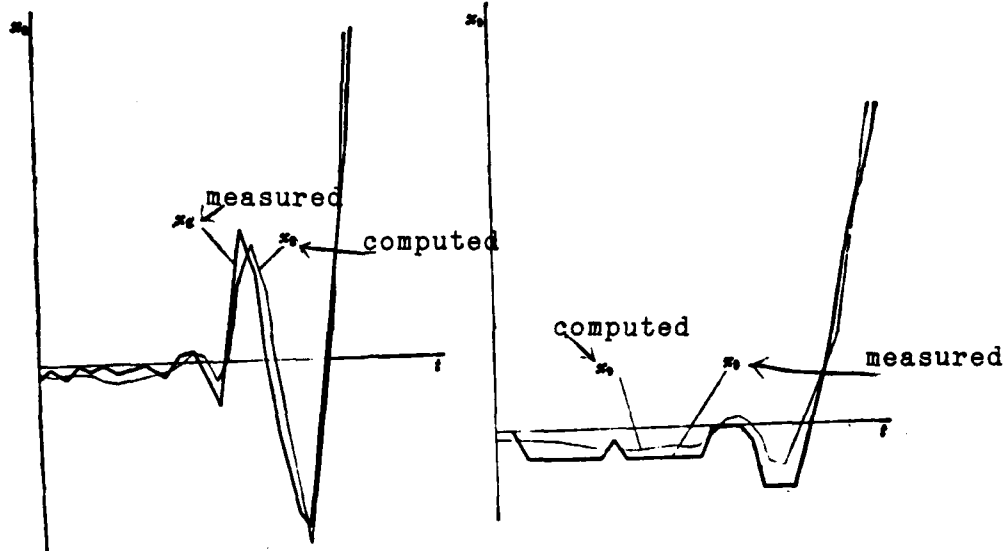


FIG. 4: COMPARISON OF YAW RATE TIME HISTORIES MEASURED IN FLIGHT AND COMPUTED

FIG. 5: COMPARISON OF YAW ANGLE TIME HISTORIES MEASURED IN FLIGHT AND COMPUTED

References:

- (1) Kenneth W. Iliff and Lawrence W. Taylor, Jr., Determination of Stability Derivative from Flight Data Using a Newton-Raphson Minimization Technique. NASA TN D-6678, 1972.
- (2) Methods for Aircraft State and Parameter Identification. ADA 013073, 1975.
- (3) Lie Bie Jie Fu Deng Zhu, Zhang Bingxuan Deng Yi: Wu Ren Jia Shi Fei Xing Dong Li Xue. Guo Fang Gong Ye Chu Ban She, 1964. " List of Outstanding Men and Works, Zhang Bingxuan and others, translators, Flight Mechanics of Unmanned Aircraft, National Defence Industry Publishing Bureau".

AN ADJUSTMENT METHOD AND ENGINEERING REALIZATION FOR CONTROL CURVES OF THE TWO-VARIABLE FUNCTION

Shao Rongshi

Design Department, Shenyuan Aircraft Corporation

Abstract:

Through designing a bypass-door system for a supersonic aircraft, which implemented adjustment in conformity to the control curves of the two-variable function (Fig. 1), a method for engineering realization of some separable multivariable functions has been put forward. It means, for any control function of n variables $f(x_1, x_2, \dots, x_n)$, if

$$\frac{\partial f(x_1, x_2, \dots, x_n)}{\partial x_i \partial x_j} = 0 \quad i, j = 1, 2, \dots, n.$$

the function, called separable by the author, can be divided into subfunction of each single variable, then the sum of these subfunctions is just equal to the original function, i.e.

$$f(x_1, x_2, \dots, x_n) = f_1(x_1) + f_2(x_2) + \dots + f_n(x_n).$$

A practical bridge circuit with parameters realizing the control curves for the bypass-door has been designed (see Fig. 4).

Moreover, the simple method of changing the characteristics of the control curves by adjusting resistors on the bridge arms has been adopted according to the test flight requirements of the system, and an actual numerical example has been given.

The above mentioned engineering realization and adjustment method for the two-variable function have done their bit for the research on the simulator reproducing the function of more than two variables and may be also valuable for design of the system with multiple input but single out-put.

I. INTRODUCTION

The design of many automatic adjustment systems in modern aircraft design requires a controlled target according to predetermined multi-variable function curves to carry out open formula adjustments. For example, the air intake passageway of the high speed fighter plane requires according to M number and flight angle of attack these two parameters to adjust the air intake cone⁽¹⁾ or oblique plate; the

motorized wing flap of the whole front edge of the wing spread of America's light duty combat plane YF-16 follows angle of attack increases and automatic lower incline, and follows the increases and automatic upper convergence of the M number⁽²⁾. The key problem of the system design of the compound existing multi-variable function curve such as this type lies in what future single variable signals (x_1, x_2, \dots, x_n) of its own sensor to synthetically merge into control signal $f(x_1, x_2, \dots, x_n)$ that are in accord with curve requirements, and that these function curves are obtained in model design phases through wind tunnel tests and computations. In order to satisfy the requirements through test flights seeking the most favorable curve, the design of the system should be able to vary the predetermined curves within a fairly large range.

Using differential treatment aircraft to realize control of the multiple element function is feasible, but establishing contact with the aircraft load and adjusting the curve is difficult, therefore we can only seek the solution computation device for an aircraft electronic simulated test. The methods of the cone model cam of the adopted machinery, the electronic diode function generator, the electronic profile model, etc. to realize the two-variable function are comparatively complicated: "Using an electronic method to resolve binary function still up to now has had almost completely no development"⁽³⁾. "The research work of reproducing two or even more variable function transformation devices still has not even remotely reached the extent of perfection," "Three or even more variable functions using the above method simply cannot be reproduced"⁽⁴⁾. It is thus evident that these methods used to control systems are difficult, so far as to adjust transforming two-variable functions then is even more difficult to imagine. This text proposes a method for simplified engineered realization for some separable multi-variable functions to become single-variable functions, and designs a signal synthetic bridge. This not only resolves the realization and adjustment of a two-variable function bypass door, but also possesses reference value for the multi-variable function process.

II. THE REALIZATION OF THE BYPASS DOOR TWO-VARIABLE FUNCTION CURVES

Certain high speed aircraft bypass door system requirements are according to the two parameters of total temperature and M number to carry out control, its open angle is within the range of 0° ~ 10° with the rise and increase of total temperature, and at the same time with the increase and reduction of M number. Its control curves are shown in Fig. 1. In the figure, S is the effective open degree of the bypass door; S is the rectilinear displacement of the control motion tube.

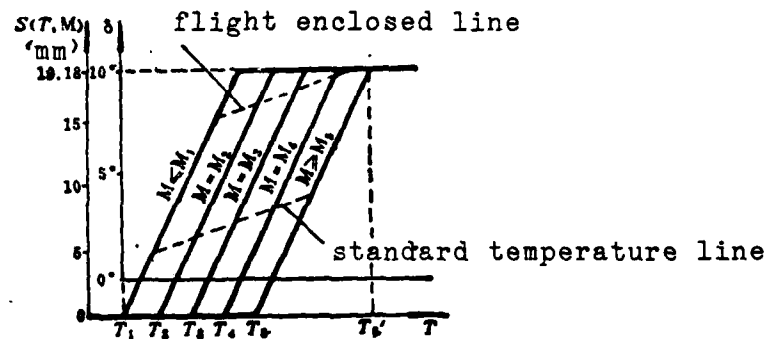


FIG. 1: CONTROL CURVES OF
THE BYPASS DOOR

1. RESOLUTION OF THE BYPASS DOOR TWO-VARIABLE FUNCTION CONTROL CURVES

In Fig. 1 the mathematical expression of the two-variable curve is:

$$S = \begin{cases} 0 & T < T_1 \\ 0.3688(T - T_1) & T_1 < T < T'_1 \quad T'_1 = T_1 + T'_1 - T_1 \\ 19.18 & T > T'_1 \end{cases} \quad (1)$$

$$T_1 = \begin{cases} T_1 & M < M_1 \\ T_1 + 150(M - M_1) & M_1 < M < M_2 \\ T_1 & M > M_2 \end{cases} \quad (2)$$

This way, a curve $S(T, M)$ in Fig. 1 can resolve as the two nonlinear curves that Fig. 2 shows, but they are not independent, because T_0 is the function of the M number. The aircraft load profile formula atmosphere data computer (central apparatus) only can export the single-variable function signal of the M number or total temperature. It cannot give out extensive function $f(T - T_0(M))$, therefore it is unnecessary with $S(T, M)$ to separate into two single functions $S_1(T)$ and $S_2(M)$ that are not interrelated.

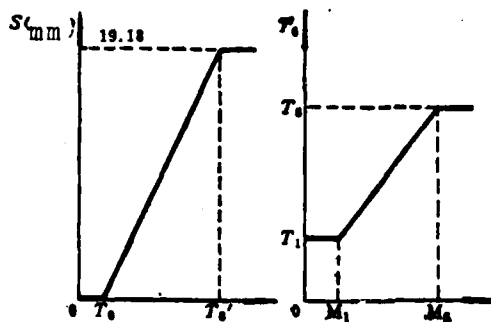


FIG. 2: DIVISION OF THE CURVES
IN FIG. 1

2. CONDITIONS FOR SEPARATION OF MULTI-VARIABLE FUNCTIONS

By unfolding the equation of the binary function we can know that so long as their intersecting incline derivative sum is zero, if:

$$\frac{\partial S(T, M)}{\partial T \partial M} = 0 \quad (3)$$

then two non-interrelated single-variable functions that are separable are engineered. If $\partial S(T, M)/\partial T$ is not related with the M number, $\partial S(T, M)/\partial M$ is not interrelated with T , then formula (3) is bound to obtain satisfaction. These kinds of curves inevitably are parallel with one another, if a certain basic curve follows the parallel displacement of a certain coordinate axis, the distance between the curves can be unequal, but they must be parallel. This is the fully required condition for a two-variable function to be able to carry out separation. It can extend to multi-variable functions:

Arbitrary multi-variable function $f(x_1, x_2, \dots, x_n)$, if its

second intersecting inclined derivative completely is zero,

$$\frac{\partial f(x_1, x_2, \dots, x_n)}{\partial x_i \partial x_j} \Big|_{i \neq j} = 0, \quad i, j = 1, 2, \dots, n \quad (4)$$

thus

$$f(x_1, x_2, \dots, x_n) = f_1(x_1) + f_2(x_2) + \dots + f_n(x_n) \quad (5)$$

This then is the theoretical basis of the engineered realization of a multi-variable function control system.

As to the binary function is Fig. 1, within the scope of boundary condition limitations is the linearized straight line of the distance equally between the curves, it can separate as two linear functions, and is a particular condition. If it is a curve where the distance between the curves is not equal but is mutually parallel, then it can separate as two single-variable nonlinear functions that are not inter-related. Taking $T=T_1$ and $M=M_1$ as primary points, with the control curves in Fig. 1 the region between $T_1 < T < T_5$, and $M_1 < M < M_5$ develops, if:

$$S(T, M) = S_1(T) + S_2(M) \quad (6)$$

$$S_1(T) = \begin{cases} 0 & T < T_1 \\ 0.3688(T - T_1) & T_1 < T < T_2 \\ 41.31 & T > T_2 \end{cases} \quad (7)$$

$$S_2(M) = \begin{cases} 0 & M < M_1 \\ -55.32(M - M_1) & M_1 < M < M_2 \\ -22.13 & M > M_2 \end{cases} \quad (8)$$

Boundary conditions

$$0 < S(T, M) = S_1(T) + S_2(M) < 19.18 \quad (9)$$

By the control motion tube and flight enclosed line there are limitations.

3. THE ENGINEERED REALIZATION OF THE BYPASS DOOR TWO-VARIABLE CONTROL CURVE

Using the electric profile model to reproduce formula (7) and (8) (See Fig. 3), with resistance characteristics as:

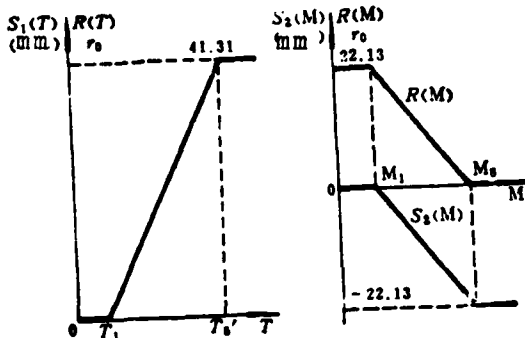


FIG. 3: SEPARATION OF THE CONTROL CURVES OF THE BYPASS DOOR AND THE RESISTANCE CHARACTERISTICS OF $R(T)$ AND $R(M)$

$$\begin{cases} R(T) = r_0 S_1(T) \\ R(M) = r_0 S_2(M) + 22.13 r_0 \end{cases} \quad (10)$$

The potentiometer separately is located in the total temperature sensor and the M number computer, when the control apparatus puts out resistance transformation r_c ohms, the control motion tube shifts 1mm. Substituting formula (6) with formula (10) we obtain:

$$S(T, M) = \frac{1}{r_0} (R(T) + R(M)) - 22.13 \quad (11)$$

In order to solve the curve of formula (11) realized in Fig. 1, we designed the bridge circuit that Fig. 4 shows, with the total temperature exhaust potentiometer R_T and M number exhaust potentiometer R_M strung together on bridge arm ob, its linking equation is: If total temperature rises then $R(T)$ increases; if M number increases then $R(M)$ reduces. By formulas (10) and (6) we can obtain ob supporting circuit total resistance:

$$R_{ob} = r_0 S(T, M) + 22.13 r_0 \quad (12)$$

The left and right door linear return potentiometer exhaust value $R(s)$ and motion tube movement distance S are in a direct ratio, if:

$$R(s) = r_0 S \quad (13)$$

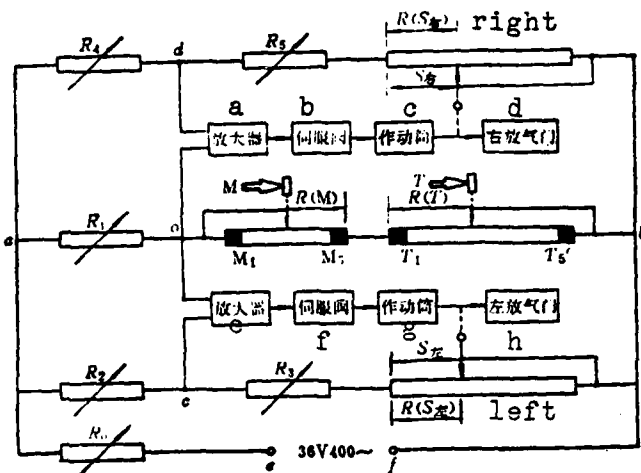


FIG. 4: SYNTHETIC BRIDGE OF THE CONTROL SYSTEM FOR THE BYPASS DOOR

KEY: (a) Amplifier; (b) Servo valve; (c) Motion tube; (d) Right bypass door; (e) Amplifier; (f) Servo valve; (g) Left bypass door.

Where r_o is the resistance on the return potentiometer unit length. Taking $R_3 = R_5 = 22.13r_o$, then cb or db support loop total resistance:

$$R_{cb} = r_o S + 22.13r_o \quad (14)$$

causes the system to possess a fairly high degree of exhaust sensitivity under standard atmosphere temperature within the range of $M_1 \leq M \leq M_5$ (See Fig. 1), taking:

$$R_1 = 30r_o, \quad R_2 = R_4 = 30r_o \quad (15)$$

r_o is the bridge piezoelectric resistance, in order to regulate the feedback system of the return exhaust potentiometer, and through system coordinate computations, take $R_o = 500 \Omega$.

When the total temperature T or M number change, the unequal piezoelectricity between oc(od) after being corrected through amplification controls the servo valve, drives the motion tube, controls the bypass door, and at the same time changes the return resistance. Due to the small valve ring, the frequency band of the hydraulic servo system is 5~10 cycle/second, and flight M number and total temperature are long cycle, slow transformation signs. Therefore, the left and right bypass

doors throughout conduct regulation of two-variable function curve according to what is shown in Fig. 1. Now taking the left door as an example we will prove whether or not it reproduces curve requirements. Because the bridge throughout is situated in balanced conditions, therefore we have:

$$R(s) = \frac{R_1}{R} [R(T) + R(M)] - R_s \quad (16)$$

With R_1 , R_2 , and R_3 substituting in the above formula and by formula (13) we can obtain:

$$S = \frac{1}{r_o} [R(T) + R(M)] - 22.13 \quad (17)$$

The right side of the equal sign of the above formula and formula (11) are completely identical, this shows the distance S of the movement of the motion tube is in complete accord with the binary function curve control $S(T, M)$ that Fig. 1 determined.

III. ADJUSTMENT OF THE TWO-VARIABLE FUNCTION CURVE OF THE BYPASS DOOR

In order to satisfy the requirements through a test flight seeking the best curve, we can manufacture a certain number of series of installations central apparatus components that have different control curves to provide for flight test selection. However, the central apparatus puts out ten kinds of control signals towards each system component of the whole aircraft. Therefore, in reality it is very difficult to satisfy this requirement of the system in this text, and having to transform the output component inside the central apparatus, then the end product is costly, and adjustment is not convenient. The adjustable resistance $R_1 - R_5$ that is set up on each arm of the synthetic bridge of this aircraft bypass door system not only can compensate for the null deviation of the left and right return transport potentiometer, what is even more important is through them the binary function curve curves of the central apparatus can be conveniently turned and shifted.

1. The Influence of the Change in R_1 on the Two-Variable Function Control Curves

Assume the bridge early matched condition is $R_{10} = 30r_c$, $R_{20} = R_{40} = 30r_o$,

and $R_{30} = R_{50} = 22.13r_0$. When R_1 by early condition R_{10} transforms ΔR_1 , if $R_1 = R_{10} + \Delta R_1$, the theoretical curve of the bypass door motion tube is:

$$S = \frac{1}{r_0} \left[\frac{R(T)}{1 + \Delta \bar{R}_1} + \frac{R(M)}{1 + \Delta \bar{R}_1} \right] - 22.13 \quad (18)$$

Contrasting formulas (17) and (18) we can see that the change in R_1 corresponds to the output characteristics that change the total pressure sensor and M number computer, the equivalent output characteristic equation of the central apparatus after the change in R_1 is:

$$R'(T) = \frac{R(T)}{1 + \Delta \bar{R}_1}, \quad R'(M) = \frac{R(M)}{1 + \Delta \bar{R}_1} \quad (19)$$

where $\Delta \bar{R}_1$ is the corresponding value of the change in R_1 , if $\Delta \bar{R}_1 = \Delta R_1 / R_{10}$. The influence of the change in R_1 is shown in Fig. 5. In the figure S only expresses the theoretical required value, in actuality the distance receives the nonlinear limitations of the motion tube, all the negative values can only correspond to the bypass door closed position. (This) can prove that the change in R_1 fully changes the beginning tone pitch S_0 and the end tone pitch S_1 of the motion tube (if a prescribed minimum and prescribed maximum of the curve), but its effective distance with the product of R_1 is a constant:

$$R_1 \cdot (S_1 - S_0) = \text{const} \quad (20)$$

This way then we can change the controlled range of the bypass door through adjusting R_1 , as to the shifting of the control position caused by the change in R_1 , we can higher and lower translate the curve through R_3 to compensate.

2. The Influence of the Change in R_2 on the Two-Variable Function Control Curve

The change in R_2 also can equivalently convert the change for the central apparatus output characteristics. Assume R_2 has an increment, for example $R_2 = R_{20}(1 + \Delta R_2)$. Then we have:

$$S = \frac{1}{r_0} ((1 + \Delta \bar{R}_2) R(T) + (1 + \Delta \bar{R}_2) R(M)) - 22.13 \quad (20)$$

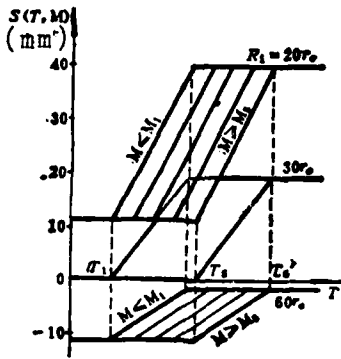


FIG. 5: EFFECT OF CHANGE
IN R_1 ON THE CONTROL
CURVES OF THE BYPASS DOOR

In that case the equivalent output characteristic of the central apparatus is:

$$R'(T) = (1 + \Delta \bar{R}_1) R(T), \quad R'(M) = (1 + \Delta \bar{R}_1) R(M) \quad (21)$$

The influence of the change in R_2 is shown in Fig. 6. Comparing it to Fig. 5, it is evident that the increased R_2 and the reduced R_1 have equal effects, provided $1 + \Delta \bar{R}_2 = 1 / (1 + \Delta \bar{R}_1)$, then the curves they correspond to are completely identical.

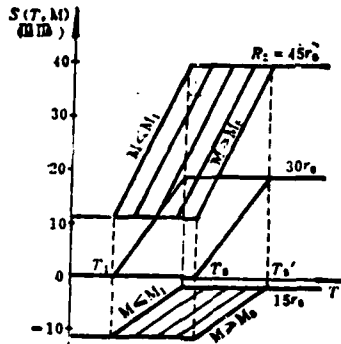


FIG. 6: EFFECT OF CHANGE
IN R_2 ON THE CONTROL CURVES
OF THE BYPASS DOOR

3. The Influence of the Change in R_3 on the Two Function Control Curves

By Fig. 5 and Fig. 6 we can see, the change in R_1 or R_2 can change

the effective control range of the slope and bypass door of the binary function curves, but with bringing the bypass door up to the shifting of the control position, in order to make the control angle degree become zero, it is necessary to take the curves after adjustment through the changes in R_1 and R_2 and move entirely along the vertical axis from top to bottom. This function depends on controlling R_3 to be realized.

When $R_3 = R_{30} + \Delta R_3$, by the bridge balanced condition we can obtain:

$$S = \frac{1}{r_s} [R(T) + R(M)] - 22.13 - \frac{\Delta R_3}{r_s} \quad (22)$$

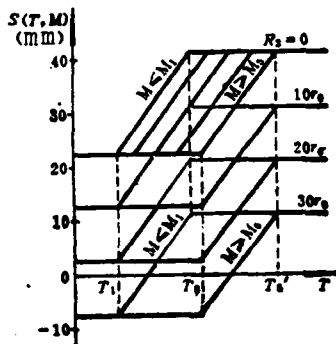


FIG. 7: EFFECT OF CHANGE
IN R_3 ON THE CONTROL CURVES
OF THE BYPASS DOOR

The influence of the change in R_3 is expressed in Fig. 7. By Fig. 7 and comparison of formulas (22) and (17) we can see that the change in R_3 does not change the condition of the curve and makes the whole curve up and down shift parallel. When R_3 increases, the whole curve shifts down, its translational quantity is equal to the increment of R_3 divided by the unit length resistance value of the return transport potentiometer.

4. Adjustment Method for Control Curves

Simultaneously changing adjustable resistance R_1 , R_2 , and R_3 makes:

$$\begin{cases} R_1 = R_{10} + \Delta R_1 = R_{10}(1 + \Delta \bar{R}_1) \\ R_2 = R_{20} + \Delta R_2 = R_{20}(1 + \Delta \bar{R}_2) \\ R_3 = R_{30} + \Delta R_3 \end{cases} \quad (23)$$

By the balanced condition of the bridge we can derive the movement curve of the motion tube:

$$S = \frac{1}{r_0} \left[\frac{1 + \Delta \bar{R}_2}{1 + \Delta R_1} R(T) + \frac{1 + \Delta \bar{R}_1}{1 + \Delta R_2} R(M) \right] - 22.13 - \frac{\Delta R_3}{r_0} \quad (24)$$

Substituting formula (24) with formula (10) we obtain:

$$S = kS(T, M) + S_0 \quad (25)$$

Where:

$$\begin{cases} k = \frac{1 + \Delta \bar{R}_2}{1 + \Delta R_1} \\ S_0 = 22.13(k - 1) - \frac{\Delta R_3}{r_0} \end{cases} \quad (26)$$

Formula (25) shows, due to the changes in R_1 , R_2 , and R_3 , causes the binary function curve of Fig. 1 to amplify the back section of k completely along the vertical axis direction translating up and down S_0 mm. With the boundary conditions formula (9) of $S(T, M)$ substitute formula (25), we obtain the effective control range of the motion tube:

$$\Delta S = S_i - S_o = 19.18 k \quad (27)$$

As to the arbitrarily determined bypass door control range, we determine the k value by formula (27). As to the already known k value, based on formula (26), the selection of R_1 and R_2 can have many kinds, to make R_1 and R_2 both possess comparatively small amounts of changes, assume:

$$k < 1: \begin{cases} \Delta \bar{R}_1 = \Delta \bar{R} \\ \Delta R_2 = -\Delta \bar{R} \end{cases}, \quad k > 1: \begin{cases} \Delta \bar{R}_2 = \Delta \bar{R} \\ \Delta R_1 = -\Delta \bar{R} \end{cases} \quad (28)$$

The selection of $\Delta \bar{R}$ seen in Fig. 8, when $k < 1$, we can choose $1/(1 + \Delta \bar{R}_1)$; $1 - \Delta \bar{R}_2$, $(1 - \Delta \bar{R}_2)/(1 + \Delta \bar{R}_1)$; when $k > 1$, we can choose $1 + \Delta \bar{R}_2$, $1/(1 - \Delta \bar{R}_1)$, $(1 + \Delta \bar{R}_1)/(1 - \Delta \bar{R}_1)$. Generally we select $\Delta \bar{R} = 0.1 \sim 0.5$. This way it is

both convenient to adjust, and ensures the degree of sensitivity of the output of the bridge.

5. Practice Examples of Adjustment

Assuming the central apparatus determined curve as shown in Fig. 1, the required design adjusted bridge arm resistance makes the bypass door automatically controlled according to the curve in Fig. 9 within the range of $0^\circ \sim 5^\circ$ according to the two parameters of total temperature and M number.

The 5° corner of the bypass door through the rocker arm corresponds to the rectilinear displacement $S_1 = 10.92\text{mm}$ of the motion tube, requiring $S_0 = 0$, therefore:

$$\Delta S = S_1 - S_0 = 10.92\text{mm} \quad (29)$$

By formula (27) we obtain:

$$k = \frac{\Delta S}{19.18} = 0.5693 \quad (30)$$

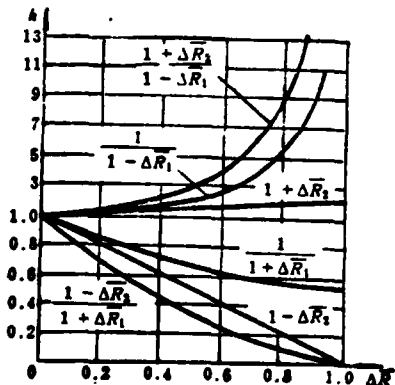


FIG. 8: EFFECT OF CHANGE
IN ΔR ON k

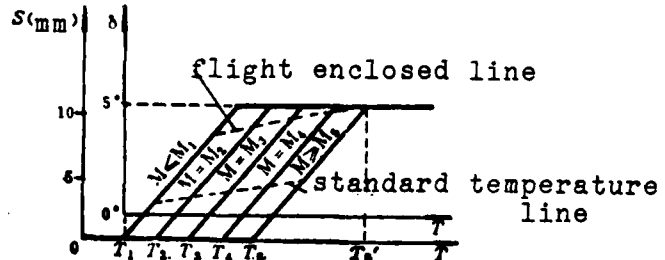


FIG. 9: CONTROL CURVES OF THE
BYPASS DOOR FROM 0° to 5°

Refering to Fig. 8, taking the form of $k = (1 - \Delta \bar{R}) / (1 + \Delta \bar{R})$ (other forms will make $\Delta \bar{R}$ enlarge), and substituting the already known k value we obtain:

$$\Delta \bar{R} = 0.2745 \quad (31)$$

By formula (23) we obtain:

$$R_1 = R_{10}(1 + \Delta \bar{R}) = 38.235 r_0 \quad (32)$$

$$R_2 = R_{20}(1 - \Delta \bar{R}) = 21.765 r_0 \quad (33)$$

Making $S_0 = 0$ in formula (26), we obtain ΔR_3 , and already known $\Delta R_{30} = 22.13 r_0$, therefore we obtain:

$$R_3 = 22.13 k r_0 = 12.06 r_0 \quad (34)$$

the right door parameters: $R_4 = R_2$, $R_5 = R_{30}$.

IV. CONCLUSION

The control target of many flight control systems except carrying out control according to a direct variable, often still must be affected by one or two other parameters to conduct correction and compensation. This type of designed channel of open formula control system of multiple intake-single exhaust takes the multi-parameter function signal synthesis of its own variable sensor as a control signal, it later is the design and synthesis of the single intake-single output system of constant curves. The method of engineered realization of separation of the two-variable function control curve of the bypass door that this text expounds on, through practice proof is feasible. This method can extend to the multi element function research. The engineered multi-variable function, many permitted similar simplifications are separable multi-variable functions. Their mathematical weakness is their two intersecting partial derivatives completely are null, the properties in the figure are parallel shifts of one one-dimension control function in n dimensional space. This type of function can become a single-variable function sought to be realized.

Through the method of adjusting the bridge arm resistance to change the binary function control curves, installation control test proof is

simply and conveniently feasible. It not only makes the bypass door curve along the vertical axis direction adjustment, but also can, within a specified range, make the whole curve along the model axis shift towards the right. This is through adjusting R_1 through R_3 and making $S_o < 0$ in formula (26), and the realistic movement of the motion tube can only realize the $S \geq 0$ section to be completed. By Fig. 1 we can know, along the model axis the largest shiftable range is $\Delta T = T'_5 - T_5$. Aside from this we still must point out, in on-site aircraft tests, we only must grasp the influence of the changes in R_1 through R_5 on the control curves and use the collective test method of controlling while measuring. We do not use the theoretic computation if we can make the bypass door curve based on necessary conducted adjustment.

The method for an engineered realization of the separable multi-variable function that this text introduces, and the methods of the synthetic bridge of Fig. 4 and the bridge arm resistance going through adjustment to change the curve, possess a specified reference value to the research of analogue devices of the compound existing three above variable functions and the engineered design of a multiple input-single exhaust system.

References:

- 1) Shao Rong Shi, Dan Bian Liang Han Shu Tiao Jie Gui Lui De Gong Cheng Shi Xian He Tiao Zheng Fang Fa, Xin Xiao Yu Kong Zhi, "Shao Rongshi, The Engineered Realization and Adjustment Method of Single-Variable Function Control Curves, Information and Control Vol. 10, No. 4, August 8, 1981, P36-40"
- 2) Shao Rongshi, Kong Zhan Ji Dong Jin Yi, Guo Ji Hang Kong, " Shao Rongshi, Motorized Wing Flaps in Aerial Combat, International Aviation Vol. 4, 1979, P16-19.
- 3) Я.В. Нур Узбек Фу А.Н. Лие Бие Жи Фу Зи, Жи Суан Жи Ти Чхуанг Зи, Ву Ченшоу, Лу Чжоншэн, И, Шанг Хай Ке Хуэ Жи Шу Чху Бан Се, "Device for Solving Problems in the Computer", Wu Zhenshao, Lu Zhongshen, translators, Shanghai Science and Technology Publishing Bureau, September, 1961, P221-291".
- 4) Б.Я. Ганьчжу, Дин Ци Му Си Чхуанг Жи Жи Qi Zai Yan Jiu Zi Dong Tiao Jie Xi Tong Zhong De Ying Yong, Zhong Guo Ke Xue Yuan Zi Dong Hua Yan Jiu Suo Qing Hua Da Xue Zi Dong Kong Zhi Xi Yi Ke Xue Chu Ban She, "Electronic Analogue Device and its Application in Researching Automatic Control Systems, China Science Institute, Automation Research Group, Qing Hua University Automatic Control Systems Coding, Science Publishing Bureau, 1960, P177-188".

- [5] Walter J. Karplus, Walter W. Soroka, ANALOG METHODS, Computation and Simulation, McGRAW-HILL BOOK COMPANY, New York, 1959, P. 88-93.
- [6] Albert S. Jackson, ANALOG COMPUTATION, McGRAW COMP., New York, 1960, P. 482-488.
- [7] Clarence L. Johnson, ANALOG COMPUTER TECHNIQUES, McGRAW COMP., New York, 1958, P. 159-163.
- [8] A. E. Rogers, T. W. Connolly, Analog Computation in Engineering Design, McGRAW COMP., New York, 1960 P 38-42.
- [9] Y. J. Wong, W. E. OTT, FUNCTION CIRCUITS, Design and Applications, McGRAW-HILL, 1976, P. 177-212.

STRAIN FATIGUE PROPERTIES AND FATIGUE DISLOCATION STRUCTURES OF 2024 ALUMINUM ALLOY

Li Qingsheng, Tsai Chikung, Chen Xianxi, Pan Tianxi
Central Iron and Steel Research Institute
Zhou Zhaoxiang
Hongan Corporation

Abstract:

This paper mainly deals with the relation between the strain fatigue properties and the fatigue dislocation structures in 2024 aluminum alloy. Some interesting features of the fatigue dislocation structure in this commercial alloy are observed.

The analysis of deformation work density δ_{de} for smooth fatigue specimens shows that the strain fatigue properties of specimens aged at 240°C are much better than naturally aged specimens at high strain level.

Systematic study of fatigue dislocation structures in this alloy under the transmission electron microscope reveals that wavy slip mode at high strain level and plain slip mode at low strain level are characteristics of the dislocation slip in the naturally aged specimens, in contrast cross slip is much easier in the 240°C aged specimens at different strain levels. By foil thickness analysis the existence of {112} slip plane in 240°C aged specimens was confirmed.

It is also pointed out that the helical dislocations in the alloy are formed through cutting of moving dislocations with dislocation loops.

The conclusion has been drawn that the features of dislocation slip serve as an essential factor which affects the interaction of dislocations with other microstructures and determines the fatigue properties.

I. MATERIALS AND ACTUAL TEST METHODS

We used two kinds of aging system smooth cylinder specimens to carry out strain control fatigue tests, and separately researched the dislocation structure of forward added load and rear fatigue cracks. The material selected is standard component LY-12 aluminum alloy.

The two kinds of aging systems are:

Naturally aged: 500°C, two hr water tempered, aged 7 days or more.

Artificially aged: 500°C, 2 hr water tempered, aged 230°C 4 hr.

The one-way tensile yielding strength of the two kinds of aging system specimens, the tensile strength, and the cycle yielding strength are seen in Table 1.

TABLE 1. MECHANICAL PROPERTIES OF NATURALLY AGED AND 240°C AGED SPECIMENS

	Yielding Strength σ_y	Tensile Strength σ_t	Elasticity E	Cycle Yielding Strength σ_{yy}
Naturally Aged	42.5	59	7500	47.5
Artificially Aged	32	42	7600	28

(units are all kg/mm²)

The specimen is a Ø 13 round stick sample, the surface has a smooth finish V8 or higher. The specimen conducted strain control fatigue tests on an Instron 1255 test computer. After the cycle crack, at the source spot of the crack opening, vertical to the crack surface using a line corresponding to the computer we take a 0.3mm piece of foil. For the specimen of no added load, we take a piece of foil of the same thickness from the specimen central section. After using up to 600# sand paper and polishing up to 50 μ with a foil piece, we use a solution of 2:1 methanol: nitric acid, and a dual injection electrolysis buff. The foil is observed in a JSEM-200 electron microscope.

II. RESULTS AND ANALYSIS OF ACTUAL TESTS

1. The strain fatigue actual test results and their method of deformation work degree are described. Test results of strain fatigue with the specimens of the two kinds of aging treatments and the use of molded strain amplitude $\frac{1}{2}\Delta\varepsilon_0$ are described, as shown in Fig. 1. At high strain level, the relationship between $\frac{1}{2}\Delta\varepsilon_0$, the artificially aged specimen and fatigue life Nf can be expressed as:

$$\frac{1}{2}\Delta\varepsilon_0 = 0.03N_f^{0.4} \quad (1)$$

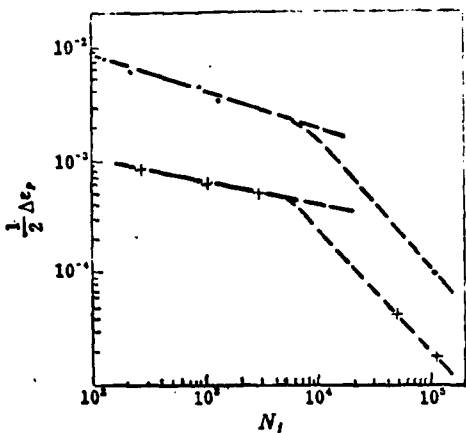


FIG. 1: RELATION BETWEEN $\frac{1}{2}\Delta\varepsilon$,
AND N_f
• Aged at 240° C
+ Aged naturally

The naturally aged specimen can be expressed as:

$$\frac{1}{2}\Delta\varepsilon = 0.003N_f^{0.22} \quad (2)$$

In the range of low strain (life reaches $10^3 \sim 10^4$), the test data all clearly diverges the Coffin-Manson model relationship such as formulas (1) and (2) express.

Literature (1) and (2) separately, from theory and actual tests, pose and prove within the range of extensive life ($10^1 \sim 10^5$ times), the use of deformation work degree to replace the molded strain amplitude, and regard as strain fatigue damage to describe the rationalization of the parameters.

We use the deformation work degree to sort out the data of Fig. 1. The results are as shown in Fig. 2.

The relation between the artificially aged specimen deformation work degree $\int \sigma d\varepsilon$ and N_f can be expressed as:

$$\int \sigma d\varepsilon = 3.22N_f^{0.300} \quad (3)$$

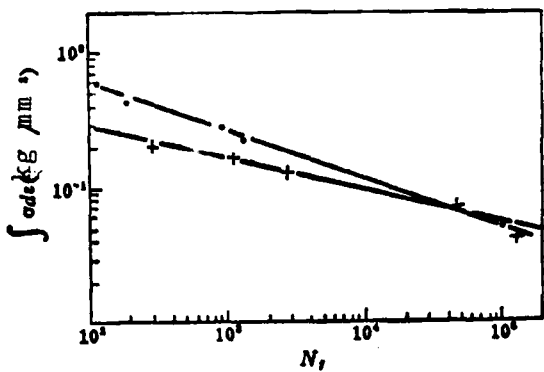


FIG. 2: RELATION BETWEEN $\int \sigma d\epsilon$
AND N_f
•Aged at 240° C
+Aged naturally

In accordance with the equation for the naturally aged specimen:

$$\int \sigma d\epsilon = 1.24 N_f^{0.28} \quad (4)$$

As Fig. 2 shows, the slope of the artificially aged specimen is fairly large, following the reduction of deformation work degree, the data of the naturally aged specimen is gradually approached. Therefore, artificially aged specimens have even more superior strain fatigue performance when enduring comparatively high strain.

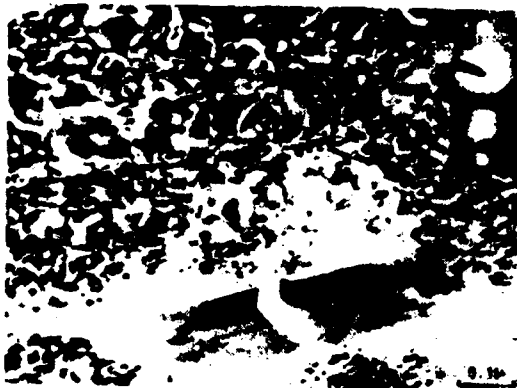


FIG. 3: FATIGUE DISLOCATION IN
NATURALLY AGED SPECIMENS AT HIGH
STRAIN LEVEL ($N_f=15$)

2. Strain dislocation structure and analysis. Microscopic analysis of the foil transmission reveals: the difference of the fatigue dislocation structure of the two kinds of aging system samples at different strain levels is unusually striking.

The naturally aged specimen: In the range of high strain, dislocation bends, for the time being are uniformly distributed, demonstrating wavy slip characteristics. Figure 3 shows this kind of characteristic, in the lower part of Fig. 3 is the inclusion (Fe, Mn, Si) Al_6 of the crack opening under the effect of dislocation. In this kind of condition, microcosmic mould strain distribution is uniform, the fatigue damage distribution of the inclusion open crack formation is also uniform, this is simply the reason for the macroscopic quantity $\frac{1}{2}\Delta\epsilon$, and fatigue life N_f in accord with the Coffin-Manson relation.

Following the reduction of strain quantity, the degree of dislocation reduces, when strain quantity is less than the strain quantity that corresponds to $10^3\sim 10^4$ number of cycles, the dislocation configuration has substantial change.

In the range of low strain, the typical dislocation configuration is as shown in Fig. 4. Figure 4-A shows the gathering and remaining wavy slip band of inclusion around dislocation.

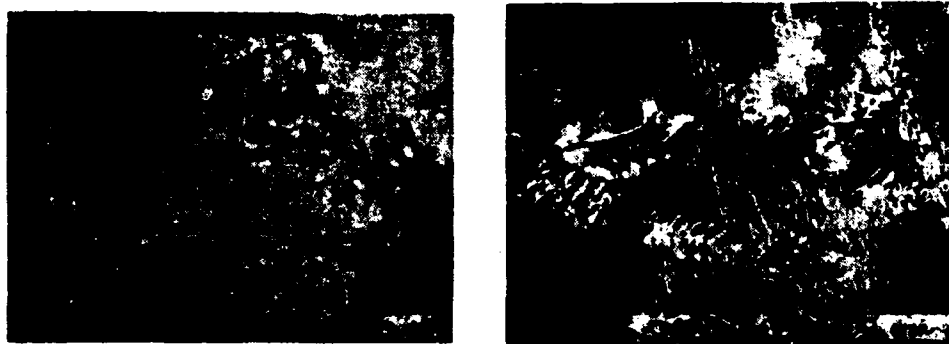


FIG. 4: FATIGUE DISLOCATION IN NATURALLY AGED SPECIMENS AT LOW STRAIN LEVEL ($N_f=1.2 \times 10^5$). A. Electron beam direction (112)

Figure 4-B shows dislocation of dislocation mesh and strategic position area of inclusion of the specimen surface form.

Because the dislocation plane is wavy slip, the form remains a wavy slip band. In the band the GP region repeatedly sheared and resolved by displacement, this kind of microcosmic organization deteriorates, and promotes the fatigue crack veins in the band to form and expand in the early stage. Because dislocation is highly concentrated in the wavy slip band, microcosmic strain distribution is not uniform. Moreover, fatigue damage in the wavy slip band that the GP region helps bring about also is local. This way, using macroscopic quantity $\frac{1}{2} \Delta e$, to express the Coffin-Manson relation of fatigue damage to forecast fatigue life, then the results obtained will be much higher than in reality.

Artificially aged specimen: Figures 5 and 6 separately express the microcosmic organization and fatigue dislocation structure in the range of high and low strain. As Fig. 5 and Fig. 6 show, artificially aged specimens have alike foil condition S' that the edge base of {100} plane separates out. In the range of low strain, this alike S' can have advancement towards the formation of fatigue crack veins, creating divergence to the Coffin-Manson relation.

As Fig. 5 and Fig. 6 show, in the range of high strain, degree of dislocation is high, in the range of low strain, degree of dislocation is low; additionally, on the line of dislocation all the sediment is separated out.



FIG. 5: FATIGUE DISLOCATION
IN ARTIFICIALLY AGED SPECIMEN
AT HIGH STRAIN LEVEL ($N_f = 225$)

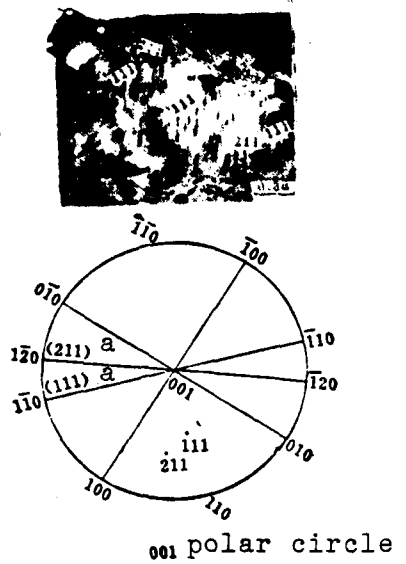


FIG. 6: POLE FATIGUE ANALYSIS
OF DISLOCATIONS IN (211) PLANE
KEY: (a) trace.

With artificially aged specimens, dislocation is easy to interact with wavy slip. Aside from dislocation in 111 plane, we still have dislocation in 112 plane. As Fig. 6 shows, three comparatively wide dislocations, their trace lines (the connecting lines of the extreme points of dislocation) are 110 direction, pole analysis reveals, they possibly are dislocations in plane 111. The upper left side dislocation trace lines are 120 direction, possibly are dislocations in 211 plane, neighboring dislocations, and should correspond to the same foil thickness. Different crystallography planes with foil plane included angle α , degree of dislocation s , and foil thickness t should satisfy:

$$t = \text{st}_{\mathcal{R}} a \quad (5)$$

Corresponding to neighboring dislocation, we should have:

$$\frac{s_1}{s_2} = \frac{\operatorname{tg} \alpha_2}{\operatorname{tg} \alpha_1} \quad (6)$$

Plane 211 and plane 001 (foil plane) included angle is 65.9° , plane 111 and plane 001 included angle is 54.73° ; actual measurement of s_1 is 6mm, and s_2 is 4mm. The above data is basically in accord

with formula (6). By this we can prove, the upper left dislocation of Fig. 6 is dislocation in the 211 plane.

Literature [3] had produced the existing wavy slip 112 plane in pure aluminum 60 C tensile specimen. LY-12 aluminum alloy artificially aged specimens in conditions of room temperature and cyclic load have dislocations existing in 112 plane. This fact points out the possibility of wavy slip in 112 plane. The lower left dislocation in Fig. 5, possibly is the condition of wavy slip intersecting with 111 plane by 211 plane.

With artificially aged specimens, dislocation is easy to intersect with wavy slip. This way, the possibility of forming a remaining wavy slip band and a strategic area of inclusion reduces. This is the reason for the favorable strain fatigue performance of the artificially aged specimen compared to the naturally aged specimen. E.J. Coyne's [3] work on the Al-Zn-Mg alloy also produced a good fatigue performance of aged samples, and attributed the reason to the dislocation being easy to intersect with wavy slip.

Helical dislocation: Helical dislocation is a particular kind of dislocation of the above alloy. Artificially aged, no added load condition then has a certain amount of helical dislocation. Figure 7 is the appearance of the dark field of the weak bond of helical dislocation under this condition. A shows the intersection of a moving dislocation and a hoop dislocation. The lower right side of A still has an independent hoop dislocation. We point out that the above helical dislocation system was formed through cutting of moving dislocations by the empty position collapsing and the formed hoop dislocation that were produced by fire tempering.

In artificially aged specimens after fatigue cracks, the changes in form and appearance of helical dislocation are not large.

Naturally aged specimens and conditions of no added load only have very small amounts of helical dislocation. After fatigue cracks, hel-



FIG. 7: HELICAL DISLOCATION
IN ARTIFICIALLY AGED SPECIMEN
BEFORE LOADING

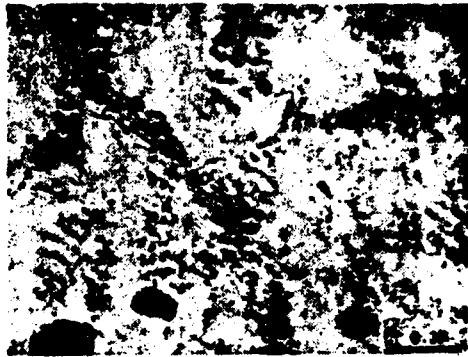


FIG. 8: HELICAL DISLOCATION
IN NATURALLY AGED SPECIMEN
AFTER FATIGUE CRACKS

ical dislocation amount increases. Figure 8 shows the high degree of dislocation concentration that helical dislocation produces after fatigue cracks. In artificially aged specimen comparisons, this possibly is related to the intersection of wavy slip performance with dislocation.

III. CONCLUSION

1. Using the degree of deformation work we can describe very well the strain fatigue laws of different time conditions with the LY-12 aluminum alloy. In the range of high strain, artificially aged specimens have obvious advantageous strain fatigue performance.
2. In heat treatment systems, strain quantities all change fatigue dislocation configurations and wavy slip characteristics.
3. Artificially aged specimens, under conditions of room temperature and cycle load, have dislocation existing in 112 plane, and can have wavy slip in 112 plane.
4. Helical dislocation systems in LY-12 aluminum alloy are formed by cutting of moving dislocations with dislocation loops.

Comrades Jin Shuzhen and Wu Qiaotian, and the computer section of the Electronic Research and Data Group assisted in conducting

sections of the test operations. We hereby express our thanks.

Reference Literature

- 1) Tsai Chikung, Jin Shu Xue Bao, 1976 Nian 12 Juan 1 Qi 45 Ye.
"Tsai Chikung, Journal of Metals, Vol. 12 No. 1 1976, Page 45".
- (2) M. Fuentes, J. Gil, Sevillano, J. J. Urcola and J. C. Zubillaga, "Unusual Slip Systems on High Purity Aluminium Single-Crystals", Scripta Metallurgica Vol 12 (1978) P169.
- (3) Coyne, E. J., Starke, E. A. later. J. of Frac Vol. 15, No. 5, P405.

STUDY ON MICROSTRUCTURE OF CARBON-ALUMINUM COMPOSITES

Zheng Lide, Zhang Guoding, Wang Wenrong, Shi Peiyuan
Shanghai Communications University

Abstract:

The microstructure of carbon-aluminum composites is close related with their technological process. Therefore, the problems in the process can be discovered by studying the features of the microstructure, and available information can be obtained further to choose the process parameters correctly, to improve the technological process and to enhance the properties of the fibers and composites.

The microstructures of the carbon fibers, the carbon fibers coated with nickle, the carbon fibers with nickle layer after vacuum heat treatment, carbon-aluminum composite wires and their specimens fabricated by hot pressing under the different technological conditions have been taken with the metallographic and sweep electron microscopes and are presented in this paper.

Carbon-aluminum composite material is a new type of composition of material that has had rapid development in the last twenty years. It has a higher strength, higher mould capacity, high temperature performance that is good, and excellent properties of dimensional stability. This material has very great potential in applications to space navigation and aeronautics industries. The properties of carbon-aluminum composites are closely related to the technological processes of basic type, carbon fiber surface coating and metal liquid state soaking and hot press solidification, and especially are directly related to the microstructures and defects. Therefore, to research the microstructures and defects of plated carbon fiber coats after coating treatment or carbon fibers with basic application, and carbon-aluminum composites after soaking and hot press solidification can be to research a definite, rational technological process and parameters and their influence on the microstructure and properties of carbon-aluminum composites; the combining and interaction between fiber and basic (or plated coating) provides an important reference and foundation.

This text uses the method of an optical microscope and sweep electron microscope to conduct analysis and research on the microstructure and fracture of nickel-plated carbon fibers, the nickel-plated carbon fibers after vacuum heat treatment, carbon-aluminum composite wires, and carbon-aluminum composite material.

EXPERIMENTS

The analysis of microstructures of carbon-aluminum composites primarily researches the characteristics of the microstructure and its transformation of carbon fibers, coatings and carbon-aluminum composites in each technological process that prepares the carbon-aluminum composite. In the text we adopt metallographic analysis method to investigate the uniformity of the carbon fiber coating, the interaction of heat-treated carbon fibers and nickel layer, the distribution of fibers in hot-press solidified carbon-aluminum composites, the binding conditions of fiber and basic, and carbon-aluminum composite wire composites. In metallographic analysis, because there is a big difference in the properties of various metals in the specimen, therefore the process of preparing the specimen has a very great influence on whether or not the microstructure and defects are correctly shown. The prepared specimen can use two methods of preparation which are using 6101 epoxy resin and ethylene diamine solidifier according to appropriate proportions to carry out casting, or using bakelite powder to hot-press.

Additionally, we still use the sweep electron microscope to observe and analyze the interaction of fractures and carbon fibers with the nickel of the nickel-plated carbon fiber carbon-aluminum composite wires, and the hot-press solidified carbon-aluminum composite plates.

The preparation method and technological process conditions of the various specimens that this text used already have detailed explanation in related texts ^(1~3), we will not again repeat it here.

1. The Microstructure of Nickel-Plated Carbon Fibers

In order to improve the binding between carbon fibers and alum-

inum, we use a chemical nickel-plating method on the carbon fiber surface to plate one layer of nickel. Tests prove that it has an excellent result in promoting carbon fiber and aluminum composites⁽³⁾. The condition of the binding of the coat with the carbon fiber, and the thickness of the coat, and the degree of uniformity all are closely related to the technological parameters. Under conditions of appropriate technology we can plate a thin and uniform nickel coat microstructure; see Fig. 1-a. When the plating time increases, the thickness also correspondingly increases, as Fig. 1-b shows. The cleanliness of the carbon fiber surface is the necessary condition to obtain a good coating, in incomplete rinsing the fibers and the coating have an obvious disjointed appearance, even complete coats will not stay on, as shown in Fig. 1-c and 1-d. The surface appearance of a typical nickel-plated carbon fiber is shown in Fig. 1-e.

2. Microstructure of Nickel-Plated Carbon Fibers After Vacuum Heat Treatment

The observance of microstructure of nickel-plated carbon fibers after vacuum heat treatment is an important method of researching the interaction of nickel carbon. Following the change in temperature and time of vacuum heat treatment, the microstructure of nickel-plated carbon fiber has a series of evident changes.

After heat treatment below 700°C, the microstructure of the carbon fiber has no evident changes. When the temperature raises to 750°C and treatment time increases, a "surface" structure appears on the nickel-plated carbon fiber, and the nickel in the nickel-plate layer assumes a needle form that permeates into the inner part of the carbon fiber, as Fig. 2-a shows. When the temperature continually rises, the nickel coating thins (even is eliminated) the nickel begins to build up in the inner part of the carbon fiber. The microstructure after treatment at 800°C is shown in Fig. 2-b.

3. The Microstructure of Carbon-Aluminum Composit Wires

Using chemical gas deposit method, the deposit on the carbon fiber

surface is one titanium-boron coating, and directly soaking aluminum is an effective method of preparing the carbon-aluminum composite wires. But the control of the gas deposit and soaking technological parameters has a very large influence on the infiltration and composites of carbon fibers with aluminum liquid. When the control of the technological parameters is suitable, the carbon fibers and aluminum liquid can spontaneously infiltrate, and fiber distribution is also comparatively uniform, as Fig. 3-a shows. When the control of technological parameters is not good, then it cannot have a good soaking interaction with the aluminum, as shown in Fig. 3-b. In the figure it is evident that in the center part aluminum liquid has no immersion. Figures 3-c and 3-d are photographs of fracture of carbon-aluminum composite wires. From the center it is evident that when carbon fibers produce boundary surface reaction with aluminum, fiber and aluminum interaction strengthens the fiber fracture level, and there is no appearance of pulling out. When the interaction of fiber and basic is appropriate, the fibers have a slight pulling out, as Fig. 3-d shows.

4. Microstructure of Carbon-Aluminum Hot-Pressed Solidified Composites

Under temperatures that are close to the melting point of aluminum, carbon fiber or carbon-aluminum composite wire that will go through coating treatment can obtain carbon-aluminum composite plate with aluminum foil hot-press solidification. Figure 4-a is a photograph of a carbon-fiber and aluminum hot-press specimen that has no coating, demonstrating that carbon fibers and aluminum do not have a very good interaction. Figure 4-b is a photograph of a carbon fiber and hot-press specimen that has a coating, demonstrating that interaction of carbon fibers and aluminum basic is very good. Figure 4-c shows the separation condition of carbon fibers in the carbon-aluminum composite wire and aluminum hot-press specimen.

CONCLUDING REMARKS

The analysis on nickel plated carbon fibers, vacuum heat treated nickel-plated carbon fibers, carbon-aluminum composite wires, and

hot-press test samples make clear, their microstructure and its technological process have a close relationship, and therefore we can discover the existing problem in the technological process through analysis and research of the microstructure, provide a foundation to further correctly choose the technological parameters, improve the technological process, and enhance the properties of fibers and composite material.

The metallographic method and sweep electron microscope method are effective means to analyze and research the microstructures of carbon fibers, nickel-plated carbon fibers, vacuum heat treated nickel-plated carbon fibers, carbon-aluminum composite wires, and hot press test samples, but it is necessary to interact with the correct manufacturing method and a good buff grinding technique, then we can really, objectivelt show the form of microstructures.

Regarding the effects of microstructures of carbon fiber coating and carbon fiber and aluminum produced coating and fiber, the effect of basic, etc., the problems are pending further research. At the same time as the suitable above research work, we still must explore new manufacturing methods and adopt new techniques.

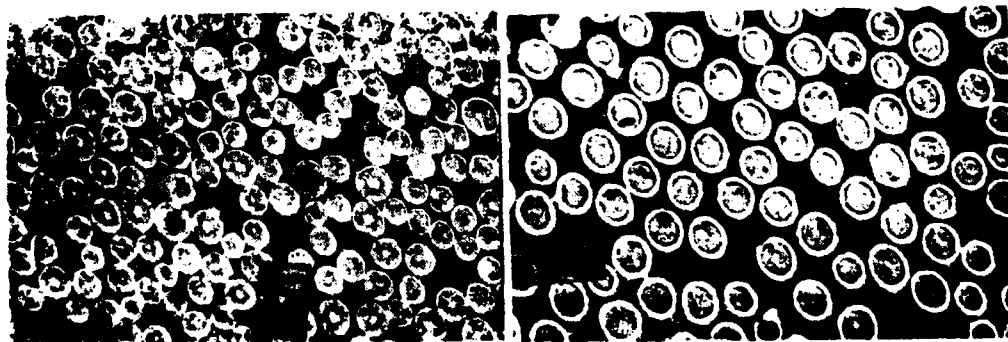


FIG. 1-a: MICROSTRUCTURE OF
CARBON FIBER COATED WITH
NICKEL (in 25 minutes)

475X

FIG. 1-b: MICROSTRUCTURE OF
CARBON FIBER COATED WITH
NICKEL (in 30 minutes)

675X



FIG. 1-c: 4000x



FIG. 1-d: 2000x

FIG. 1-c and 1-d: NICKEL-COATING CARBON FIBER WITH DIRT



FIG. 1-e: TYPICAL END
VIEW OF CARBON FIBER
COATED WITH NICKEL
5000x



FIG. 2-a: 200x
MICROSTRUCTURE OF CARBON
FIBER COATED WITH NICKEL
TREATED AT 750°C (in 1 hour)



FIG. 2-b: 5000x
MICROSTRUCTURE OF CAR-
BON FIBER COATED WITH
NICKEL TREATED AT 800°C
(in 1 hour)

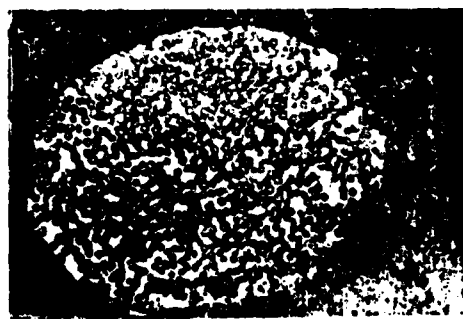


FIG. 3-a: 250x
MICROSTRUCTURE OF CARBON-AL-
UMINUM COMPOSITE WIRE



FIG. 3-b: 250x
MICROSTRUCTURE OF PARTIAL
COMPOSITE CARBON-ALUMINUM
WIRE

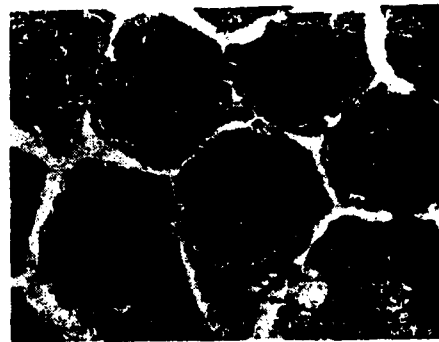


FIG. 3-c: 2000x
FRACTURE OF CARBON-ALUMINUM
COMPOSITE (Strong Bonding)



FIG. 3-d: 1500x
FRACTURE OF CARBON-ALUMINUM
COMPOSITE (Intermediate
Bonding)



FIG. 4-a: 1500x
MICROSTRUCTURE OF UNCOATED
HEAT-PRESSES CARBON FIBERS-
ALUMINUM COMPOSITE



FIG. 4-b: 500x
MICROSTRUCTURE OF COATED
CARBON FIBERS-ALUMINUM
OILS COMPOSITE (Hot-pressed)



FIG. 4-c: 100x
MICROSTRUCTURE OF CARBON-ALUMINUM
COMPOSITE (Hot-pressed from carbon
fiber-aluminum composite wires and
aluminum foils)

Reference Literature:

- 1) Li Xianjin, Guo Gongdun, Zhang Zenghu, Li Renhe, Tan Yi Lu Fu Hu Si De Zhi Bei, Shang Hai Jiao Tong Da Xue Cai Liao Ke Xue Ji Gong Cheng Lun Wen Ji. "Li Xianjin, Guo Gongdun, Zhang Zenghu, Li Renhe, The Preparation of Carbon-Aluminum Composite Wires, Shanghai Communications University, Collection of Material Science and Engineering Dissertations, June 1980, pages 178-186".
- 2) Luo Shuofu, Huang Guanfeng, Yu Ailian, Tan Xian Wei Hua Xue Du Nie Tong, Shang Hai Jiao Tong Da Xue Ji Shu Zi Liao (81488). "Luo Shuofu, Huang Guanfeng, Yu Ailian, Carbon Fiber Chemical Nickel and Copper Plating, Shanghai Communications University Technical Material (81488) August 1980".
- 3) Zhao Changren, Hou Dingkang, Jin Cheng, Wang Wu, Jiang Yuhe, Du Nie Tan Xian Wei Yu Lu De Gu Tai Kuo San Nian Jie, Shang Hai Jiao Tong Da Xue Ji Shu Zi Liao (81487). "Zhao Changren, Hou Dingkang, Jin Cheng, Wang Wu, Jiang Yuhe, Solid State Diffusion Coherence of Nickel-Plated Carbon Fibers and Aluminum", Shanghai Communications University, Technical Material (81487), August 1980.

FLOURISHING DEVELOPMENTS IN ACADEMIC ACTIVITIES OF CHINA AERONAUTIC INSTITUTE

In the China Aeronautic Institute in the period from August to October 1981, academic activities were perfectly dynamic. China Aeronautic Institute successively with China Automation Institute jointly convened "Control System Models and Real Technological Exchange Conference", jointly convened "The Third National Crack Mechanics Symposium" with China Mechanics Institute and China Machinery Engineering Institute, jointly convened "Titanium and Titanium Alloy Symposium" with China Metallurgy Institute, jointly convened "Engine Combustion Symposium", "Engine Heat Transmission Symposium", Impeller Machinery Pneumatic Heat Mechanics Symposium", and "Engineering Heat Mechanics Symposium" with China Engineering Heat Physics Institute. In addition, each committee of related disciplines at China Aeronautics Institute successively convened "Computer Auxilary Aircraft Design-Auxilary Geometric Design-Auxilary Manufacturing Symposium" (simply called CAD/CAGD/CAM Symposium), "Flight Mechanics and Test Flight Symposium", "Applications of Modern Control Theory and Electronics in the Area of Aeronautics and Space Navigation Symposium", "Non-Metallic Material and Technology Symposium", "Optics Metallography and Transmission Electron Lens Symposium", "Aircraft Technology Symposium", "Aeronautics Maintenance Engineering Specialty Committee Establishment Conference and Aeronautic Maintenance Engineering Theory Seminar", "Special Problems of Composite Material Seminar", and others, totalling seventeen symposiums. In August in Beijing they also jointly held "Composit Material Short Term Training Course" with Beijing Aeronautics Institute.

The above academic activities all are academic conferences that belong to the discipline committees or specialty study groups. The representatives present at the meeting unanimously considered that the convening of these symposiums was perfectly essential, and also very timely. For some meetings it was the first time held in the last ten-plus years. Each related unit and numerous experts, professors, and science and technology personnel enthusiastically delivered their theses, and enthusiastically supported the academic activities. The research

papers that were received at these meetings were comparatively many, the content was considerably rich, the related specialty learning scope was also very extensive. From the theses quality and level the fields were clearly at a higher level than previously.

These academic activities possess the following characteristics: Firstly, they are alike or nearly alike academic activities that are held jointly with brother institutes and have specialty content, many famous experts, professors, and science and technology personnel from within the country were invited who participated in the activities, thus making the scope of the symposiums even more extensive. At the same time it also enhanced the quality of the academic activities and reflected the present level of science of our country's related disciplines. Secondly, these academic conferences, aside from exchanging the research results and experience of recent years in the various areas of scientific research, production, teaching, etc., still invited related experts to the conferences to make the summary academic report of technological developments and trends inside and outside the country, for example: the National Computer Department Vice Department Head Guo Pingxing at the conference of application of modern control theory and electronics in areas of aeronautics and space navigation wrote the comprehensive report "The application of Mini Computers in the Areas of Aeronautics and Space Flight"; Professor Wen Zhuanyuan of Beijing Aeronautics Institute at the "Control Systems Model and Real Technology Symposium" wrote "A Report on Going to America to Observe and Study Ground Flight Analogue Computer"; Professor Yang Pengji of Xi Bei Industrial University at the "CAD/CAGD/CAM Conference" made the academic report on "7760 CAD/CAM System Engineering", making the representatives at the conferences to broaden their academic outlook, obtain inspiration, and received a warm welcome from conference representatives.

In the above academic activities the committees of each discipline at the same time held work conferences, stressing the research of related academic organizational and structural problems. They established the "Aeronautics Maintenance Engineering Specialty Committee", the "Electron Specialty Committee", and the "Automatic Control Specialty

Committee". They deliberated on forming twenty-plus discipline study groups. The work meetings also researched the arrangement of academic activities for each discipline from now on, and put forward plans for activities in 1982 and preliminary tentative plans for activities from 1983 to 1985. They pointed out for academic activities from now on: We should closely combine the realistic needs of our country's present four modernizations to develop academic activities of some special topics. The scale of the meetings can be somewhat small, the discussion content can be somewhat deep, and interaction of scientific research, production, and teaching practices can become even closer.

"JOURNAL OF AERONAUTICS" BRIEF RULES FOR SOLICITED CONTRIBUTIONS

"Journal of Aeronautics" is a comprehensive academic publication sponsored by China Aeronautic Institute, already published and available inside and outside the country in 1980. This publication takes Marxism, Leninism, Mao Zidong thought as its guide. It thoroughly carries out the guiding principle of "Let a hundred flowers bloom, let a hundred schools of thought contend", develops academic exchange, and promotes the modernization of space navigation science and technology.

This publication primarily publishes scientific research results in the realm of aeronautics and space navigation science and technology. The reader target is primarily specialists engaged in scientific research, teaching, design, production, and application in the areas of aeronautics and space navigation science and technology.

I. This publication publishes the following various contributions:

1. New academic achievements related to aeronautics and space navigation science and technology, including aerodynamic mechanics and flight mechanics, aircraft design and structure strength, aerodynamic devices, electronic technique and automatic control, academic discussion of production in the area of technique and material, and achievements and experiences of new theory and new technique applications.
2. Technological reading notes, reports, and summarized discussions of related aeronautic and space navigation science and technology that has been newly created.
3. Explanation and discussion of books and literature that are related to aeronautics and space navigation science and technology.

II. Requirements for Contributions:

1. The content of the analysis, computations, test data, etc.

of the contributions must be correct and without error, structure must make every effort to be close, arrangement of ideas must be clear, grounds of argument must be well-knit, and writing style must be succinct and easy to understand. Each essay should take 5000 characters as appropriate, and the length of the produced dissertation must not exceed 10,000 characters (including illustrations and tables).

2. Contributions use 16 evolution ruled paper. A fountain pen must be used for writing. Writing must be neat and clear. The units of technical terms and computations should be consistent throughout.

3. Illustrations shall use drawing paper according to the engineer-ed drawing, the words on the illustration shall be written with a pencil. Please position illustrations centered on the manuscript, and use three ruled spaces to frame the drawing. The order, title, and the notes of the illustrations should be underneath the corresponding frame, and translated into English. The drawing paper cannot be pasted onto the manuscript, a separate pamphlet of hte illustrations shall be attached.

4. Equations all without exception shall be centered on the man-uscript, the number of the equation shall be enclosed in () on the right margin, without a dotted line.

5. Reference literature should be listed by number in back of the text, according to the exact order used in the text; only list primary and published literature. It shall be written in the following pattern: (number) Author, Book Title, Publisher, Year Published, Page Numbers. (number), Author, Article Subject Title, Periodical Name, Volume Number, Publication Number, Year, Pages.

6. The article must include an abstract in Chinese and English (number of words not to exceed 300), English spelling of the author's work unit, and Chinese spelling in pinyin of the author's name.

III. Other

1. If submitted manuscripts have been read at a certain conference, have appeared in another journal, or have already been published, this must be made clear.
2. After submitted manuscripts have been examined, all essays that are carried in "Journal of Aeronautics" will receive payment according to regulations.
3. Submitted manuscripts may be mailed to: Beijing, Institute Way, China Aeronautics Institute, Journal of Aeronautics Editorial Department. Be sure not to mail it to an individual.